Density Functional Theory Studies of Cs-based Double Perovskites for Solar Cell and Photocatalysis

（太陽電池と光触媒のためのセシウムベースダブルペロブスカイトの密度汎関数理論研究）

Graduate School of Life Science

And System Engineering

Kyushu Institute of Technology

Dissertation for the Degree of Doctor of Philosophy

Author: YE XINYU

Supervisor: Professor Tingli Ma

November. 2022

Abstract

In recent years, halide perovskite materials have attracted extensive interests and attention of researchers due to their high optical absorption coefficient, low electron hole recombination rate, long carrier diffusion length and low manufacturing cost. However, most of the highly efficient perovskite photovoltaic materials currently prepared contain heavy metal element lead, which seriously pollutes the environment and limits large-scale commercial application. In addition, perovskite materials are easy to decompose due to the influence of air and water, which restricts the photovoltaic performance. Cesium based double perovskite is expected to solve these problems because of its excellent stability and more choices for lead-free applications. Inspired by the advantages of cesium based double perovskite, our work mainly focuses on the theoretical research on the structural, electronic and optical properties of this kind of perovskites by density functional theory (DFT). The work aims to predict the potential of cesium based halogenated double perovskites in the application of perovskite solar cells and photocatalysis, and to clarify the microscopic physical and chemical mechanisms, thereby providing theoretical guidance for the experimental work.

In chapter 1, the research progress and background of the ABX_3 and Cs_2BX_6 perovskites were introduced. In addition, the developments and status of perovskite solar cells and photocatalysts were also introduced. Finally, the purpose of this thesis was depicted.

In chapter 2, the detailed descriptions of the theoretical calculation methods were represented. The development process, theoretical framework and some new developments of the first principle theory were introduced. In addition, computational software packages used were briefly introduced.

In chapter 3, we simulated and optimized the structure of the $Cs_2PtI_{6-y}Cl_y$, $Cs_2PtI_{6-y}Br_y$, and $Cs_2PtBr_{6-y}Cl_y$ (y = 0, 1, 2, 3, 4, 5, 6) and systematically studied their electronic properties. The calculated tolerance factor and formation energy revealed good stability for all these compounds. In addition, the substitutional doping of halogen ions can effectively adjust the bandgap and show an obvious trend.

In chapter 4, structural, electronic, and optical properties of 30 kinds of Cs_2BX_6 compounds were studied by DFT calculation. Theses perovskites with potential application in solar cells and photocatalysts were pre-screened based on bandgap calculation results. After studying the optical

properties and band edge positions, we found 8 kinds of cesium based double perovskites which have the application research value of single junction solar cells and photocatalysts.

In chapter 5, the band structure and density of state (DOS) of g-C_3N_4/Cs_2BBr_6 (B=Pt, Ti, Sn) heterojunctions were studied by DFT. After g-C_3N_4 contacted with double perovskite, the band edge positions of the two semiconductors changed, and then different types of band arrangement were formed due to the interaction between g-C_3N_4 and the perovskite interface. The insight gained of this work is of direct relevance to the design of new catalysts relating to g-C_3N_4 or Cs_2BBr_6.

Finally, we summarized this thesis and introduced the possible future development direction of related field. Computational techniques of our thesis can provide theoretical guidance for the rational design of Cs based double perovskite materials with improved photovoltaic and photocatalytic characteristics.

Contents

Chapter 1. Introduction

1.1 Research background and significance

Since the discovery of ABX_3 perovskite materials, people have never stopped their research and exploration. At first, because the development of relevant application fields is not very mature, the research on perovskite materials mainly focuses on structural characteristics, electromagnetic properties, etc.[1,2] In 1993, Helmolt and his research team from Germany found that room temperature magnetoresistance exceeded 60% in perovskite $La_{2/3}Ba_{1/3}MnOx$ films.[3] Shortly afterwards, Jin and his collaborators in the United States observed a magnetoresistance effect of 99.9% in $La_{0.67}Ca_{0.33}MnOx$ thin films prepared with PLD.[4] These colossal magnetoresistance (CMR) effects found in the research of perovskite materials have attracted extensive attention and further detailed research.

High temperature superconductors, multiferroic materials, colossal magnetoresistance materials, solar cell materials, and semi metallic magnetic materials are several important research fields in condensed matter physics in recent years. In these fields, some representative materials have perovskite or perovskite like structures. In 1996, Wu et al. reported a perovskite type unconventional high temperature superconductor $Sr_2YRu_{1-x}Cu_xO_6$ without copper oxide surface, and its superconducting temperature was as high as 30 K.[5] In 1998, Kobayashi et al found that the double perovskite compound Sr_2FeMoO_6 has a tunneling magnetoresistance effect at room temperature.[6] In 2015, the first multifarious material $LaMn_3Cr_4O_{12}$ with cubic perovskite lattice was discovered.[7] In addition, the discovery of a large number of semi metallic magnetic materials with perovskite structure, such as $CaFeO_3$,[8] $YMnS_3$,[9] $NiCrO_3$,[10] Sr_2NiOsO_6,[11] has expanded the research field of perovskite to spintronics. In particular, in 2009, Miyasaka and his research team prepared quantum dots of ABX_3 type organic/inorganic hybrid perovskite materials such as $CH_3NH_3PbI_3$ and $CH_3NH_3PbBr_3$, and applied them to dye sensitized solar cells, achieving a photoelectric conversion efficiency of 3.8%,[12] thus opening the prelude of ABX_3 type perovskite materials in the field of solar cell research and achieving great success.

Although the materials mentioned above have different physical properties, their basic structures can be summarized as ABX_3 perovskite structure or its derivative compounds. At the same time, the strong correlation existing in perovskite materials, especially the inextricable

relationship between structure and physical properties, also deepens people's further understanding of perovskite materials, thus pushing condensed matter physics to a wider and deeper level.

In addition, theoretically, ABX_3 perovskite materials can provide a variety of combinations, thus giving theoretical researchers a wider modeling space. Because the ions at A, B and X sites in ABX_3 perovskite materials have different electronic configurations, different ion radii and different types of exchange effects, it is possible to realize the assumption of a variety of different types of perovskites by changing the types of ions at A, B and X sites. All these provide a relatively perfect theoretical basis for revealing the characteristics of correlation interaction and electron transport in perovskite materials. The research on magnetic, optical and electrical properties of ABX_3 perovskite materials will have broad research prospects and research values.

1.2 ABX_3 perovskite compounds

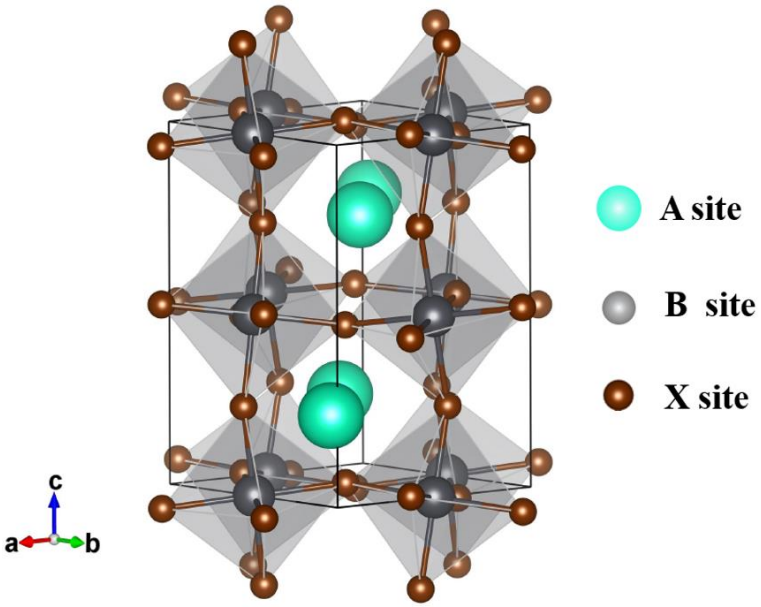

Figure. 1. Scheme of the structure of ABX_3 perovskite.

The structure of perovskite compound is similar to calcium titanate ($CaTiO_3$). As a by-product in alkaline rocks, perovskite is one of the most abundant minerals on the earth. It was first discovered by Gustav Rose, a German mineralogist, in 1839 in the metamorphic rocks of the Ural Mountains in Russia, and later named after Von Perovski, a Russian geologist.[13]

In the narrow sense, perovskite refers to calcium titanate mineral. However, with the improvement of technology, some compounds with similar crystal structure to calcium titanate

have been found and obtained in the laboratory, such as $LaMnO_3$, $BiFeO_3$, $BaTiO_3$, etc. Therefore, the perovskite referred to today is a class of compounds similar to the crystal structure of perovskite. Their chemical composition can be uniformly expressed as ABX_3, in which A is usually a cation with large radius such as Na^+, K^+, Ba^{2+}, Sr^{2+}, Ca^{2+}, etc; B is generally a cation with small radius, such as Nb^{5+}, Fe^{3+}, Ta^{5+}, Th^{4+}, Ti^{4+}, etc; X is generally an anion, such as O^{2-}, F^-, Br^-, etc. Since a variety of element atoms with different quantities can be at A, B and X positions, there are many kinds of perovskite compounds, which are widely used in geology and materials science.

Ideally, the crystal structure of ABX_3 perovskite is shown in Figure 1. It belongs to an equiaxed crystal system. The coordinate parameters of each atom in the cell are A (0, 0, 0), B (0.5, 0.5, 0.5) and X (0.5, 0.5, 0), respectively. The space group is $Pm\bar{3}m$. Its crystal structure can be seen as that the octahedron formed by BX_6 is connected through a common vertex angle. The A cation is located in the center of the void formed by the octahedron, and its coordination number is 12. Since the ionic radii of A and X are very similar, from the view of dense packing, this structure can also be seen as a result of the hexagonal dense packing of the atomic layer formed by A and X along the (111) direction and the filling of octahedral voids by B ions.

For ordinary calcium iron ores, the chemical bonds in the structure are usually ionic bonds. In ionic compounds, the same charges will repel each other, while the opposite charges will attract each other. The hard sphere stacking model shows that the coordination number is usually determined by the radius ratio of positive and negative ions, that is, for a certain crystal structure, if the coordination number of positive and negative ions is determined, the value of the radius ratio of positive and negative ions is also determined. If anions and cations with different radii are combined with each other, the symmetry of the perovskite crystals will be different, thus obtaining a variety of perovskite structures with different distortion. Theoretically, the tolerance factor is commonly used to characterize this symmetry relationship of perovskite crystals, and its calculation expression is:[14]

$$\tau = \frac{R_A + R_X}{\sqrt{2}(R_B + R_X)} \quad (1)$$

where R_A, R_B and R_X denote the ionic radius of the A, B and X in the A_2BX_6 double perovskite structure, respectively. For most perovskite materials, the crystal structure is not an ideal cubic structure due to the regulation of the radius ratio of anions and cations, and most crystals will deform on the basis of the cubic structure. When $\tau<0.77$, the crystal is ferrotitanium; If $0.77<\tau<1.1$,

the crystal exists as perovskite; When $\tau > 1.1$, the crystal exists as aragonite or calcite.[15] Only when the tolerance factor is close to 1 or the crystal is in high temperature environment, the ideal cubic structure will appear.

The crystal structure of ABX_3 semiconductor perovskite determines its bandgap to some extent. Generally speaking, if the ionic radius decreases, the cell volume will shrink, the bandgap will become larger, and the absorption spectrum will shift blue. On the contrary, if the ionic radius is increased, the volume of the cell will expand, resulting in a narrowing of the bandgap and a red shift in the absorption spectrum. To maintain the three-dimensional crystal structure of ABX_3 semiconductor perovskite, it is necessary to ensure that its tolerance factor is between 0.77 and 1.1. At this time, the radii of anions and cations at A, B and X positions must be appropriate. Therefore, in order to form an ideal cubic perovskite and have a bandgap that meets the actual needs, it is necessary to select appropriate anions and cations.[15]

1.3 Cs_2BX_6 perovskite compounds

Typical perovskite compounds generally have the chemical composition of ABX_3. Considering the type, quantity, ordered or disordered substitution of A, B and X ions, this ABX_3 type perovskite compound can be divided into many perovskites with different chemical compositions. Some modifications in the basic structure of perovskite, such as $A_2B^{1+}B^{3+}X_6$ [16] and $A_2B^{4+}X_6$ [16,17], have been reported in the literature. By replacing each pair of adjacent B cations with a B^{1+} and a B^{3+} cation at the top, the $A_2B^{1+}B^{3+}X_6$ structure (also known as anorthite) can be considered cubic. In terms of structure, if half of the B cations in the $[BX_6]$ cluster center are removed, it will be transformed into a double perovskite with the formula of A_2BX_6, such as Cs_2SnI_6 or Cs_2PbBr_6, which can be considered as a derivative of ABX_3, extending the type of cations used for substitution to B site.[18] Generally, it is referred to as antifluorite crystal (K_2PtCl_6) and described by the $[BX_6]^{2-}$ octahedral cluster bridged by the A-site cation. The A_2BX_6 structure was shows in Fig. 2 and has similar characteristics to ABX_3 perovskite, most of which have cubic structure.

A new sort of all inorganic Cs based halogenated perovskite has been developed by using oxygen evolution in water recently,[19–21] which effectively improves the thermal stability of the material, thereby prolongs the service life of the equipments.[22] In addition, the introduction of Cs can suppress the phase impurities, permitting the preparation with high purity

and defect-free perovskite films, which is less sensitive to processing conditions. This enables perovskite solar cells device performance to achieve repeatable high efficiency.[23] Recent studies on lead-free perovskite substitutes, especially A_2BX_6, usually report the synthesis and characterization of bulk powders or single crystals, such as Cs_2ZrCl_6, Cs_2SnI_6, Cs_2TiBr_6, and so on.[24–26]

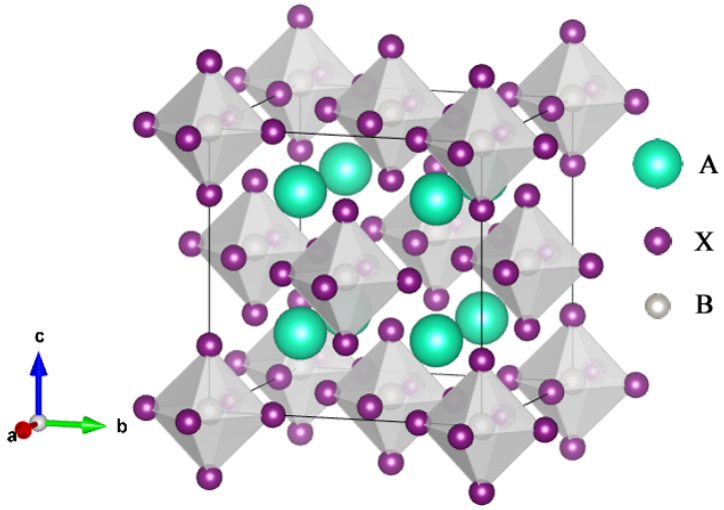

Figure. 2. Scheme of the structure of A_2BX_6 double perovskite.

1.4 Perovskite solar cell

With the rapid development of human society, people's demand for energy has increased rapidly. The limitation of traditional fossil energy and a series of problems such as environmental pollution and climate warming caused by massive consumption have triggered an urgent demand for sustainable energy. Because of its good cleanliness and inexhaustible characteristics, solar energy has solved the increasingly acute problem of energy depletion and the contradiction between energy and environment. Therefore, how to use solar energy efficiently has become an urgent problem for scientists all over the world. Solar cells realize the conversion of solar energy to electric energy, making it possible for humans to effectively use solar energy. In 1883, Frits et al. prepared the first semiconductor/metal junction solar cell in human history, with a photoelectric conversion efficiency of about 1%.[27] In 1954, Bell Laboratories developed a crystalline silicon solar cell with a photoelectric conversion efficiency of 4.5%. These major events in the field of solar cell research and development have opened the prelude to the use of solar power by human beings.[28]

The development of solar cell technology has mainly gone through three stages: (1) the first generation of solar cells, in which the preparation materials of solar cells are mainly monocrystalline silicon and polycrystalline silicon. At present, the conversion efficiency of monocrystalline silicon solar cells has reached 25%, and the conversion efficiency of polycrystalline silicon solar cells has also exceeded 20%.[29] However, due to the extremely high requirements for the purity of the raw material silicon in the preparation of monocrystalline silicon and polycrystalline silicon solar cells, such cells are very expensive, and their energy consumption is also large. These factors have affected their further commercial applications.[30] (2) In the second-generation solar cell stage, which mainly includes thin film cell, such as amorphous silicon and polycrystalline silicon thin film cells. At present, the photoelectric conversion efficiency of such thin film cells also exceeds 20%.[29] This kind of solar cells also faces problems that cannot be solved, such as environmental pollution, high manufacturing cost, and unsustainable.[31] (3) Some third-generation new concept solar cells with high conversion efficiency, such as organic solar cells, dye sensitized cells, etc.[32-34] Among them, some solar cells based on ABX_3 perovskite materials have attracted great attention due to their rich raw materials and low manufacturing costs. In particular, in recent years, people have made a series of major breakthroughs in the research field of organic-inorganic hybrid perovskite solar cell, which makes this kind of perovskite solar cells become one of the research hotspots in the photoelectric field.[35-39]

In 2009, Miyasaka group prepared 9-10 nm quantum dots from organic-inorganic hybrid perovskite materials such as $CH_3NH_3PbI_3$ and $CH_3NH_3PbBr_3$, and applied them to dye sensitized solar cells, obtaining 3.8% photoelectric conversion efficiency.[35] In 2011, Jeong Hyeok et al. increased the size of $CH_3NH_3PbI_3$ quantum dots to 2-3 nm, and the solar cell efficiency based on the quantum dots was about 6.54%.[36] In 2012, a solid hole conductor material was introduced into perovskite solar cells by scientists, and the efficiency was about 10%.[40] In 2013, people improved the preparation method of perovskite solar cells through sequential deposition, and increased the conversion efficiency of the cells to 15%.[41] In the same year, Lidzey and his collaborators obtained a perovskite type planar heterojunction cell with a conversion efficiency of 15.4% by vapor evaporation.[42] Through the efforts of many scientists, the conversion efficiency of perovskite solar cells has increased to 25.7% this year, as shown in Figure 3.[43]

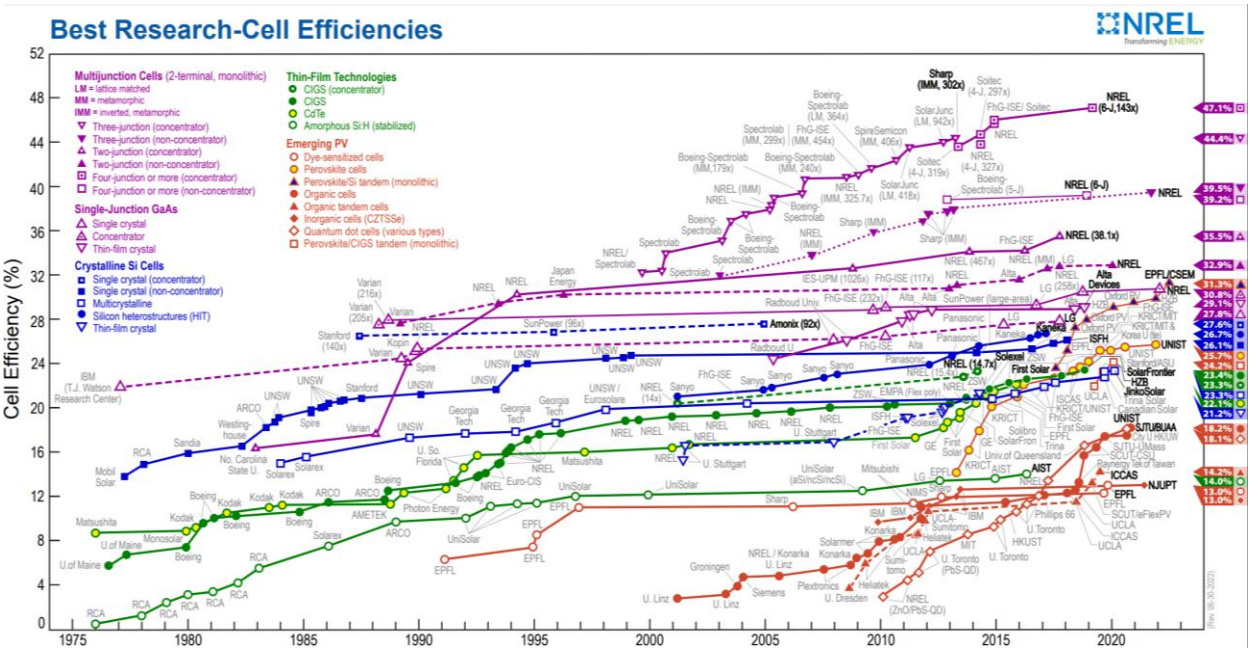

Figure. 3. Power conversion efficiency of various solar cells.[43]

The structure of the perovskite solar cell is very similar to that of the dye sensitized solar cell because it is improved on the basis of the dye sensitized solar cell. Perovskite solar cells mainly adjust the optical properties by changing the chemical composition of perovskite materials. The main role of perovskite in planar heterojunction solar cells and mesoscopic structure solar cells is light absorber. The components of general perovskite solar cells include counter electrode, conductive glass substrate, hybrid perovskite optical absorption layer, electron transport layer, semiconductor porous film and hole transport layer, as shown in Figure 4.

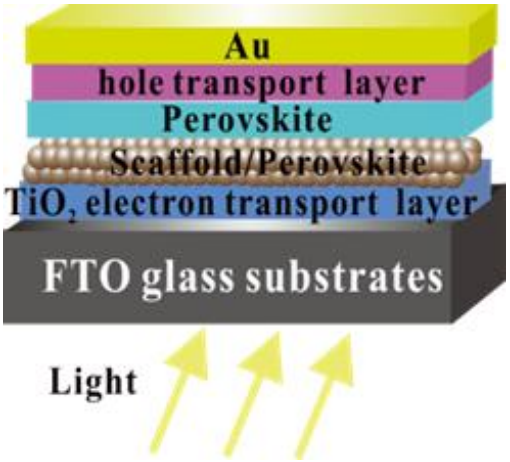

Figure. 4. Sketch of device structure of a normal PSCs

Solar cells based on organic-inorganic hybrid perovskite have many advantages, such as low price, simple preparation process, high photoelectric conversion efficiency, etc. However, there

are still several important factors that restrict the further development of solar cells. These factors mainly include: (1) The absorption spectrum of an ideal solar cell should be relatively wide, for example, it can absorb light waves from visible light to near-infrared wavelength in the range of 350-950 nm. However, due to the influence of the bandgap of perovskite, the light response range of these light absorbing materials based on organic-inorganic hybrid perovskite is relatively narrow. (2) Some existing organic-inorganic hybrid perovskite solar cell with high conversion efficiency contain lead element. Because of the toxicity of lead, it is explicitly prohibited in many countries. How to find a substitute for lead while maintaining high power conversion efficiency is an urgent problem to be solved. (3) The stability of organic-inorganic hybrid perovskite solar cells will be affected not only by the properties of the materials themselves, but also by environmental factors, processing conditions, UV light and other conditions. Therefore, how to improve the stability of organic-inorganic hybrid perovskite solar cells is the focus of future theoretical and experimental research.

In a word, it is of great scientific significance to find perovskites with good stability and ideal bandgap for the research and development of solar cells. In this research field, although researchers in various countries have done a lot of work, there is still a lack of strong explanation for some important issues, whether experimental or theoretical, such as authoritative reports on the structural stability of $CH_3NH_3PbI_3$ crystal in theory. On the way to explore new perovskite solar cell materials, in order to avoid a large number of repeated experiments when looking for replacement elements of Pb, it is possible to predict the structure and properties through theoretical simulation, and then conduct targeted experimental research. Due to the complexity of the organic-inorganic hybrid structure, the conclusions of some theoretical and experimental studies are not consistent at present, which requires more reliable calculation methods and more detailed parameter settings to verify the experimental results. Reasonable theoretical predictions are very important for exploring the working mechanism of organic-inorganic hybrid perovskite solar cells and optimizing their photovoltaic performance.

1.5 Perovskite photocatalysis

In solar energy collection, photothermal, photovoltaic and photocatalysis are three different methods, which involve power generation, with an annual growth rate of about 33%.[44] Among them, the fields of photothermal and photovoltaic have been fully established and explored. On

the other hand, photocatalysis is a new field with great potential. It can convert the rich H_2O, CO_2 and N_2 on the earth into energy rich products, such as H_2, CH_4, CH_3OH and NH_3, by using solar energy through processes such as water decomposition to generate H_2, organic pollutant degradation, CO_2 reduction, N_2 fixation, etc.[45-52] Through these photocatalytic processes, solar energy can be used for wastewater treatment and can be converted into useful chemical fuels such as H_2, hydrocarbons and NH_3 using different raw materials. Solar light mainly includes three different kinds of energy radiation (ultraviolet (UV), visible light (vis) and near-infrared (NIR)). According to the optical absorption of the working photocatalyst, specific energy radiation can be used in the above photocatalytic process. In order to develop the main part of solar spectrum, it is of great significance to design and develop efficient photocatalysts that can capture visible light and near infrared region. NIR active photocatalysts are of great importance because they can obtain NIR light from the solar spectrum, and because of the high penetration depth of NIR radiation, they can also be used in cloudy days.[53] The use of this highly efficient photocatalyst to collect solar energy from all regions can contribute to global energy security, because it may limit the dependence on non-renewable energy and may combat environmental pollution to limit climate change.

The perovskite oxides (ABO_3) are originated from $CaTiO_3$ and are widely studied for various photocatalytic applications owing to their high stability, adjustable structures, and excellent photocatalytic activity. Several kinds of element can be adjusted at A and B-sites resulting in a huge family.[54] The availability of these different sites allows the researchers to replace or dope different elements and to fabricate new materials with high photocatalytic activity. In addition, the substitution or doping of cations at A and B sites with other elements leads to changes in composition and symmetry, leading to the formation of cations or oxygen vacancies, which seriously affects the band structure, light absorption, adsorption and photocatalytic performance of perovskite materials. In addition, O-site doping can also change the bandgap, thereby changing the optical properties of perovskites. Therefore, the photocatalytic activity of perovskite materials can be easily adjusted. Different nanostructures, composites and heterojunctions can also be prepared by using different modification sites.[55, 56]

1.6 Challenges and motivation of this thesis

As mentioned above, perovskite solar cells are the most promising and most likely to be

commercialized third generation solar cells. Due to the existence of organic cations, the thermal stability of organic-inorganic hybrid perovskite solar cells is not ideal. All inorganic devices exhibit excellent thermal stability when substituted with Cs ions. In addition, the toxicity of lead ions in halide perovskite absorption materials is the main bottleneck in practical applications. Perovskite composed of other divalent cations instead of lead may have poor photoelectric properties due to its large band gap. Therefore, attempts have been made to explore the perovskite like structure through double perovskite. Cs_2BX_6, a new type of perovskite, provides a new idea for researchers to prepare green materials without loss of photoelectric properties, and shows excellent stability in light, humidity and temperature.

Recently, these lead halide double perovskites have been extended to the field of photocatalysis. Various lead halide double perovskite and its composites have been studied to improve their hydrogen evolution performance. Through the construction of heterojunction, the charge separation between double perovskite and g-C_3N_4 is significantly promoted, and the photocatalytic activity can be effectively improved under visible light irradiation. Heterojunction between perovskite and other semiconductor materials can effectively promote charge separation and maintain the stability of photocatalyst.

There are few studies to predict the properties of cesium based halogenated double perovskites through simulation calculation. The potential application of these materials in solar cells and photocatalysts is worth exploring. The results of theoretical calculation can provide a rough prediction for experimental work, reduce the time cost of experimental exploration, and make the experiment more purposeful. In order to solve the above problems, the following three attempts have been made in this thesis. Firstly, we have successfully investigated the structure, stability and electronic properties of $Cs_2PtBr_yCl_{6-y}$, $Cs_2PtI_yBr_{6-y}$, and $Cs_2PtI_yCl_{6-y}$ (y = 0, 1, 2, 3, 4, 5, 6) using DFT calculations. The general trends in bandgaps and stability are anticipated to provide a guideline for the design of novel stable inorganic halide perovskite materials with ideal properties. Secondly, the structural, electronic, and optical properties of Cs_2BX_6 compounds were calculated using first-principles calculations of Perdew–Burke–Ernzerhof (PBE) and Heyd–Scuseria–Ernzerhof (HSE) with spin-orbit coupling (SOC) methods, with 30 combinations of B = Ti, Zr, Ge, Hf, Pd, Te, Mo, Sn, Pt, and Pb cations, X = Cl, Br, and I halogen ion. Cs_2TiI_6, Cs_2GeBr_6, Cs_2PtI_6, Cs_2PdBr_6, and Cs_2TeI_6 have suitable bandgaps for solar cell applications. The band edge positions of Cs_2TeI_6, Cs_2TiBr_6, Cs_2SnBr_6, and Cs_2PtBr_6 are

matched the water redox potential. Thirdly, the structural, electronic properties and photocatalytic mechanism of g-C_3N_4/Cs_2BBr_6 (B= Pt, Sn, Ti) are systematically investigated by performing first-principles calculations. Our calculation results show that the g-C_3N_4/Cs2$PtBr_6$ and g-C_3N_4/Cs_2SnBr_6 heterojunction forms staggered band arrangement. The g-C_3N_4/Cs_2TiBr_6 forms a straddling gap heterojunction after contact.

References

1 Glazer A. Simple ways of determining perovskite structures. *Acta Crystallogr. A*. **1975**;31:756-762.

2 Wollan E, Koehler W. Neutron diffraction study of the magnetic properties of the series of perovskite-type compounds [(1−x)La, xCa]MnO_3. *Phys. Rev.* **2008**; 100:545-563.

3 Von Helmolt R, Wecker J, Holzapfel B, et al. Giant negative magnetoresistance in perovskitelike $La_{2/3}Ba_{1/3}MnO_x$ ferromagnetic films. *Phys. Rev. Lett.* **1993**; 71:2331-2333.

4 Jin S, Tiefel T, Mc Cormack M, et al. Thousandfold change in resistivity in magnetoresistive La-Ca-Mn-O Films. *Science*. **1994**;264:413-415.

5 Wu M, Chen D, Chien F, et al. Anomalous magnetic and superconducting properties in a Ru-based double perovskite. *Zeitschrift für Physik B Condensed Matter*. **1996**;102:37-41.

6 Kobayashi K, Kimura T, Sawada H, et al. Room-temperature magnetoresistance in an oxide material with an ordered double-perovskite structure. *Nature*. **1998**;395:677-680.

7 Wang X, Chai Y, Zhou L, et al. Observation of magnetoelectric multiferroicity in a cubic perovskite system: $LaMn_3Cr_4O_{12}$. *Phys. Rev. Lett*. **2015**;115:087601-087605.

8 Ali Z, Ahmad I, Khan B, et al. Robust half-metallicity and magnetic properties of cubic perovskite $CaFeO_3$. *Chinese Phys. Lett*. **2013**;30:047504-047508.

9 Wu H, Lu R, Tan W, et al. Theoretical search for half-metallic material: $YMnS_3$. *Solid State Commun*. **2012**;152:288-291.

10 Lee K, Pickett W. Compenstaed half-metallicity in the trigonally distorted perovskite $NiCrO_3$. *Phys. Rev. B*. **2011**;83:180406-180409.

11 Song W, Zhao E, Meng J. Near compensated half-metal in Sr_2NiOsO_6. *J. Chem. Phys.* **2009**;130:114707-114711.

12 Kojima A, Teshima K, Shirai Y. Organometal halide perovskites as visible-light sensitizers for photovoltaic cells. *J. Am. Chem. Soc*. **2009;**131:6050-6051.

13 Rose G. De novis quibusdam fossilibus quae in montibus Uraliis inveniuntur. *Berlin: AG Schadii*, **1839**.

14 Goldschmidt V. Die gesetze der krystallochemie. *Naturwiss*. **1926**;14:477-485.

15 Liu S, Guan Y, Sheng Y, et al. A review on additives for halide perovskite solar cells. *Adv. Energy Mater*. **2020**;10:1902492.

16 Chen H, Xiang S, Li W, et al. Inorganic perovskite solar cells: A rapidly growing field. *Sol. RRL.* **2018**;2:1700188.

17 Maughan A, Ganose A, Bordelon M, et al. Defect tolerance to intolerance in the vacancy-ordered double perovskite semiconductors Cs_2SnI_6 and Cs_2TeI_6. *J. Am. Chem. Soc.* **2016**;138:8453–8464.

18 Jodlowski A, Rodríguez-Padrón D, Luque R, et al. Alternative perovskites for photovoltaics. *Adv. Energy Mater*. **2018**;8:1703120.

19 Kumar A, Swami S, Rawat S, et al. Mixed bismuth-antimony-based double perovskite nanocrystals for solar cell application. *Int. J. Energ. Res*. **2021**;45:16769-16780.

20 Liu S, Guan Y, Sheng Y, et al. A Review on Additives for Halide Perovskite Solar Cells. *Adv. Energy Mater.* **2020**;10:1902492.

21 Tong G, Ono L, Qi Y. Recent Progress of All-Bromide Inorganic Perovskite Solar Cells. *Energy Technol.* **2020**;8:1900961.

22 Liang J, Wang C, Wang Y, et al. All-inorganic perovskite solar cells. *J. Am. Chem. Soc*. **2016**;138:15829-15832.

23 Saliba M, Matsui T, Seo J, et al. Cesium-containing triple cation perovskite solar cells: improved stability, reproducibility and high efficiency. *Energy Environ. Sci*. **2016**; 9:1989-1997.

24 Abfalterer A, Shamsi J, Kubicki D, et al. Colloidal Synthesis and Optical Properties of Perovskite-Inspired Cesium Zirconium Halide Nanocrystals. *ACS Mater. Lett*. **2020**;2:1644-1652.

25 Qiu X, Wang, Cao B, Yuan S, et al. From unstable $CsSnI_3$ to air-stable Cs_2SnI_6: A lead-free perovskite solar cell light absorber with bandgap of 1.48 eV and high absorption coefficient. *Sol. Energy Mater. Sol. Cells*. **2017**;159:227-234.

26 Euvrard J, Wang X, Li T, et al. Is Cs_2TiBr_6 a promising Pb-free perovskite for solar energy applications? *J. Mater. Chem. A*. **2020**;8:4049-4054..

27 Wei J, Zhao Q, Li H, et al. Perovskite solar cells: Promise of photovoltaics. *Scientia Sinica Technologica*. **2014**;44:801-821.

28 Chapin D, Fuller C, Pearson G. A new silicon p-n junction photocell for converting solar radiation into electrical power. *J. Appl. Phys.***1954**;25:676-677.

29 Green M, Emery K, Hishikawa Y. Solar cell efficiency tables. *Prog Photovolt: Res. Appl*. **2013**;43:1-11.

30 Green M. The path to 25% silicon solar cell efficiency: history of silicon cell evolution. *Prog Photovolt: Res. Appl*. **2009**;17:183-189.

31 Parida B, Iniyan S, Goic R. A review of solar photovoltaic technologies. *Renew. Sust. Energ. Rev*. **2011**;15:1625-1636.

32 Mathew S, Yella A, Gao P, et al. Dye-sensitized solar cells with 13% efficiency achieved through the molecular engineering of porphyrin sensitizers. *Nat. Chem*. **2014**;6:242-247.

33 Congreve D, Lee J, Thompson N, et al. External quantum efficiency above 100% in a singlet-exciton-fission-based organic photovoltaic cell. *Science*. **2013**;340:334-337.

34 Kamat P. Quantum dot solar cells: Semiconductor nanocrystals as light harvesters. *J. Phys. Chem. C*. **2008**;112:18737-18753.

35 Kojima A, Teshima K, Shirai Y, et al. Organometal halide perovskites as visible light sensitizers for photovoltaic cells. *J. Am. Chem. Soc*. **2009**;131:6050-6051.

36 Im J, Lee C, Lee J, et al. 6.5% efficient perovskite quantum dot sensitized solar cell. *Nanoscale*. **2011**;3:4088-4093.

37 Li W, Li J, Wang L, et al. Post modify cation of perovskite sensitized solar cells by aluminium oxide for enhanced performance. *J. Mater. Chem. A*. **2013**;1:11735-11740.

38 Zhou H, Chen Q, Li G, et al. Interface engineering of highly efficient perovskite solar cells. *Science*. **2014**;345:542-546.

39 Kim H, Lee C, Im J, et al. Lead iodide perovskite sensitized all solid state submicron thin film mesoscopic solar cell with efficiency exceeding 9%. *Scientific Report*. **2012**;2:591-596.

40 Heo J, Im S, Kim H, et al. Sb_2S_3-Sensitized photoelectrochemical cells: Open circuit voltage enhancement through the introduction of poly-3-hexylthiophene interlayer. *J. Phys. Chem. C*. **2012**;116: 20717-20721.

41 Burschka J, Pellet N, Moon S, et al. Sequential deposition as a route to high performance perovskite-sensitized solar cells. *Nature*. **2013**;499:316-319.

42 Barrows A, Pearson A, Kwak C, et al. Efficient planar heterojunction mixed-halide perovskite solar cells deposited via spray-deposition. *Energ. Environ. Sci*. **2014**;7:2944-2950.

43 NREL. Best Research-Cell Efficiency Chart. Photovoltaic research. https://www.nrel.gov/pv/assets/pdfs/best-research-cell efficiencies-rev220630.pdf. Accessed August 24, 2022.

44 Habisreutinger S, Schmidt-Mende L, Stolarczyk J. Photocatalytic Reduction of CO_2 on TiO_2 and Other Semiconductors. *Angew. Chem., Int. Ed.* **2013**;52:7372−7408.

45 Grabowska E. Selected Perovskite Oxides: Characterization, Preparation and Photocatalytic Properties. *A Review. Appl. Catal. B*. **2016**;186:97−126.

46 Shi R. Waterhouse G. Zhang, T. Recent Progress in Photocatalytic CO_2 Reduction Over Perovskite Oxides. *Sol. Rrl.* **2017**;1:1700126.

47 Chen X, Li N, Kong Z, et al. Photocatalytic Fixation of Nitrogen to Ammonia: State-of-the-Art Advancements and Future Prospects. *Mater. Horiz.* **2018**;5: 9−27.

48 Kong J, Yang T, Ru. Z, et al. Perovskite-Based Photocatalysts for Organic Contaminants Removal: Current Status and Future Perspectives. *Catal. Catal. Today*. **2019**;327:47−63.

49 Olah G, Prakash G, Goeppert A. Anthropogenic Chemical Carbon Cycle for A Sustainable Future. *J. Am. Chem. Soc*. **2011**;133:12881−12898.

50 Kumar S, Kumar A, Kumar A, et al. Nanoscale Zinc Oxide Based Heterojunctions as Visible Light Active Photocatalysts for Hydrogen Energy and Environmental Remediation. *Catal. Rev.*: *Sci. Eng.* **2020**;62:346−405.

51 Christoforidis K, Montini T, Fittipaldi M, et al. Photocatalytic Hydrogen Production by Boron Modified TiO_2/Carbon Nitride Heterojunctions. *ChemCatChem*. **2019**;11:6408−6416.

52 Maeda K, Mallouk T. Two-Dimensional Metal Oxide Nanosheets as Building Blocks for Artificial Photosynthetic Assemblies. *Bull. Chem. Soc. Jpn*. **2019**;92:38−54.

53 Reddy K, Balaji R, Kumar A, et al. Lanthanide Doped Near Infrared Active Upconversion Nanophosphors: Fundamental Concepts, Synthesis Strategies, and Technological Applications. *Small.* **2018**;14:1801304.

54 Pena M, Fierro J. Chemical Structures and Performance of Perovskite Oxides. *Chem. Rev.* **2001**;101:1981−2018.

55 Wang W, Tade M, Shao Z. Research Progress of Perovskite Materials in Photocatalysis- and Photovoltaics-Related Energy Conversion and Environmental Treatment. *Chem. Soc. Rev.* **2015**;44:5371−5408.

56 Grabowska E. Selected Perovskite Oxides: Characterization, Preparation and Photocatalytic Properties—A Review. *Appl. Catal. B*. **2016**;186:97−126.

Chapter 2. Fundamentals of theoretical calculation

In this chapter, we will introduce the theoretical framework of density functional theory (DFT), as well as some recent developments. Here, Schrodinger equation theory is introduced, followed by the theory and derivation of DFT. Then we will introduce the Hartree Fock equation and Kohn Sham (KS) equation, exchange correlation functional approximation and plane wave basis set. The time-dependent density functional theory will also be briefly understood. Finally, some software packages used in this paper are introduced.

2.1 Density functional theory

With the development of computer technology and the improvement of computing performance, many quantitative software simulating material properties have emerged, most of which are developed based on DFT. The DFT is one of the important methods to deal with the energy theory of multi particle systems, and it is also considered to be one of the most effective tools to analyze the electronic and structural properties of solids. The important task of the band theory of solid is to determine the energy level of electrons, and the knowledge of band theory of solid can explain the basic physical properties of solids. Therefore, the band theory of solids one of the most important theories in condensed matter physics research. Solid materials contain a large number of atomic nuclei and extranuclear electrons, which constitute a very complex multi particle and multi electron system. In order to determine the band structure in solids, some approximate methods or simplified treatment must be adopted. The basic idea of DFT in dealing with such problems is to separate the motion of atomic nucleus and external electrons in solid by adiabatic approximation, and then simplify the multi electron problem into a single electron problem by Hartree Fock approximation. This chapter will briefly introduce some basic theories and ideas of density functional theory.

2.2 Schrodinger equation of multi particle system

The solid material can be regarded as a system composed of atomic nucleus and external electrons, and its total Schrodinger equation can be expressed as:[1]

$$H\Psi(\vec{r},\vec{R}) = E^{H}\Psi(\vec{r},\vec{R}) \tag{1}$$

In the above formula, $\vec{R}$ represents the set of coordinates of all atomic nuclei in the multi particle system. $\vec{r}$ corresponds to the set of all extranuclear electronic coordinates in the system. In the absence of an external field, the Hamiltonian of a multiparticle system should include three parts: The total energy of electrons in the system *(H_e)*, the total energy of atomic nuclei (H_N) and the total energy generated by the interaction between atomic nuclei and electrons ($H_{e\text{-}N}$). Therefore, the Hamiltonian expansion of the multi particle system is

$$H = H_e + H_N + H_{e\text{-}N} \tag{2}$$

The Hamiltonian H_e of an electron can be expressed as the sum of the kinetic energy of all electrons and the Coulomb potential energy between all electrons, that is

$$H_e = T_e(\vec{r}) + V_e(\vec{r}) = -\sum_i \frac{\hbar^2}{2m}\nabla_{r_i}^2 + \frac{1}{2}\sum_{i\neq i'}\frac{e^2}{|r_i - r_j|} \tag{3}$$

In formula (3), $\hbar$ is the reduced Planck constant, m is the electron mass, and e is the electron electric quantity. Similarly, the Hamiltonian of atomic nuclei can be expanded as the sum of kinetic energy and interaction potential energy of all atomic nuclei:

$$H_N = T_N(\vec{R}) + V_N(\vec{R}) = -\sum_j \frac{\hbar^2}{2M_j}\nabla_{R_j}^2 + \frac{1}{2}\sum_{j\neq j'} V_N(\vec{R}_j - \vec{R}_{j'}) \tag{4}$$

In Formula (4), M_j is the mass of the jth nucleus. It can be seen that the formula does not give a specific expression of the potential energy of the interaction between atomic nuclei, but shows that the amount is related to the relative position of atomic nuclei. The potential energy of electron nucleus interaction in multi particle system can be written:

$$H_{e-N}(\vec{r},\vec{R}) = -\sum_{i,j} V_{e-N}(\vec{r}_i - \vec{R}_j) \tag{5}$$

Although Formula (1) - (5) can well describe the state of the multi particle system, it is very difficult to directly solve the Schrodinger equation due to the large number of particles and complex interactions in the multi particle system, so it needs to be approximated and simplified.

2.3 Born-Oppenheimer approximation

In the multi particle system, the mass of the electron is far less than that of the atomic nucleus (about one thousandth), and the movement of the atomic nucleus is much slower than that of the

electron. Therefore, it can be considered that the atomic nucleus only makes small vibration near the equilibrium position, while the electron moves at a high speed outside the nucleus; Whenever the nucleus produces a small movement, the electrons around it can always be rapidly adjusted to a new equilibrium state. In this case, the motion of the nucleus and the electron in the multi particle system is considered to be independent of each other and can be treated separately: when studying the motion of the nucleus, the specific position of the electron in space need not be considered; When the motion of electrons is considered, the nucleus can be considered as stationary (instantaneous stationary). This approximate treatment method was proposed by German theoretical physicist Born and American physicist Oppenheimer, so it is called Born Oppenheimer approximation, also known as adiabatic approximation.[2]

Under the condition that only the motion of electrons is considered, the atomic nucleus can be regarded as static, the kinetic energy is zero, the multi particle system is simplified to the multi electron system, and the Hamiltonian and the corresponding Schrodinger equation can be written

$$H_0(\vec{r},\vec{R}) = H_e(\vec{r}) + V_N(\vec{R}) + H_{e-N}(\vec{r},\vec{R}) \tag{6}$$

$$H_0(\vec{r},\vec{R})\Phi_n(\vec{r},\vec{R}) = E_n(\vec{R})\Phi_n(\vec{r},\vec{R}) \tag{7}$$

Where n is the quantum number of the electronic state, the parameter $\vec{R}$ in the electronic wave function $\Phi_n(\vec{r},\vec{R})$ corresponds to the instantaneous position coordinate of the atomic nucleus, and the kinetic energy of the atomic nucleus can also be reintroduced as a perturbation.

2.4 Hartree-Fock (HF) approximation

Although the multi particle system has been successfully simplified into a multi electron system through the Born Oppenheimer approximation, due to the complex electron-electron interaction, it is still difficult to solve the Schrodinger equation of the multi electron system. In the multi electron system, any electron can be regarded as moving in the equivalent potential field generated by other electrons. The interaction energy between the electron and all other electrons is only related to the position of the electron. In 1928, Hartree of St. John's College proposed that the multi electron problem can be transformed into a single electron problem by averaging the Coulomb interaction between electrons (mean field).[3] Therefore, the wave function of the multi electron system can be expanded as the product of the single electron wave function, namely,

$$\phi(r) = \varphi_1(r_1)\varphi_2(r)\varphi_3(r_3)\cdots\varphi_n(r_n) \tag{8}$$

The above equation is also called Hartree wave function. Substitute equation (8) into the Schrodinger equation of multi electron system, and obtain the single electron equation by separating variables:

$$\left[-\nabla^2 + V(\vec{r}) + \sum_{i'(\neq i)} \int d\vec{r}' \frac{\left|\varphi_{i'}(\vec{r}')\right|^2}{\left|\vec{r}' - \vec{r}\right|}\right] \varphi_i(\vec{r}) = E_i \varphi_i(\vec{r}) \tag{9}$$

The above equation, also known as Hartree equation, describes the motion of a single electron (coordinate $\vec{r}$) in the lattice potential $V(\vec{r})$ and the average potential generated by all other electrons.

Although Hartree wave function satisfies Pauli exclusion principle and each electron has different quantum states, it ignores the Fermion property of the electron: when exchanging positions, the wave function of the electron must satisfy antisymmetry. In 1930, Fock used a series of linear combinations of single electron wave functions satisfying the commutative antisymmetry to represent the multi electron wave functions:[4]

$$\phi = \frac{1}{\sqrt{N!}} \begin{vmatrix} \varphi_1(\vec{q}_1) & \varphi_2(\vec{q}_2) & \cdots & \varphi_N(\vec{q}_1) \\ \varphi_1(\vec{q}_2) & \varphi_2(\vec{q}_2) & \cdots & \varphi_N(\vec{q}_2) \\ & \vdots & & \\ \varphi_1(\vec{q}_N) & \varphi_2(\vec{q}_N) & \cdots & \varphi_N(\vec{q}_N) \end{vmatrix} \tag{10}$$

Where $\vec{q}_i$ is the electron coordinate and is a function of position $\vec{r}_i$ and spin. Hartree Fock equation of single electron can be written:

$$\left[-\nabla^2 + V(\vec{r}) + \sum \int d\vec{r}' \frac{\rho(\vec{r}') - \rho_i^{HF}(\vec{r}, \vec{r}')}{\left|\vec{r}' - \vec{r}\right|}\right] \varphi_i(\vec{r}) = E_i \varphi_i(\vec{r}) \tag{11}$$

Since the orthogonality of the spin function leads to the sum of spins equal to zero, $\vec{r}_i$ is used instead of $\vec{q}_i$ in the above equation.

In Formula 11, the last two terms on the left are only related to the position vector $\vec{r}_i$ of the electron, which can be represented by a Coulomb effective potential field $V_{eff}(\vec{r})$ uniformly distributed for all electrons:

$$\left[-\nabla^2 + V_{eff}(\vec{r})\right] \varphi_i(\vec{r}) = E_i \varphi_i(\vec{r}) \tag{12}$$

Through Hartree Fock approximation, Schrodinger equation based on single electron effective potential can be used to replace Schrodinger equation of multi electron system. However, Hartree Fock approximation ignores the spin antiparallel repulsion between electrons and only considers the exchange interaction between electrons, so it cannot be used to strictly solve the single electron Schrodinger equation.

2.5 Hohenberg Kohn (HK) theorem

Hohenberg and Kohn proved two basic theorems in the study of non-uniform electron gas, which laid the foundation of DFT:[5]

Theorem 1: The ground state energy of the identical Fermion system without spin is the only functional of the particle number density function $\rho(\vec{r})$.

The particle number density here is defined as

$$\rho(\vec{r}) = \left\langle \Phi \left| \Psi^{+}(\vec{r}) \Psi(\vec{r}) \right| \Phi \right\rangle \tag{13}$$

Where Φ is the ground state wave function. Theorem 1 points out that the particle number density is a basic variable that determines the physical properties of the ground state of the multi particle system. Once the density function is determined, all the ground state properties of the system, including energy, wave function, etc., can be uniquely determined.

Theorem 2: When the number of particles is constant, the energy functional $E[\rho(\vec{r})]$ finds the extreme value of the particle number density function $\rho(\vec{r})$, which is equal to the ground state energy.

For a given local potential $v(\vec{r})$, the energy functional $E[\rho(\vec{r})]$ is defined as

$$E[\rho(\vec{r})] = \int d\vec{r} v(\vec{r}) \rho(\vec{r}) + \left\langle \Phi \left| T + U \right| \Phi \right\rangle \tag{14}$$

2.6 Kohn Sham (KS) equation

In the previous section, we mentioned that based on the HK theorem, the Hamiltonian of the system is unknown because of the kinetic energy functional of interaction and the form of electronic interaction. In order to solve the Schrodinger equation of the system, Kohn and Sham

simplified the interaction system as non-interaction.[5] Finally, the mathematical expression of Kohn Sham equation can be obtained:

$$\left\{-\nabla^2+v(\vec{r})+\int d\vec{r}'\frac{\rho(\vec{r}')}{|r-r'|}+\frac{\delta E_{xc}\left[\rho(\vec{r})\right]}{\delta\rho(\vec{r})}\right\}\psi_i(\vec{r})=E_i\psi_i(\vec{r}) \tag{15}$$

Where the effective potential is

$$\begin{aligned}V_{KS}(\vec{r}) &= v(\vec{r})+\int d\vec{r}'\frac{\rho(\vec{r}')}{|r-r'|}+\frac{\delta E_{xc}\left[\rho(\vec{r})\right]}{\delta\rho(\vec{r})}\\ &= v(\vec{r})+V_{coul}\left[\rho(\vec{r})\right]+V_{xc}\left[\rho(\vec{r})\right]\end{aligned} \tag{16}$$

Compared with Hartree Fock approximation, KS equation is derived from DFT theory and is accurate. The only item that cannot be determined is the exchange correlation item (XC) that contains all complex interactions. If the exact exchange correlation potential can be obtained, the exact ground state properties of the system can be solved by KS equation.

2.7 Exchange correlation potential

As discussed above, the solution of DFT finally focuses on the construction of exchange correlation potential. In general, the exchange correlation potential is related to the charge density distribution. In a broad sense, the exchange correlation potential is not local, but describes the properties of the spatial distribution, which makes it difficult to accurately construct the exchange correlation potential. So far, two mainstream approximation methods have been developed. The first is the local density approximation (LDA).[6] The second is the generalized gradient approximation (GGA).[7]

LDA regards the space charge density as a slow and continuous change function. This method simplifies the non-uniform electron gas system to a homogeneous case, and its exchange correlation potential has the following form:

$$E_{xc}\cong E_{xc}^{LDA}=\int\rho(\vec{r})\varepsilon_{xc}\left[\rho(\vec{r})\right]d\vec{r} \tag{17}$$

Where $\varepsilon_{xc}\left[\rho(\vec{r})\right]$ is the local exchange correlation energy density. In the local density approximation, the exchange correlation energy E_{xc}^{LDA} is decomposed into the exchange energy E_x and the correlation energy E_c. The former generally adopts the results of the homogeneous electron gas

model directly, while the expression of the latter needs to be obtained through quantum Monte Carlo simulation of the homogeneous electron gas model.

LDA method is relatively simple, and satisfactory results are obtained for systems with uniform electron density distribution, such as simple metals. However, because only the local charge distribution is considered, when dealing with systems with obvious changes in charge density, such as macromolecular systems, crystals dominated by covalent bonds, the calculated results have a large deviation from the actual values.

LDA neglects the interaction between various local electron gases, which leads to deviation in the calculation results. On the basis of LDA, GGA fully considers the interaction between different regions, and adds a gradient correction term to the exchange correlation functional that represents the charge density of the non-uniformity of the charge distribution. The exchange correlation energy of generalized gradient approximation can be written as:

$$E_{xc} \cong E_{xc}^{GGA} = \int \rho(\vec{r}) \varepsilon_{xc} \left[\rho(\vec{r}), \nabla \rho(\vec{r}) \right] d\vec{r} \tag{18}$$

In general, due to the correction of the non-uniformity of the charge density distribution, the results given by GGA are closer to the actual values for covalent crystals, macromolecules and other heterogeneous systems. However, it should be noted that GGA is not better than LDA in all cases, and the computation time of GGA will increase significantly.

2.8 Hybrid functional method

When calculating the electronic structure, there is no way to offset the correlation term and the exchange term, thus causing a large error. Using the hybrid functional method, the exact exchange term of Hartree Fock is added to the expression of the exchange correlation potential. Such hybrid functional forms include B3LYP, HSE03, HSE06, etc. At present, HSE06 is a hybrid functional that can more accurately describe the electronic structure of semiconductor. [8] The semi local GGA is expanded in a non-local way, and the exchange correlation energy of the hybrid functional is expressed as:

$$E_{XC}^{HSE} = \frac{1}{4} E_X^{SR}(\mu) + \frac{3}{4} E_X^{PBE,SR}(\mu) + E_X^{PBE,LR}(\mu) + E_C^{PBE} \tag{19}$$

Where μ is the shielding parameter, and the superscript SR/LR corresponds to the short range/long range action respectively. When the mixed parameter is 0, the HSE functional degenerates into Perdew–Burke–Ernzerhof (PBE) functional. When the shielding parameter μ tends to zero, the HSE functional is called PBE0 functional, while when the shielding parameter μ tends to infinity, the HSE functional still degenerates into PBE functional

2.9 VASP Package Introduction

VASP, fully known as Vienna ab initio Simulation Package, is a software package developed by the University of Vienna for electronic structure and ab initio molecular dynamics calculation and simulation, and is currently the most commonly used commercial software for computing condensed matter physics and computational material science. VASP obtains the wave function and energy of the system by approximately solving Schrodinger equation. VASP is based on the calculation of the pseudo potential plane wave basis set.[9,10] It uses the method of mode conservation pseudo potential, ultra-soft pseudo potential, and projection plus plane wave to express the pseudo interaction between electrons and ion entities. It uses the matrix diagonalization technique to solve the ground state wave function of electrons. The mixed density scheme of Pulay and Broyden is applied in the iterative solution, so as to accelerate the energy convergence of the self-consistent cycle. The main functions of VASP:

Periodic boundary conditions or supercell models are applied to deal with atoms, molecules, clusters, nanowires, films, surface systems and solids, specifically as follows: (1) atomic geometric structure parameters of materials: such as lattice constant, bond length, bond angle, atomic position, etc. (2) Mechanical properties of materials. (3) The electronic structure of the material. (4) Linear and nonlinear optical properties of materials. (5) The magnetism of the material. (6) Lattice dynamics of materials. (7) Dynamic simulation from scratch.

References

1 Born M, Oppenheimer R. Zur quantentheorie der molekeln. *Annalen der Physik*. **1927**;389:457-484.

2 Hartree D. The wave mechanics of an atom with a non-Coulomb central field. Part I. Theory and methods. *Mathematical Proceedings of the Cambridge Philosophical Society*. **1928**;24:89-110.

3 Fock V. Näherungsmethode zur Lösung des quantenmechanischen Mehrkörperproblems. *Zeitschrift für Physik*. **1930**;61:126-148.

4 Hohenberg P, Kohn W. Inhomogeneous electron gas. *Phys. Rev.* **1964**;136:B864.

5 Kohn W, Sham L. Self-consistent equations including exchange and correlation effects. *Phys. Rev*. **1965**;140:A1133.

6 Langreth D. Perdew J. Theory of nonuniform electronic systems. I. Analysis of the gradient approximation and a generalization that works. *Phys. Rev. B*. **1980**;21:5469.

7 Giannozzi P, Baroni S, Bonini N, et al. QUANTUM ESPRESSO: a modular and open-source software project for quantum simulations of materials. *J. Phys-Condens. Mat*. **2009**;V21:395502.

8 Heyd J, Scuseria G, Ernzerhof M. Hybrid functionals based on a screened Coulomb potential. *J. Chem. Phys.* **2003**;118:8207-8215.

9 Kresse G, Furthmuller J. Efficient iterative schemes for ab initio total-energy calculations using a plane-wave basis set. *Phys. Rev. B*. **1996**;54:11169-11186.

10 Kresse G, Furthmuller J. Efficiency of ab-initio total energy calculations for metals and semiconductors using a plane-wave basis set. *Comp. Mat. Sci*. **1996**;6:15-50.

Chapter 3. DFT study of X-site ion substitution doping of Cs_2PtX_6 on structural and electronic properties

3.1 Introduction

The inorganic-organic hybrid perovskites solar cells (HPSCs), which are expected to generate renewable resources and resolve global energy problems because of their favorable properties including low cost, superior absorption coefficient[1,2], appropriate band gap and easy fabrication process.[3,4] The power conversion efficiencies (PCEs) achieved by these materials have steadily improved and currently reach 25.5%.[5] The chemical formula of this kind of perovskite is ABX_3, where A is inorganic ion (Cs^+, Rb^+ or K^+) or monovalent organic cation (MA^+, $CH(NH_2)^{2+}$(FA)), B is divalent cation (Ge^{2+}, Sn^{2+} or Pb^{2+}) and X is halide ion (I^-, Br^- or Cl^-).[6,7] The cations A and B are combined with 12 and 6 X, respectively.[8,9] Although superior photovoltaic properties have been realized, some challenges still exist with the HPSCs, i.e., the toxicity of lead (Pb), and the perovskites that suffer from a poor chemical stability in air.[10,11] Replacing organic components in the perovskite materials with inorganic components may be an ultimate solution to the problem of thermal instability.[12-14]Therefore, many researchers have developed a new type of all inorganic Cs-based halogenated perovskite $CsBX_3$ by oxygen evolution in water. The decomposition of the compounds can be retarded by replacing the organic cations with inorganic cesium ions.[15-17] On the other hand, to avoid the toxicity of lead, this has stimulated research into using alternative materials instead of lead for the perovskite compounds. The double and vacancy ordered perovskites have appeared with general formulas $A^{+1}{}_2B^{+1}B'^{+3}X_6$ and $A^{+1}{}_2B^{+4}X_6$ respectively, and have many potential applications in optoelectronics and hybrid perovskite halides due to better stability and low toxicity than the traditional ABX_3 perovskites.[18-20] Besides, the advantage that they can be simply prepared into thin films has also attracted the attention of scientists in the field of optoelectronics. Accordingly calculating the physical properties of novel double perovskite will have a wide application prospect.[21] Bahmad et al. studied the magnetic properties, magnetizations and magnetic susceptibilities, and phase diagrams of double perovskite

Sr_2VMoO_6 and Sr_2RuHoO_6 using the Monte Carlo Simulation.[22,23] Mahmood et al. studied the optoelectronics and thermoelectric applications of lead-free double perovskites halides Cs_2TiCl_6 and Cs_2TiBr_6 using density functional theory.[24] Galin et al. simulated the oxygen diffusion in the solid solutions of $PrBaCo_2O_{5.5}$-based double perovskites by the molecular dynamics method.[25] In recent years, many efforts have been extensively made to study the photoelectricity of the A_2BX_6 type. In this double perovskite structure, the selection of atoms with varying ion radii can significantly affect the diverse physical properties displayed. Such a unique performance adjustment method can produce optoelectronic devices, magnetoelectric memory and multifunctional spintronics.[26,27] If half of the B ions in the center of the $[BX_6]$ cluster are removed, the checkered pattern of A_2BX_6 can be regarded as a derivative of the ABX_3 structure.[28] The selection of the B-site cation has been reported as Sn and Te with an infrared light absorption ability, and can also be transition metal elements of the +4 states such as Pt.[29-31]

Our group[10] has synthesized large-size Cs_2PtI_6 single crystal and high-quality Cs_2PtI_6 thin film by a simple method and studied its photovoltaic properties. In the same year, Maike et al.[32] and Sajjad et al.[33] explored the extraordinary stability of Cs_2PtI_6 in various environments by means of experiment and first principle calculation. For photovoltaic applications, the cost of Pt may be considered prohibitively high. However, Pt provides an excellent model for the substitution of Pb, and Pt based perovskite can be used as interface modification material. Similar to traditional perovskite, halide based double perovskite has been proved to adjust the band gap to optimize the photoelectric properties because ion substitution can produce metal to insulation properties. The substitution and doping of the X-site halogen in Cs_2PtX_6 (X= Cl, Br, I) will also affect the electronic properties of these perovskites. Based on the understanding of the crystal structure and chemical composition of the perovskite compounds, novel perovskite materials for efficient photovoltaic applications can be found by calculation methods such as the density functional theory (DFT). Zeng et al. predicted a series of $Cs_2TiI_xBr_{6-x}$ (x = 0, 2, 4, 6) lead-free halide perovskites for solar cells applications based on DFT, and the results were confirmed by experimental efforts.[34] Mahmood et al. calculated that bromine substituted chlorine has a great influence on the optical and thermoelectric properties in novel double perovskite Rb_2PtX_6, which is almost consistent with the experimental results.[35] Consequently, the theoretical study of these double perovskites can provide a basis for exploring novel device applications.

In this paper, we simulated and optimized the structure of the $Cs_2PtI_{6-y}Cl_y$, $Cs_2PtI_{6-y}Br_y$, $Cs_2PtBr_{6-y}Cl_y$ (y = 0, 1, 2, 3, 4, 5, 6) and systematically studied their electronic properties by using the generalized gradient approximation of the Perdew–Burke–Ernzerhof (PBE) functional of projector augmented waves (PAW). This function can save calculation time, but it is not accurate when calculating the solid band gap. Therefore, the band gap was calculated with the help of the Heyd-Scuseria-Ernzerhof hybrid functional (HSE06), and we have achieved a good balance between a reasonable computational cost and accuracy of the results. According to the predicted band gap variation law, we selected some perovskites for further calculation using the more accurate but also computationally more expensive HSE06 functional. This work provided a good theoretical foundation for understanding the structural and electronic properties of these compounds. Moreover, the results of the theoretical calculations can provide a rough prediction for the experimental work, reduce the time cost of experimental exploration and avoid meaningless consumptions of the raw materials.

3.2 Computational details

In this study, we used the first principles DFT by the Vienna Ab initio simulation package (VASP) code with a plane-wave basis set.[36] Both the generalized gradient approximation (GGA) of the PBE functional and HSE06 have been used to calculate the structural and electronic properties.[37,38] The atomic pseudo potential was described by the PAW method.[39] The electronic configurations of the Cs, Pt, I, Br and Cl atoms are $[Xe]6s^1$, $[Xe]5d^96s^1$, $[Kr]4d^{10}5s^25p^5$, $[Ar]3d^{10}4s^24p^5$ and $[Ne]3s^23p^5$, respectively. All the structures considered in this paper are fully relaxed using the conjugate gradient algorithm until the total electronic energy and force converge on individual ion was less than $0.1e^{-4}$ eV and 0.001 eV/Å, respectively. The energy cutoff for the plane wave basis for all compounds was set to 400 eV. The grid of k-points employed for computing integrals over the Brillouin zone for geometry optimizations and density of states calculations was taken as 4×4×4. The original models and substitutional doping models of the Cs_2PtX_6 (X= Cl, Br, I) perovskites were established by Vesta. According to the predicted band gap variation law, we selected Cs_2PtCl_6, Cs_2PtBr_6, Cs_2PtI_6 and Cs_2PtICl_5 for further calculation using the more accurate but also computationally more expensive HSE06 method.

3.3 Results and discussions

As illustrated in Fig. 1a, the Cs_2PtX_6 (X= Cl, Br, I) has a face centered cubic structure with space group Fm3m (No.225), which is alternately formed by isolated [PtX_6] clusters and twisted tetragonal Cs cations (space group P4/mnc). In this figure, the $[PtX_6]^{4-}$ octahedra are shaded with the purple balls in the corners representing halogen. The Cs cations are green balls that are located in the center of 12 halogen ions, and the Pt cations are silver balls and located in the center of the octahedron. The perovskite primitive cell with 9 atoms was chosen as single halogen substitution structure (Fig. 1b). First of all, we need to build the models of $Cs_2PtBr_yCl_{6-y}$, $Cs_2PtI_yBr_{6-y}$ and $Cs_2PtI_yCl_{6-y}$ (y = 0, 1, 2, 3, 4, 5, 6). After consulting the relevant crystal databases and references, we did not find a single halogen doped Cs_2PtX_6 model. Based on the known crystal As illustrated in Fig. 1a, the Cs_2PtX_6 (X= Cl, Br, I) has a face centered cubic structure with space group Fm3m (No.225), which is alternately formed by isolated [PtX_6] clusters and twisted tetragonal Cs cations (space group P4/mnc). In this figure, the $[PtX_6]^{4-}$ octahedra are shaded with the purple balls in the corners representing halogen. The Cs cations are green balls that are located in the center of 12 halogen ions, and the Pt cations are silver balls and located in the center of the octahedron. The perovskite primitive cell with 9 atoms was chosen as single halogen substitution structure (Fig. 1b). First of all, we need to build the models of $Cs_2PtBr_yCl_{6-y}$, $Cs_2PtI_yBr_{6-y}$ and $Cs_2PtI_yCl_{6-y}$ (y = 0, 1, 2, 3, 4, 5, 6). After consulting the relevant crystal databases and references, we did not find a single halogen doped Cs_2PtX_6 model. Based on the known crystal models of Cs_2PtCl_6, Cs_2PtBr_6 and Cs_2PtI_6, the X-site atoms of Cs_2PtX_6 are substituted in a primitive cell, so that we constructed the theoretical calculation doped models. Table 1 shows the lattice constant and formation energy of Cs_2PtX_6 calculated by the semi-local GGA-PBE functional. The lattice constant of the undoped symmetrical cells of Cs_2PtCl_6, Cs_2PtBr_6 and Cs_2PtI_6 are 10.35 Å, 11.04 Å and 11.67 Å respectively, which are close to the experimental values (Cs_2PtCl_6: 10.19 Å, Cs_2PtBr_6: 10.67 Å, Cs_2PtI_6: 11.37 Å),[40-42] indicating that the parameters and models we used are reasonable. We further used another halogen with different doping concentrations to replace the X-site cations to build the lattice model of Cs_2PtX_6. It can be seen from Table 1 that halogen ions with a small doping radius will reduce the crystal lattice constant and the cell volume (ion radius: $I^- > Br^- > Cl^-$).

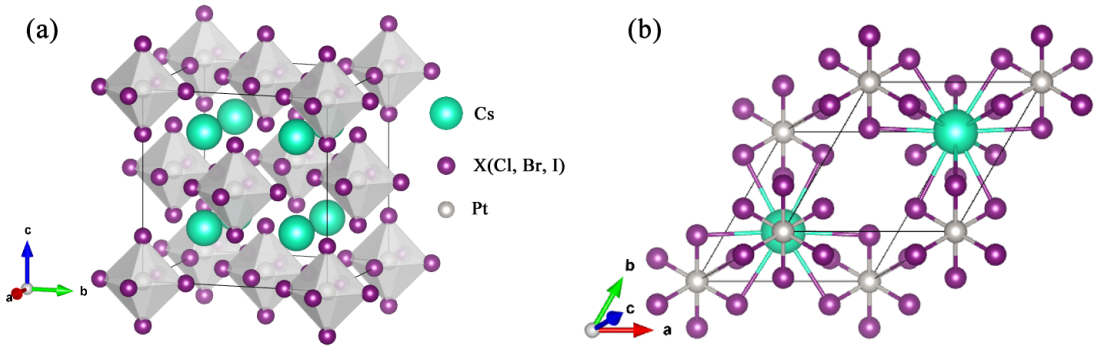

Figure. 1. (a) Schematic crystal structure of Cs_2PtX_6 (X=Cl, Br, I) with PtX_6 octahedral structure. (b) Primitive cell structure of Cs_2PtX_6. Structures visualized with the support of VESTA.

Table 1. Optimized lattice parameters and formation energy of different concentration ratios of halogen doped in Cs_2PtX_6 (X= Cl, Br, I) primitive cell.

Compound	*a* (Å)	*Volume* (Å^3)	*Formation Energy* (eV)
Cs_2PtCl_6	7.32	277.16	-11.25
$Cs_2PtBrCl_5$	7.42	288.47	-11.04
$Cs_2PtBr_2Cl_4$	7.50	297.93	-10.85
$Cs_2PtBr_3Cl_3$	7.58	307.45	-10.67
$Cs_2PtBr_4Cl_2$	7.65	316.30	-10.48
Cs_2PtBr_5Cl	7.72	325.78	-10.29
Cs_2PtBr_6	7.81	337.21	-10.11
Cs_2PtIBr_5	7.86	343.87	-9.64
$Cs_2PtI_2Br_4$	7.98	359.85	-9.18
$Cs_2PtI_3Br_3$	8.05	368.89	-8.70
$Cs_2PtI_4Br_2$	8.11	377.01	-8.27
Cs_2PtI_5Br	8.19	388.27	-7.86
Cs_2PtI_6	8.25	397.19	-7.44
Cs_2PtI_5Cl	8.15	382.81	-8.02
$Cs_2PtI_4Cl_2$	7.99	360.54	-8.61

$Cs_2PtI_3Cl_3$	7.85	341.57	-9.20
$Cs_2PtI_2Cl_4$	7.82	337.90	-9.88
Cs_2PtICl_5	7.64	315.04	-10.52

Except for the lattice constants, we also calculated the Goldschmidt's tolerance factor (τ) to study the structural properties of crystal using the following equation[43,44]:

$$\tau = \frac{R_A + R_X}{\sqrt{2}(R_B + R_X)} \quad (1)$$

where R_A, R_B and R_X denote the ionic radius of the A, B and X in the A_2BX_6 double perovskite structure, respectively. The τ evaluated whether the A-Site atoms can stabilize the frame of the octahedron $[BX_6]^{4-}$. For the Cs_2PtX_6 perovskites, the corresponding Shannon ionic radii of Cs^+, Pt^{2+}, Cl^-, Br^- and I^- are 1.67, 0.62, 1.81, 1.96, 2.2 Å, respectively. The value of τ is between 0.813 and 1.106, which matches with the higher symmetry.[45] It can be seen from Fig. 2 that the τ of all the compounds ranged from 0.97 to 1.013, meeting the constraint conditions given by the definition and indicating that the perovskites are stable at room temperature in the cubic form.

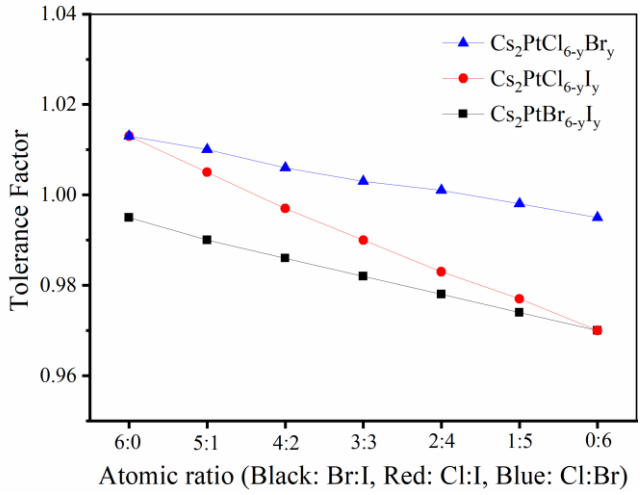

Figure. 2. The tolerance factor of Cs_2PtX_6 (X=Cl, Br, I) varies with the ratio of X doping. The abscissa represents the ratio of two halogens in the compounds.

It was necessary to calculate τ for predicting the structural stability of the perovskites, however, the structural stability alone is not enough to judge whether a perovskite can be formed. Therefore, in order to evaluate the thermodynamic stability, we calculated the formation energy (E_f) of the undoped and halogen doped Cs_2PtX_6 perovskites.[12,46] The E_f

can be defined as the difference between the total energy of the compound and the sum of the energies of the main components in the standard form, and the formula is given by

$$E_{\mathrm{f}} = E_{\mathrm{bulk}} - n_{Cs}E_{\mathrm{atom}}^{\mathrm{Cs}} - n_{Pt}E_{\mathrm{atom}}^{\mathrm{Pt}} - n_{Cl}E_{\mathrm{atom}}^{\mathrm{Cl}} - n_{Br}E_{\mathrm{atom}}^{\mathrm{Br}} - n_{I}E_{\mathrm{atom}}^{\mathrm{I}} \quad (2)$$

in which E_{bulk} is the total energy of Cs_2PtX_6; E_{atom} represents the energy of the free atom k (k = Cs, Pt, I, Br, and Cl), and n_k is the number of atoms k in the primitive cell. The obtained calculation results are listed in Table 1 and Fig. 3, which show that the formation energy varies with the ratio of the X doping. All compounds in our research have negative formation energies, indicating that the compounds can be synthesized under the given environmental conditions.[28] The lower the formation energy, the easier the compound is to be formed and the more stable it is.[46,47] Comparing the data in Table 1, we noticed that Cs_2PtI_6 has the most unstable structure but doping Cl^- and Br^- can significantly reduce the formation energy and improve the thermodynamic stability of the cell. It can be obviously seen from Fig. 3, when Cs_2PtX_6 is substitution doped with a halogen having a small radius, the formation energy will decrease, thus improving the stability of the cell.

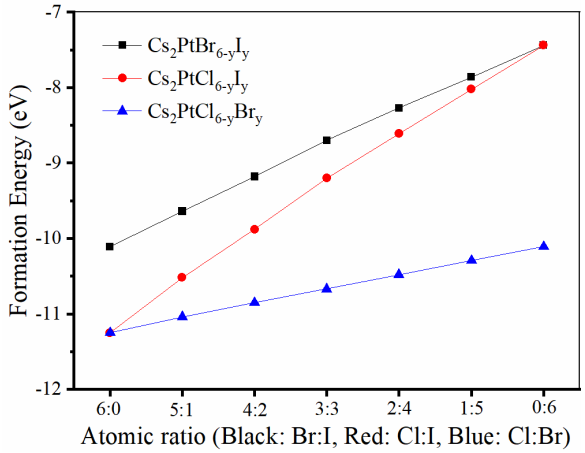

Figure. 3. The formation energy of Cs_2PtX_6 (X=Cl, Br, I) varies with the ratio of X doping. The abscissa represents the ratio of two halogens in the compounds.

Table 2. Calculated band gaps with PBE (GGA) and HSE06 functional of halogen substitution doped Cs_2PtX_6 (X= Cl, Br, I) compounds perovskites.

Compound	E_g (GGA-PBE)/eV	E_g (HSE06)/eV
Cs_2PtCl_6	2.02	3.31
$Cs_2PtBrCl_5$	1.78	

$Cs_2PtBr_2Cl_4$	1.68	
$Cs_2PtBr_3Cl_3$	1.58	
$Cs_2PtBr_4Cl_2$	1.51	
Cs_2PtBr_5Cl	1.46	
Cs_2PtBr_6	1.45	2.33
Cs_2PtIBr_5	1.07	
$Cs_2PtI_2Br_4$	0.97	
$Cs_2PtI_3Br_3$	0.87	
$Cs_2PtI_4Br_2$	0.80	
Cs_2PtI_5Br	0.63	
Cs_2PtI_6	0.61	1.39
Cs_2PtI_5Cl	0.69	
$Cs_2PtI_4Cl_2$	0.87	
$Cs_2PtI_3Cl_3$	1.02	
$Cs_2PtI_2Cl_4$	1.13	
Cs_2PtICl_5	1.30	2.07

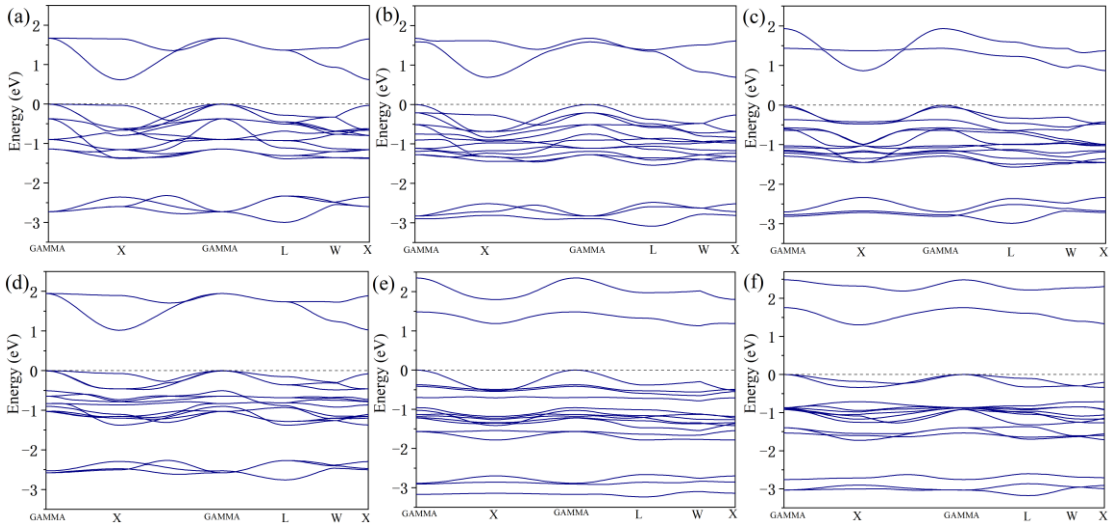

Figure. 4. Band structures of the (a) Cs_2PtI_6, (b) Cs_2PtI_5Cl, (c) $Cs_2PtI_4Cl_2$, (d) $Cs_2PtI_3Cl_3$, (e) $Cs_2PtI_2Cl_4$ and (f) Cs_2PtICl_5 calculated by PBE functional.

In order to investigate the latent changing tendency of the halogen doped Cs_2PtX_6 perovskites, we calculated the band structure and density of states (DOS) of each perovskite. Based on the relaxed structures, the band gaps were calculated by PBE functional and listed in Table 2 in the span range of 0.61 to 2.02 eV. For $Cs_2PtI_yCl_{6-y}$, $Cs_2PtI_yBr_{6-y}$, and $Cs_2PtBr_yCl_{6-y}$ (y = 0, 1, 2, 3, 4, 5, 6), the band structures are shown in Fig. 4, Fig. 5 and Fig. 6, respectively. It can be seen from the $Cs_2PtI_yCl_{6-y}$, the indirect band gap of Cs_2PtI_6 was estimated to be 0.61 eV, which is in favorable agreement with the value reported in the Materials Projects and the literature using a similar computational approach.[21] In addition, we found that the type of band gap of the $Cs_2PtBr_yCl_{6-y}$ and $Cs_2PtI_yCl_{6-y}$ changed from direct to indirect when y is from 0 to 1 in Fig. 4 and Fig. 6, and all the other perovskites have indirect band structure, conduction band minimum (CBM) and the valence band maximum (VBM) are at the X point and GAMMA point, respectively. This phenomenon indicated that the doping of a halogen will change the band structure type of Cs_2PtCl_6, but not destroy the main characteristics of the band structure of the other compounds.

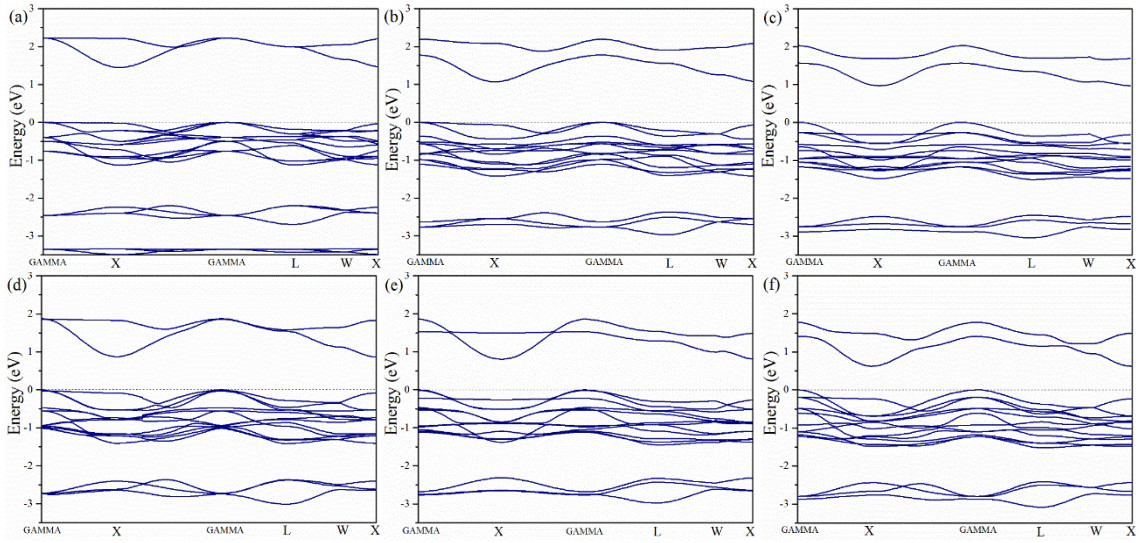

Figure. 5. Band structures of the (a) Cs_2PtBr_6, (b) Cs_2PtIBr_5, (c) $Cs_2PtI_2Br_4$, (d) $Cs_2PtI_3Br_3$, (e) $Cs_2PtI_4Br_2$ and (f) Cs_2PtI_5Br calculated by PBE functional.

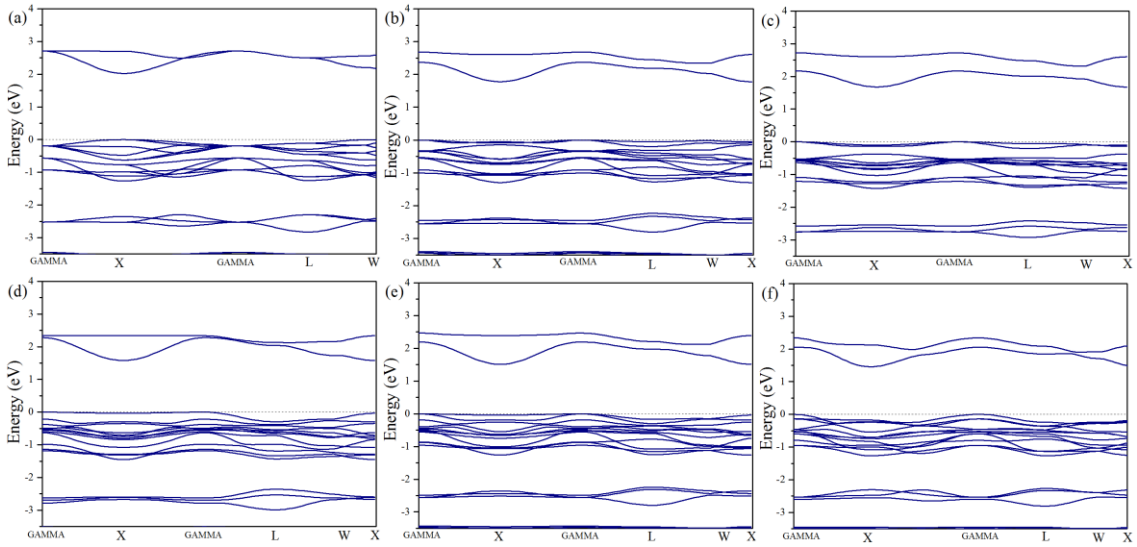

Figure. 6. Band structures of the (a) Cs_2PtCl_6, (b) $Cs_2PtBrCl_5$, (c) $Cs_2PtBr_2Cl_4$, (d) $Cs_2PtBr_3Cl_3$, (e) $Cs_2PtBr_4Cl_2$ and (f) Cs_2PtBr_5Cl calculated by PBE functional.

In our research, Cs_2PtI_6 has the narrowest band gap, while Cs_2PtCl_6 has the largest value of band gap. The present calculation results show an obvious trend with the size of the X-site anion in Fig. 7. In the $[PtX_6]^{4-}$ octahedron, the lighter Cl^- is replaced by the heavier Br^- and I^-, resulting in the enhanced interaction between Pt and X-site anions, which have an important impact on the characteristics of the band structure. Owing to electronegativity (Cl > Br > I) and atomic radius (I > Br > Cl), the difference of the Pt-Cl distance is more significant than that of Pt-Br and Pt-I, which leads to the larger band gap of the Cl^- doped perovskite than that of the other halogen doped perovskites.[28,48] The electronic properties of the different concentration ratios of halogen doping in Cs_2PtX_6 (X= Cl, Br, I) are further explained by the DOS.

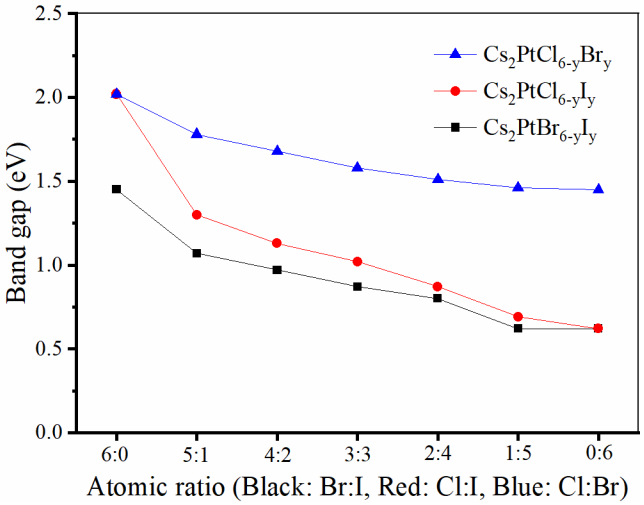

Figure. 7. The band gap (calculated by PBE method) of Cs_2PtX_6 varies with the ratio of X doping (X=Cl, Br, I). The abscissa represents the ratio of two halogens in the compounds.

Figure 8, 9 and 10 show the calculated DOS of the $Cs_2PtI_yCl_{6-y}$, $Cs_2PtI_yBr_{6-y}$ and $Cs_2PtBr_yCl_{6-y}$ perovskites, respectively, and the Fermi energy is set to zero. All the materials exhibit semiconductor properties because the valence band of DOS does not cross over the Fermi level. The analysis of the orbital characteristics of Cs_2PtI_6 shows that the VBM is mainly contributed by the I-p orbitals and a small contribution of Pt-d, while the CBM also consists of the interaction of Pt-d orbitals with I-p orbitals. The contribution of the Cs orbitals of all materials in the total density of states (TDOS) is unimportant in both the valence band and conduction band. When I atom is replaced by Cl or Br atom, we can see similar pattern with a few differences in the partial density of states (PDOS) diagram. From Fig. 8, it is clear that the p orbitals of Cl will contribute more and more to the valence and conduction bands when the doping concentration increases, and which sits back quite deep in the valence band, resulting in the movement of PDOS towards lower energy. With the increasing content of Br^- and I^-, the contribution of the heavier halogen tends to be close to the Fermi energy, leading to decrease of the band gap. The electrostatic force of valence electrons in nucleus will weaken with the increase of atomic radius, which will reduce the energy between valence band and conduction band. Therefore, for the narrow bandgaps, only a small amount of incident energy is needed to excite the bound electron guide band to move to the free conduction state.[49,50] Almost all the bandgap transitions of these

compounds occur in the mixed state from the X-p and Pt-d orbital of the conduction band to the X-p orbital of the valence band.

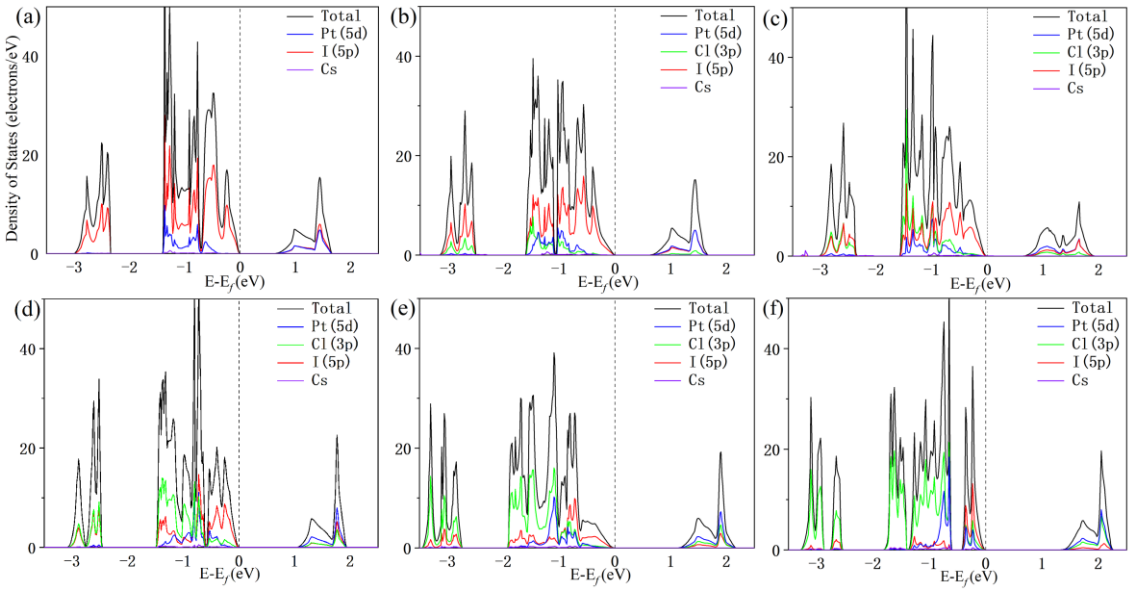

Figure. 8. The density of states (DOS) of the (a) Cs_2PtI_6, (b) Cs_2PtI_5Cl, (c) $Cs_2PtI_4Cl_2$, (d) $Cs_2PtI_3Cl_3$, (e) $Cs_2PtI_2Cl_4$ and (f) Cs_2PtICl_5.

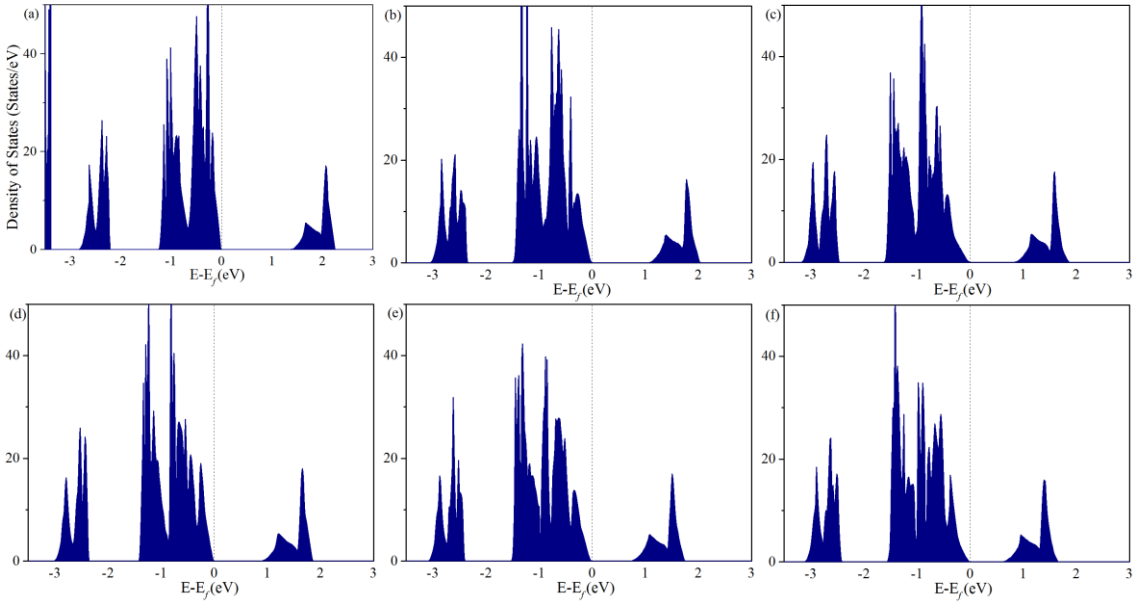

Figure. 9. Density of states (DOS) of the (a) Cs_2PtBr_6, (b) Cs_2PtIBr_5, (c) $Cs_2PtI_2Br_4$, (d) $Cs_2PtI_3Br_3$, (e) $Cs_2PtI_4Br_2$ and (f) Cs_2PtI_5Br.

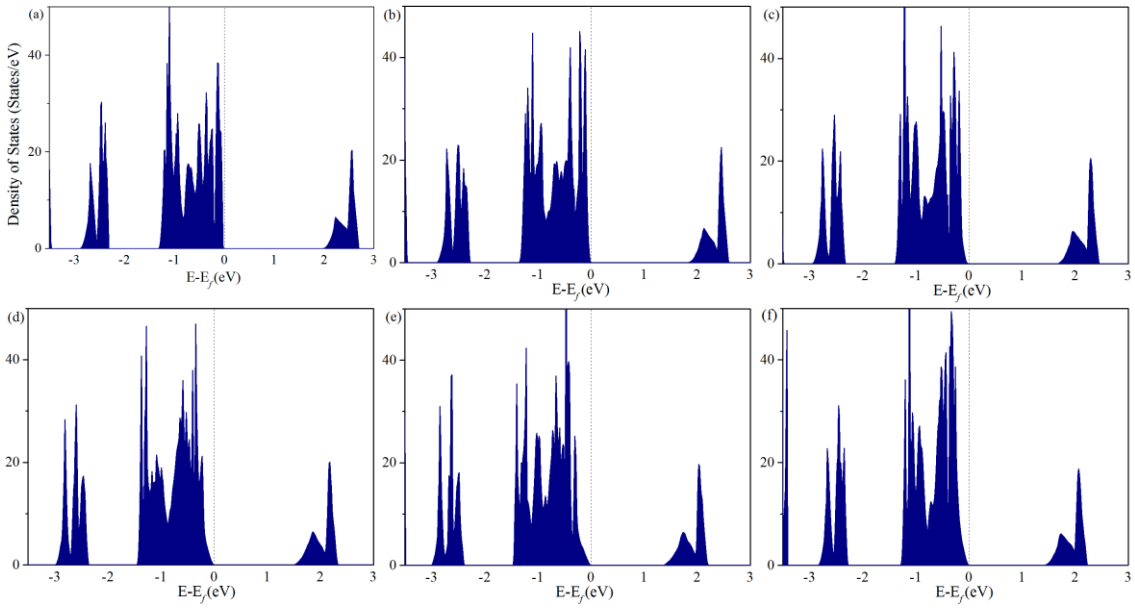

Figure. 10. Density of states (DOS) of the (a) Cs_2PtCl_6, (b) $Cs_2PtBrCl_5$, (c) $Cs_2PtBr_2Cl_4$, (d) $Cs_2PtBr_3Cl_3$, (e) $Cs_2PtBr_4Cl_2$ and (f) Cs_2PtBr_5Cl.

Since the PBE functional tends to underestimate the bandgaps, the variation law of bandgaps was used as a screening criterion for further calculations based on HSE06 level. With the consideration of the computational cost, we only calculate the hybrid-functional band structure of Cs_2PtCl_6, Cs_2PtBr_6, Cs_2PtI_6 and Cs_2PtICl_5. Fig.11 shows the HSE band structures of the four perovskites selected as representatives. It is worth mentioning that although the bandgap values calculated by the two methods are different, they have similar band structures. It can be seen from Table 2 that the hybrid functional band gaps of the four perovskites are 3.31 eV, 2.33 eV, 1.39 eV and 2.07 eV, respectively. As for Cs_2PtI_6, the calculated HSE bandgap is 1.39 eV, which is roughly consistent in experimental value of 1.37 eV, proving the reliability of the calculation results.[10] According to the trend in the bandgaps calculated by PBE method, we can predict that other unscanned HSE bandgaps of the compounds will change in a small range. The band gap of $Cs_2PtI_yCl_{6-y}$ is between 1.39 eV and 3.31 eV, while that of $Cs_2PtI_yBr_{6-y}$ and $Cs_2PtBr_yCl_{6-y}$ are from 1.39 to 2.33 eV and 2.33 to 3.31 eV, respectively. The range of the bandgaps for the most potential candidates is usually between 1.0 eV and 1.9 eV. Considering that the results of HSE06 functional calculation slightly overestimate the band gap, the $Cs_2PtI_yBr_{6-y}$ and $Cs_2PtI_yCl_{6-y}$ with appropriate band gap may be potentially ideal for pure perovskite and tandem perovskite solar cell materials.

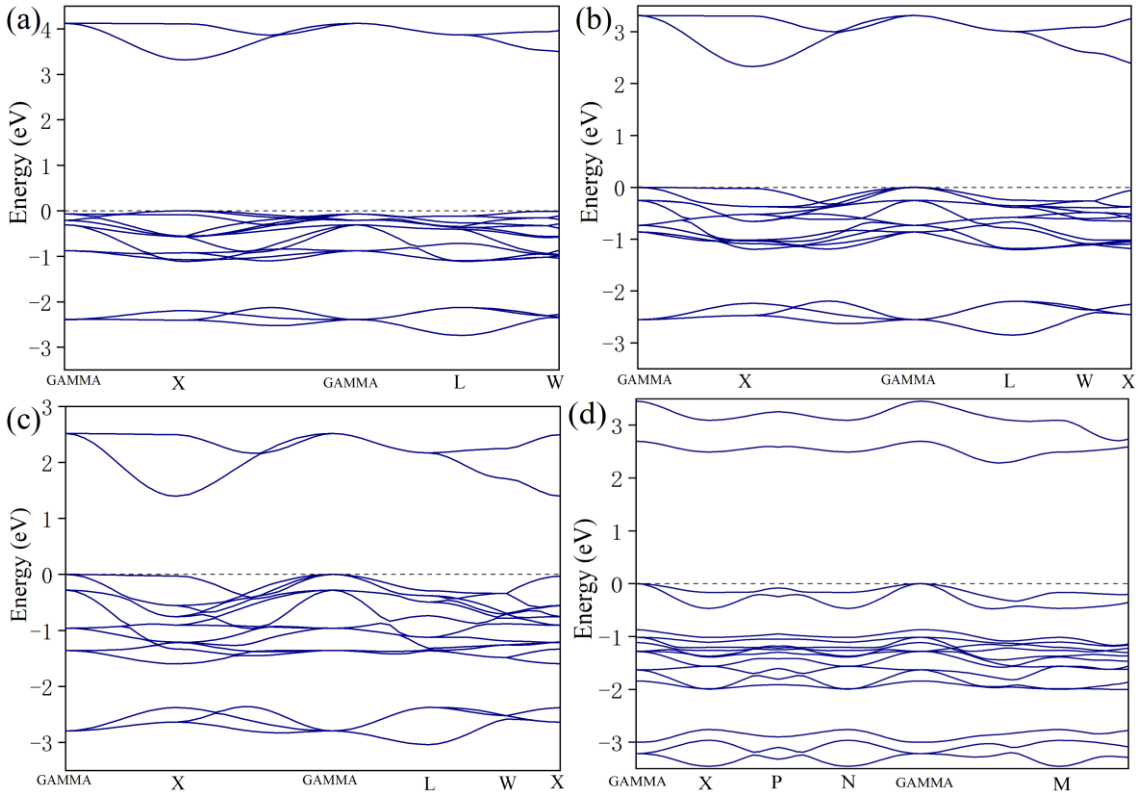

Figure. 11. Band structures of the (a) Cs_2PtCl_6, (b) Cs_2PtBr_6, (c) Cs_2PtI_6, (d) Cs_2PtICl_5 calculated by HSE06 functional.

3.4 Conclusions

In summary, we have successfully investigated the structure, stability and electronic properties of $Cs_2PtBr_yCl_{6-y}$, $Cs_2PtI_yBr_{6-y}$, and $Cs_2PtI_yCl_{6-y}$ (y = 0, 1, 2, 3, 4, 5, 6) using DFT calculations, 18 perovskites in total. Based on the structural analysis, both the crystal lattice constant and the cell volume of Cs_2PtX_6 (X= Cl, Br, I) suffer a monotonic increase with the decreasing content of halogen ions with small doping radii. In the study of the stability, the calculated tolerance factors for all the perovskites are well within the specified range. The formation energies of all the compounds are negative. Moreover, the value of formation energy of investigated Cs_2PtX_6 perovskites with higher Cl^- content is lower, which indicates that the thermodynamic stability of structure can be improved by replacing the I^- or Br^- with an appropriate amount of Cl^-. The electronic properties based on PBE level results show that the band gap tends to increase when I^- is replaced by Cl^- and Br^- in the halogen substitution of the X-site. Furthermore, $Cs_2PtI_yBr_{6-y}$ and $Cs_2PtI_yCl_{6-y}$ (Except Cs_2PtCl_6)

have band gap values of 1.3-2.3 eV calculated by HSE06 functional, indicating that they have the potential to be used in perovskite and tandem perovskite solar cells. Based on this work, the general trends in bandgaps and stability are anticipated to provide a guideline for the design of novel stable inorganic halide perovskite materials with ideal properties.

References

1 A. Kojima, K. Teshima, Y. Shirai and T. Miyasaka. Organometal halide perovskites as visible-light sensitizers for photovoltaic cells. *J. Am. Chem. Soc.*, **2009**, 131, 6050-6051.

2 J. Burschka, N. Pellet, S.J. Moon, R. Humphry-Baker, P. Gao, M.K. Nazeeruddin and M. Grätzel. Sequential deposition as a route to high-performance perovskite-sensitized solar cells. *Nature*, **2013**, 499**,** 316-319.

3 Y. Zhang, J. Wen, Z. Xu, D. Liu, T. Yang, T. Niu, T. Luo, J. Lu, J. Fang, X. Chang, K. Zhao and S. (Frank) Liu. Effective phase‐alignment for 2D halide perovskites incorporating symmetric diammonium ion for photovoltaics. *Adv. Sci.*, **2021**, 8, 2001433.

4 J. Zhang, Y. Xuan, L. Yang. A novel choice for the photovoltaic–thermoelectric hybrid system: the perovskite solar cell. *Int. J. Energ. Res.,* **2016**, 40, 1400-1409.

5 Best Research-Cell Efficiency Chart, Photovoltaic Research NREL, https://www.nrel.gov/pv/assets/pdfs/cell-pv-eff-emergingpv.202001042.pdf.

6 M. Jiang, N. Deng, L. Wang, H. Xie and Y. Qiu. The structural, electronic, and optical properties of organic–inorganic mixed halide perovskites $CH_3NH_3Pb\ (I_{1-y}X_y)_3$ (X= Cl, Br). *Chinese Phys B*, **2018**, 27, 067102.

7 G. Wang, S. Dang, P. Zhang, S. Xiao, C. Wang and M. Zhong. Hybrid density functional study on the photocatalytic properties of AlN/$MoSe_2$, AlN/WS_2, and AlN/WSe_2 heterojunctions. *J. Phys. D: Appl. Phys.*, **2018**, 51, 025109.

8 H.J. Snaith. Present status and future prospects of perovskite photovoltaics. *Nat. Mater.*, **2018**, 17, 372-376.

9 H. Fu. Review of lead-free halide perovskites as light-absorbers for photovoltaic applications: From materials to solar. *Sol. Energy Mater. Sol. Cells*, **2019**, 193, 107-132.

10 S. Yang, X. Song, L. Gao, N. Wang, X. Ding, S. Wang and T. Ma. Novel Lead-Free Material Cs2PtI6 with Narrow Bandgap and Ultra-Stability for Its Photovoltaic Application. *ACS Appl. Mater. Interfaces*, **2020**, 40**,** 44700-44709.

11 A. Latini, G. Gigli and A. Ciccioli. A study on the nature of the thermal decomposition of methylammonium lead iodide perovskite, $CH_3NH_3PbI_3$: an attempt to rationalise contradictory experimental results. *Sustain. Energy Fuels*, **2017**, 6, 1351-1357.

12 J. An, H. Jiang, Y. Tian, H. Xue and F. Tang. Manganese doping mechanism in a $CsPbI_2Br$ photovoltaic material: a first-principles study. *Phys. Chem. Chem. Phys.*, **2019**, 21, 23552-23558.

13 D.P. McMeekin, G. Sadoughi, W. Rehman, G.E. Eperon, M. Saliba, M.T. Horantner, A. Haghighirad, N. Sakai, L. Korte, B. Rech, M.B. Johnston, L.M. Herz and H. J. Snaith. A mixed-cation lead mixed-halide perovskite absorber for tandem solar cells. *Science*, **2016**, 351, 151-155.

14 R.F. Service. Cesium fortifies next-generation solar cells. *Science*, **2016**, 351, 113-114.

15 S. Liu, Y.J. Guan, Y.S. Sheng, Y. Hu, Y.G. Rong, A.Y. Mei and H.W. Han. A review on additives for halide perovskite solar cells. *Adv. Energy Mater.*, **2020**, 10, 1902492.

16 G. Tong, L.K. Ono and Y. Qi. *Energy Technol*., **2020**, 8, 1900961.

17 I. Poli, U. Hintermair, M. Regue, S. Kumar, E.V. Sackville, J. Baker, T.M. Watson, S. Eslava and P.J. Cameron. Recent Progress of All-Bromide Inorganic Perovskite Solar Cells. *Nat. Commun.*, **2019**, 10, 2097.

18 A. Kumar, S.K. Swami, S.S. Rawat, V.N. Singh, R. Srivastava. Mixed bismuth-antimony-based double perovskite nanocrystals for solar cell application. *Int. J. Energ. Res.*, **2021**, 45, 16769-16780.

19 H.N. Chen, S.S. Xiang, W.P. Li, H.C. Liu, L.Q. Zhu and S.H. Yang. Inorganic Perovskite Solar Cells: A Rapidly Growing Field. *Sol. Rel.*, **2018**, 2, 1700188.

20 A.E. Maughan, A.M. Ganose, M.M. Bordelon, E.M. Miller, D.O. Scanlon and J.R. Neilson. Defect Tolerance to Intolerance in the Vacancy-Ordered Double Perovskite Semiconductors Cs_2SnI_6 and Cs_2TeI_6. *J. Am. Chem. Soc.*, **2016**, 138, 8453-8464.

21 A. Natik, Y. Abid, R. Moubah, M. Abid, H. Lassri. Ab-initio investigation of the structural, electronic and optical properties of lead-free halide Cs_2TiI_6 double perovskites. *Solid State Commun.*, **2020**, 319, 114006.

22 M.E. Yadari, L. Bahmad, A.E. Kenz, A. Benyoussef. Monte Carlo study of the double perovskite nano Sr_2VMoO_6. *J. Alloys Compd.*, **2013**, 579, 86-91.

23 A. Nid-Bahami, A.E. Kenz, A. Benyoussef, L. Bahmad, M. Hamedoun, H.E. Moussaoui. *J. Magn. Magn. Mater.*, Magnetic properties of double perovskite Sr_2RuHoO_6: Monte Carlo simulation. **2016**, 417, 258-266.

24 Q. Mahmood, M. Hassan, N. Yousaf, A.A. AlObaid, T.I. Al-Muhimeed, M. Morsi, H. Albalawi, O.A. Alamri. Study of lead-free double perovskites halides Cs_2TiCl_6, and Cs_2TiBr_6 for optoelectronics, and thermoelectric applications. *Mater. Sci. Semicond. Process.*, **2021**, 137, 106180.

25 M.Z. Galin, A.K. Ivanov-Schitz, G.N. Mazo. Molecular dynamics simulation of structural and transport properties of solid solutions of double perovskites based on $PrBaCo_2O_{5.5}$. *Crystallogr. Rep.*, **2020**, 65, 289-296.

26 G. Catalan, J.F. Scott. Physics and applications of bismuth ferrite. *Adv. Mater.*, **2009**, 21, 2463.

27 J. Ma, J. Hu, Z. Li, C.W. Nan. Recent progress in multiferroic magnetoelectric composites: from bulk to thin films. *Adv. Mater.*, **2011**, 23, 1062.

28 M. Faizan, K.C. Bhamu, S.H. Khan, G. Murtaza and X. He. Computational study of defect variant perovskites A_2BX_6 for photovoltaic applications. *arXiv*, **2020**, arXiv:2002.07543v2.

29 Y. Wang, T. Zhang, F. Xu, Y. Li and Y. Zhao. A Facile Low Temperature Fabrication of High Performance $CsPbI_2Br$ All-Inorganic Perovskite Solar Cells. *Sol. RRL*, **2018**, 2, 1700180.

30 Y. Cai, W. Xie, H. Ding, Y. Chen, K. Thirumal, L.H. Wong, N. Mathews, S.G. Mhaisalkar, M. Sherburne and M. Asta. Computational Study of Halide Perovskite-Derived A_2BX_6 Inorganic Compounds: Chemical Trends in Electronic Structure and Structural Stability. *Chem. Mater.*, **2017**, 29, 7740-7749.

31 M. Hutter and T. Clark. On the enhanced stability of the guanine-cytosine base-pair radical cation. *J. Am. Chem. Soc.*, **1996**, 118, 7574-7577.

32 M. Hamdan, A.K. Chandiran. Cs_2PtI_6 Halide Perovskite is Stable to Air, Moisture, and Extreme pH: Application to Photoelectrochemical Solar Water Oxidation. *Angew. Chem.*, **2020**, 132, 16167-16172.

33 M. Sajjad, Q. Mahmood, N. Singh and J.A. Larsson. Ultralow Lattice Thermal Conductivity in Double Perovskite Cs_2PtI_6: A Promising Thermoelectric Material. *Acs Appl. Energ. Mater.*, **2020**, 11, 11293-11299.

34 M.G. Ju, M. Chen, Y. Zhou, H.F. Garces, J. Dai, L. Ma, N.P. Padture, X.C. Zeng. Earth-abundant nontoxic titanium (IV)-based vacancy-ordered double perovskite halides with tunable 1.0 to 1.8 eV bandgaps for photovoltaic applications. *ACS Energy Lett.*, **2018**, 3, 297-304.

35 Q. Mahmood, M. Hassan, T.H. Flemban, B.U. Haq, S.A. Faify, N.A. Kattan, A. Laref. Optoelectronic and thermoelectric properties of double perovskite Rb_2PtX_6 (X= Cl, Br) for energy harvesting: first-principles investigations. *J. Phys. Chem. Solids*, **2021**, 148, 109665.

36 G. Kresse and J. Furthmuller. Efficiency of ab-initio total energy calculations for metals and semiconductors using a plane-wave basis set. *Comput. Mater. Sci.*, **1996**, 6, 15–50.

37 J.P. Perdew, K. Burke and M. Ernzerhof. Generalized gradient approximation made simple. *Phys. Rev. Lett.*, **1996**, 77, 3865-3868.

38 J. Heyd, G.E. Scuseria and M. Ernzerhof. Hybrid functionals based on a screened Coulomb potential. *J. Chem. Phys.*, **2003**, 118, 8207-8215.

39 P.E. Blöchl. Projector augmented-wave method. *Phys. Rev. B*, **1994**, 50, 17953-17979.

40 G. Engel and Z. Kristallogr. The crystal structures of several hexachlorous complex salts. *Cryst. Mater.*, **1935**, 90, 341-373.

41 A. Ferrari and L. Coghi. On the existence of hexahalogenoaurates. *Gazz. Chim. Ital.*, **1941**, 71, 440.

42 G. Thiele, C. Mrozek, D. Kämmerer and K. Wittmann. Über Hexaiodoplatinate(IV) M_2PtI_6 (M = K, Rb, Cs, NH_4, Tl) Darstellungsverfahren, Eigenschaften und Kristallstrukturen / On Hexaiodoplatinates(IV) M_2PtI_6 (M = K, Rb, Cs, NH_4, Tl) - Preparation, Properties and Structural Data. *Zeitschrift für Naturforschung B*, **1983**, 38, 905-910.

43 V.M. Goldschmidt. Die gesetze der krystallochemie. *Naturwissenschaften*, **1926**, 14, 477-485.

44 J. Gebhardt and A.M. Rappe. Mix and match: organic and inorganic ions in the perovskite lattice. *Adv. Mater.*, **2019**, 31, 1802697.

45 H. Tanaka, T. Oku and N. Ueoka. Structural stabilities of organic–inorganic perovskite crystals. *Jpn. J. Appl. Phys.*, **2018**, 57, 08RE12.

46 L. Schimka, R. Gaudoin, J. Klimes, M. Marsman and G. Kresse. Lattice constants and cohesive energies of alkali, alkaline-earth, and transition metals: Random phase approximation and density functional theory results. *Phys. Rev. B: Condens. Matter Mater. Phys.*, **2013**, 87, 214102.

47 N.P. Blake, D. Bryan, S. Latturner, L. Møllnitz, G.D. Stucky and H. Metiu. Structure and stability of the clathrates $Ba_8Ga_{16}Ge_{30}$, $Sr_8Ga_{16}Ge_{30}$, $Ba_8Ga_{16}Si_{30}$, and $Ba_8In_{16}Sn_{30}$. *J. Chem. Phys.,* **2001**, 114, 10063-10074.

48 S. Zhu, M. Jiang, J. Ye, H. Xie and Y. Qiu. Optical properties of photovoltaic materials: Organic-inorganic mixed halide perovskites $CH_3NH_3Pb(I_{1-y}X_y)_3$(X= Cl, Br). *Comput. Theor. Chem.*, **2018**, 1144, 1-8.

49 M. Hussain, M. Rashid, A. Ali, F. Bhopal, A.S. Bhatti. Systematic study of optoelectronic and transport properties of cesium lead halide (Cs_2PbX_6; X= Cl, Br, I) double perovskites for solar cell applications. *Ceram. Int*., **2020**, 46, 21378-21387.

50 S. Idrissi, S. Ziti, H. Labrim, L. Bahmad. Band gaps of the solar perovskites photovoltaic $CsXCl_3$ (X= Sn, Pb or Ge). *Mater. Sci. Semicond. Process.*, **2021**, 122, 105484.

Chapter 4. Computational screening of Cs based vacancy-ordered double perovskites for solar cell and photocatalysis applications

4.1 Introduction

Halide perovskites have been expected to be the next generation of important materials for various optoelectronic applications due to their low-cost, excellent absorption coefficient, suitable bandgap, and facile fabrication process.[1–4] The perovskite solar cells, in particular, have achieved remarkable power conversion efficiency (PCE) over a short research time. Since the debut of $MAPbI_3$ and $MAPbBr_3$ as photovoltaic materials,[5] the PCEs were steadily improved and reach 25.5% nowadays.[6] Furthermore, this type of perovskite with exceptional charge transfer ability has also witnessed a vigorous development in photocatalysis over the traditional oxide perovskites in the past few years.[7–9] Their potential applications in the organic pollutants degradation, the decomposition of H_2O to H_2 and O_2, and CO_2 reduction by solar energy have triggered ripples of excitement.[10] Halide perovskites possess a crystal structure of general formula ABX_3, similar to that of typical perovskites with general formula ABO_3. In the halide perovskite crystal structure, the larger metal ion (e.g. Cs^+) or monovalent organic cation (e.g. MA^+) is located at the A-site, and the B-site is smaller metal ion (Ge^{2+}, Sn^{2+}, Pb^{2+}, etc) as well as X is halide ion. Although many researchers have witnessed the phenomenal growth of halide perovskite, both inorganic and hybrid, there are still challenges to the booming field of solar cells and photocatalysis, i.e., the instability and lead toxicity that some perovskites suffer from.[11] The toxicity of lead ions in halide perovskite absorbing materials is the main bottleneck for practical application. Lead is one of the three major heavy metal contaminants and a heavy metal element that seriously endangers humans and the environment.[12] Even if only a small amount of exposure, lead can seriously threaten health, causing problems including impaired brain development, renal failure, and nerve injury.[13] Therefore, it also hinders the lead halide perovskite large-scale production and commercial application. To overcome these limitations, researchers are focusing on replacing Pb with non-toxic metals. However, studies have shown that the oxidation tendency of same group elements like Sn and Ge changes from + 2 states to + 4 states, which is

incompatible with totally replacing Pb.[14,15] The perovskites composed of other divalent cations instead of lead may have poor photoelectric properties due to a large bandgap.[16,17] Hence, attempts have been made to explore perovskite-like structures through double perovskites, in which monovalent and trivalent ones transmute two adjacent divalent lead ions.[18] So far, according to the different types of B and B' cations, researchers have synthesized four sorts of double perovskites with general formulas $A_2BB'X$. A-side from the general formula A_2BX_6, represented by a vacancy in the B cation and a tetravalent B' cation, the other three types all take the scheme of Pb^{2+} replacing monovalent and trivalent ions.[7] This kind of new perovskite provides researchers with a new idea to prepare green materials without losing photoelectric properties and shows excellent stability in light, moisture, and temperature.[19,20] Due to the existence of unstable organic cations, the thermal decomposition temperature of hybrid perovskite is low. For the solution of thermal instability, some scholars prefer to replace the organic components in perovskite with inorganic metal ions, such as Cs^+.[21–23] A new sort of all inorganic Cs based halogenated perovskite has been developed by using oxygen evolution in water recently.[24–26] This effectively improves the thermal stability of the material, thereby prolongs the service life of the equipments.[27] In addition, the introduction of Cs can suppress the phase impurities, permitting the preparation with high purity and defect-free perovskite films, which is less sensitive to processing conditions. This enables perovskite solar cells device performance to achieve repeatable high efficiency.[28] Recent studies on lead-free perovskite substitutes, especially A_2BX_6, usually report the synthesis and characterization of bulk powders or single crystals, such as Cs_2ZrCl_6, Cs_2SnI_6, Cs_2TiBr_6, and so on.[29–31] All these investigations show that A_2BX_6 structure can be readily doped with different impurity ions, especially at the position of 6-fold coordinated tetravalent cations. Substitution alloying is expected to realize the lead-free perovskite and optimize the properties for device applications.[32] Furthermore, in some studies comparing hole transport characteristics of Cs_2SnX_6 and Cs_2TiX_6 (X = Cl, Br, I), systematic variations in the transport and optical properties were observed the halogen anions substitution with different sizes and electronegativity.[33,34] Zeng et al. also reported a novel sort of all inorganic perovskites $Cs_2TiI_xBr_{6-x}$ based on earth-rich, lead-free, and ultrastable Ti (IV). They have proved that titanium-based photonic crystals have desirable attributes.[35] Although this is only a small experimental sample of A_2BX_6 family material, which

have distinctly shown the significance of B-X composition is worthy of future exploration in the field of photocatalysis as well as solar cells.

To guide future research into the theoretical calculation of the properties of more extensive double perovskite, this study used a calculation method based on density functional theory (DFT) to investigate the structural, electronic, and optical properties of Cs_2BX_6 compounds, with the goal of finding suitable candidates for photocatalysts and perovskite solar cells. For this purpose, the study began with 30 perovskite materials including cesium ions, 10 metals, and 3 halogens, as shown in Fig.1. The A_2BX_6 double perovskite can be thought of as a derivative structure of standard $A_2B'BX_6$ perovskites, in which the vacancy substitutes the B-site cation, yielding vacancy-ordered double perovskites. The studied crystal model is shown in Fig. 1; the Cs_2BX_6 usually has a face-centered cubic structure with space group Fm3m (No.225), which is alternately formed by isolated [BX_6] clusters and twisted tetragonal Cs cations (space group P4/mnc). In the DFT framework, the most advanced hierarchical calculation method based on the first-principles is used for high-throughput screening. After using the tolerance factor and enthalpy of formation (ΔH) to evaluate the stability (or formability) of the perovskites geometric structure, the bandgaps of the optimized perovskites are calculated at the PBE (Perdew-Burke-Ernzerhof), and HSE (Heyd-Scuseria-Ernzerhof) levels with spin-orbit coupling (SOC) of theory. We employed a single procedure to prescreen the materials with potential in solar cells and photocatalysis, and set the bandgap threshold at 1.6 eV. These selected perovskites were further explored for their optical properties and band-edged positions. This study lays a solid theoretical foundation for understanding these compounds' structural and electronic properties. The experimental data of other studies prove the reliability of our calculation results. Furthermore, the results predicted by theoretical calculation can provide efficient guidance for the experimental plan, so as to improve the work efficiency and making the research more purposeful.

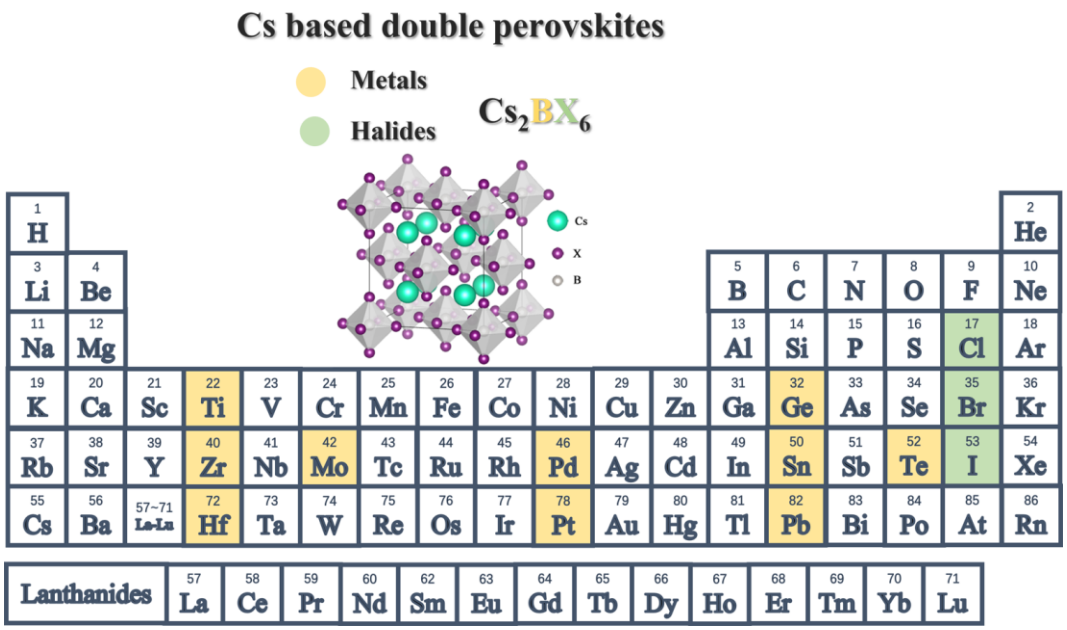

Figure. 1. The cubic phases of hybrid double perovskites of the form Cs_2BX_6 were studied using 10 different metals (B, yellow) and 3 different halides (X, green).

4.2 Calculation methods

All calculations on the compounds were performed using PBE-GGA (generalized gradient approximation) and HSE with SOC based DFT study by the Vienna Ab initio simulation package (VASP) code with a plane-wave basis set.[36–38] GGA is an approximation of functionals for exchange and correlation in DFT calculation, which contains more physical information, such as charge density and gradient information of charge density, which can generally make the calculation result more accurate[37]. The projector augmented waves (PAW) approach was used to characterize the atomic pseudopotential.[39] The energy cutoff for the plane-wave basis for all compounds was set to 400 eV. The k-points grid of 4×4×4 was employed for computing integrals over the Brillouin zone for geometric optimizations and analysis of the density of states (DOS). According to the convergence testing results of three randomly picked compounds Cs_2TiCl_6, Cs_2PdBr_6, and Cs_2TeI_6 in Fig. 2, it is found that the selections of plane-wave cutoff, k-point density, and the energy convergence criterion are sufficient to provide the total energy converging to within 0.001 eV/atom, lattice constants within 0.1 Å, and band gaps within 0.01 eV. In this work, the optimized perovskites' optical properties and electronic properties were first calculated by PBE functional, a less expensive function in terms of computational time without enough accuracy for

calculating the bandgaps of solids. After prescreening, HSE functional with SOC was used to perform the high-precision calculation for remaining perovskites. After prescreening, HSE functional with SOC was used to perform the high-precision calculation for remaining perovskites. All the structures considered in this study were fully relaxed using the conjugate gradient algorithm until the force converge on individual ions were less than 0.001 eV/Å at the PBE level, and within 0.05 eV/Å for HSE+SOC. Fig. 3 show the variation of the DFT bandgap of perovskites with two distinct functional and with or without SOC. In halide perovskite systems containing heavy elements, the SOC effect must be seriously considered, and SOC can significantly reduce the calculated bandgap for cesium-based halide perovskites. [40–42]

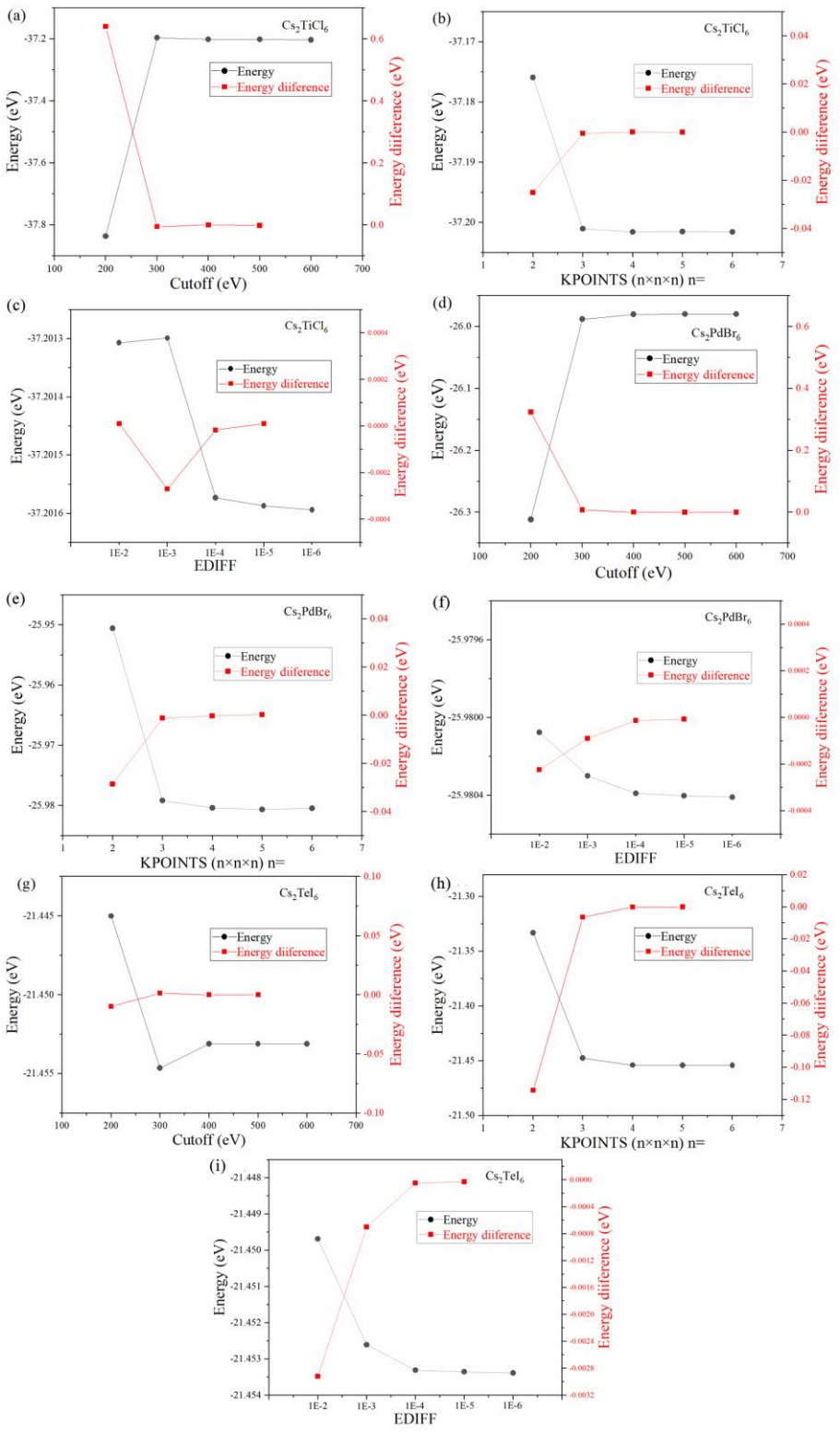

Figure. 2. Convergence testing of Cs_2TiCl_6(a: Cutoff, b: K-points, c: EDIFF), Cs_2PdBr_6(d: Cutoff, e: K-points, f: EDIFF) and Cs_2TeI_6(g: Cutoff, h: K-points, i: EDIFF).

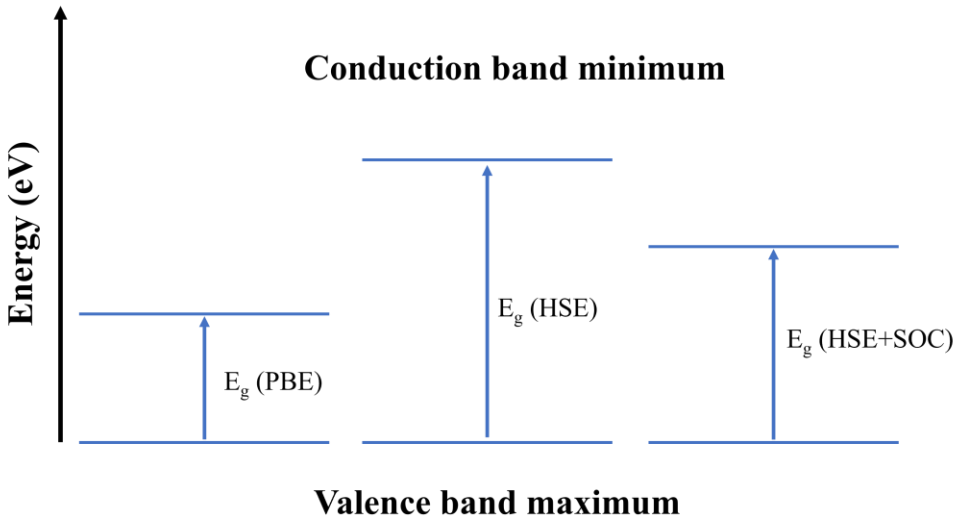

Figure. 3. Diagram of difference in the DFT bandgaps with the 2 functionals (PBE and HSE) without and with SOC.

4.3 Results and discussions

4.3.1 Structural and thermodynamic stability

Perovskites' structural and thermodynamic stability are important area of research for practical applications. Due to weakly bonded soft organic cations, inorganic halide perovskite is more stable than hybrid perovskite.[43] However, as inorganic cations and halogen ions vary, the stability of inorganic halide perovskite changes as well. In screening perovskites, the perovskite structure structural stability (or formability) under various chemical compositions is usually the preliminary evaluation for the studied materials. The structures of 30 perovskite materials were optimized at the PBE functional level using DFT, and their enthalpy of formation (ΔH), Gibbs free energy (ΔG), and entropy (ΔS) were calculated. Note that the ΔH is enough to determine the perovskite stability at 0 K, but it could be different from that at room temperature.[44] Therefore, we also calculated the reaction free energy at room temperature (298.15 K), and considered the zero-point energy (ΔE_{ZPE}) correction. The optimized lattice parameters, ΔH, ΔG, ΔS, Goldschmidt tolerance factor (t), octahedral factor (μ), and new tolerance factor (τ) of Cs_2BX_6 symmetrical cubic cell, are included in Table 1.

Table 1 Optimized lattice parameters, enthalpy of formation (ΔH), Gibbs free energy (ΔG), entropy (ΔS), Goldschmidt tolerance factor (t), octahedral factor (μ), and new tolerance factor (τ)

of Cs_2BX_6 symmetrical cell.

Compound	*a* (Å)	ΔH(eV/$f.u.$)	ΔG(eV/$f.u.$)	ΔS(meV/K)	t	μ	τ
Cs_2TiCl_6	10.34	-16.37	-17.11	3.21	0.977	0.475	3.900
Cs_2TiBr_6	10.84	-13.63	-14.63	3.86	0.963	0.439	4.074
Cs_2TiI_6	11.83	-10.04	-11.20	4.27	0.943	0.391	4.353
Cs_2ZrCl_6	10.54	-19.21	-20.03	3.44	1.031	0.398	4.234
Cs_2ZrBr_6	11.02	-15.10	-16.14	3.97	1.013	0.367	4.443
Cs_2ZrI_6	11.95	-11.34	-12.53	4.31	0.988	0.327	4.776
Cs_2GeCl_6	10.57	-12.45	-13.21	3.28	1.027	0.403	4.202
Cs_2GeBr_6	11.07	-10.03	-11.04	3.87	1.009	0.372	4.407
Cs_2GeI_6	11.76	-6.92	-8.12	4.35	0.985	0.332	4.736
Cs_2HfCl_6	10.48	-18.12	-18.94	3.43	1.035	0.392	4.341
Cs_2HfBr_6	11.00	-15.16	-16.21	3.98	1.017	0.362	4.480
Cs_2HfI_6	11.95	-11.27	-12.47	4.35	0.991	0.323	4.818
Cs_2PdCl_6	10.31	-10.73	-11.43	3.12	0.977	0.475	3.900
Cs_2PdBr_6	10.93	-9.19	-10.19	3.85	0.963	0.439	4.074
Cs_2PdI_6	11.64	-7.14	-8.3	4.27	0.943	0.391	4.353
Cs_2TeCl_6	10.61	-11.75	-12.64	3.60	0.939	0.536	3.795
Cs_2TeBr_6	11.13	-9.89	-11.00	4.14	0.927	0.495	3.950
Cs_2TeI_6	12.06	-7.37	-8.61	4.47	0.910	0.441	4.197
Cs_2MoCl_6	10.32	-12.52	-13.24	3.18	1.060	0.359	4.508
Cs_2MoBr_6	10.84	-10.02	-11.01	3.83	1.040	0.332	4.739
Cs_2MoI_6	11.60	-6.83	-5.42	4.21	1.012	0.295	5.108
Cs_2SnCl_6	10.48	-13.38	-14.19	3.38	0.881	0.635	3.900
Cs_2SnBr_6	11.14	-11.14	-12.20	3.99	0.873	0.587	4.030
Cs_2SnI_6	12.01	-8.05	-9.27	4.40	0.861	0.523	4.239
Cs_2PtCl_6	10.19	-11.25	-11.93	3.08	1.000	0.442	4.013
Cs_2PtBr_6	10.67	-10.11	-11.10	3.83	0.984	0.408	4.200
Cs_2PtI_6	11.37	-7.44	-8.59	4.21	0.962	0.364	4.500
Cs_2PbCl_6	11.58	-11.75	-12.64	3.58	0.870	0.657	3.976
Cs_2PbBr_6	11.11	-9.90	-11.04	4.18	0.862	0.607	4.102

Cs_2PbI_6	11.99	-7.26	-8.58	4.68	0.851	0.541	4.303

The optimized primitive cells of all compounds were shown in Fig. 4-13. Taking the Cs_2PtX_6 optimized primitive cell as an example (Fig. 4), the lattice constant of Cs_2PtI_6, Cs_2PtBr_6, and Cs_2PtCl_6 is 11.67 Å, 11.04 Å, and 10.35 Å, respectively. These results are close to the experimental values (Cs_2PtI_6: 11.37 Å, Cs_2PtBr_6: 10.67 Å, Cs_2PtCl_6: 10.19 Å),[45–47] suggesting that the construction of the model and the selection of calculation parameters are reasonable.

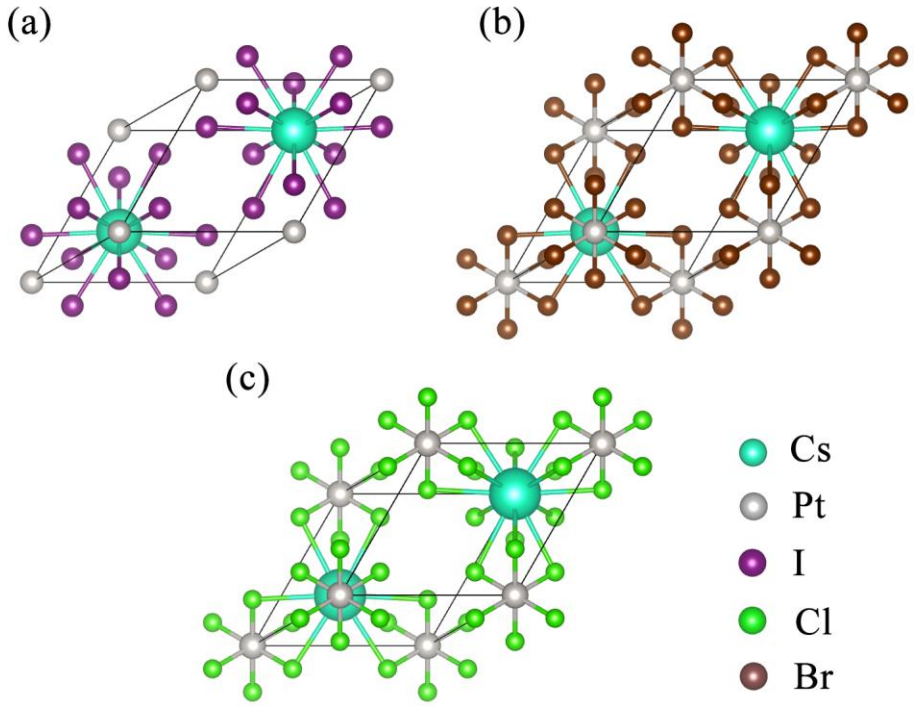

Figure. 4. Primitive cell structure of (a) Cs_2PtI_6, (b) Cs_2PtBr_6 and (c) Cs_2PtCl_6.

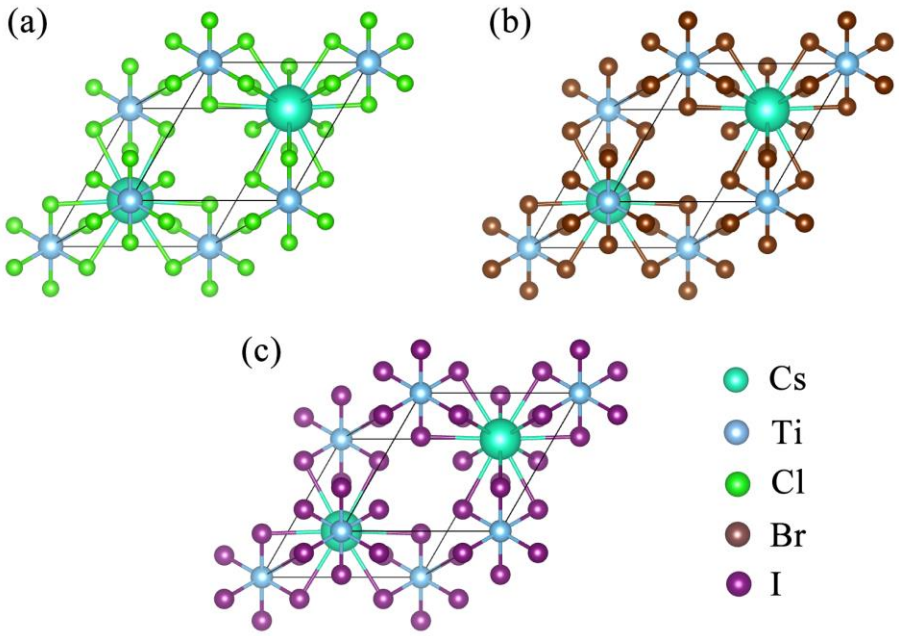

Figure. 5. Primitive cell structure of (a) Cs_2TiCl_6, (b) Cs_2TiBr_6 and (c) Cs_2TiI_6.

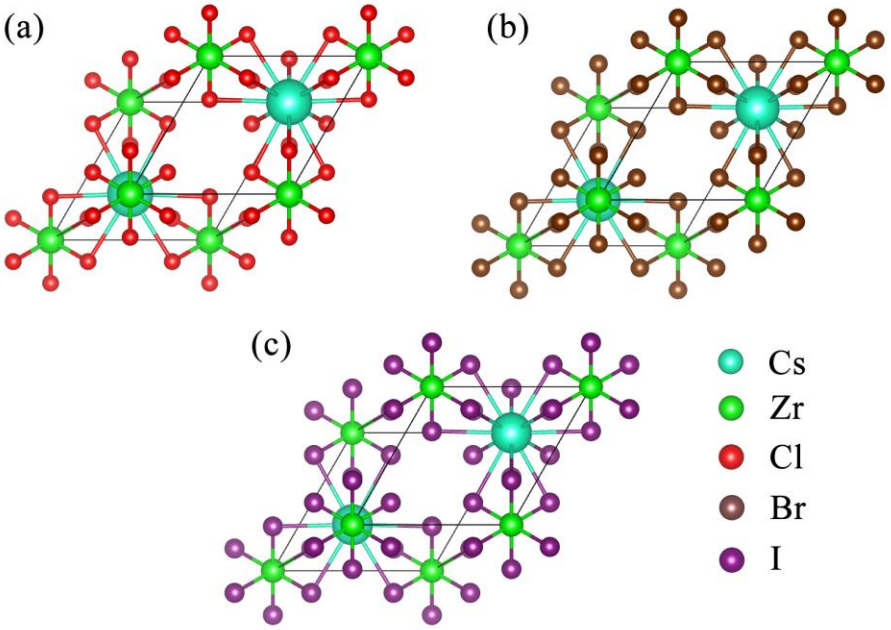

Figure. 6. Primitive cell structure of (a) Cs_2ZrCl_6, (b) Cs_2ZrBr_6 and (c) Cs_2ZrI_6.

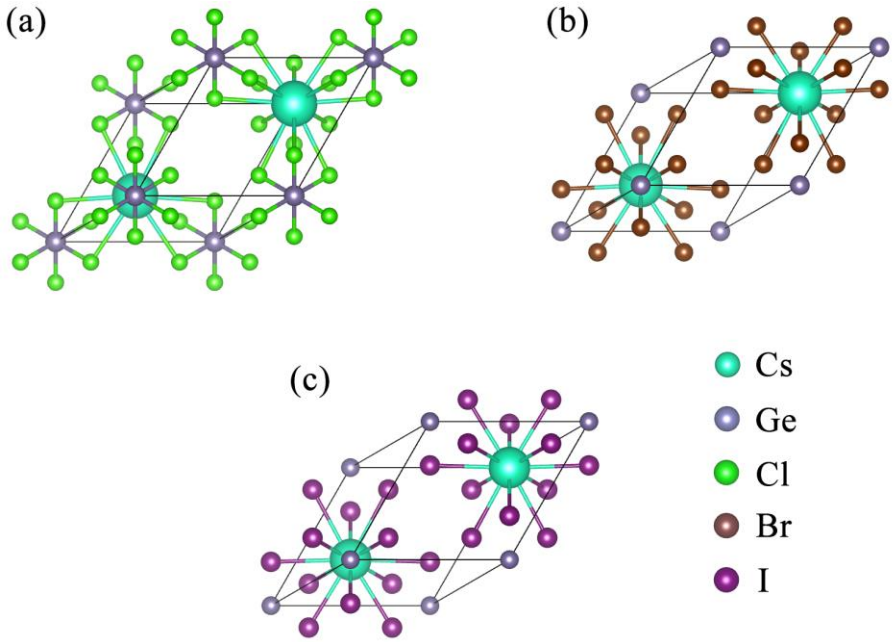

Figure. 7. Primitive cell structure of (a) Cs_2GeCl_6, (b) Cs_2GeBr_6 and (c) Cs_2GeI_6.

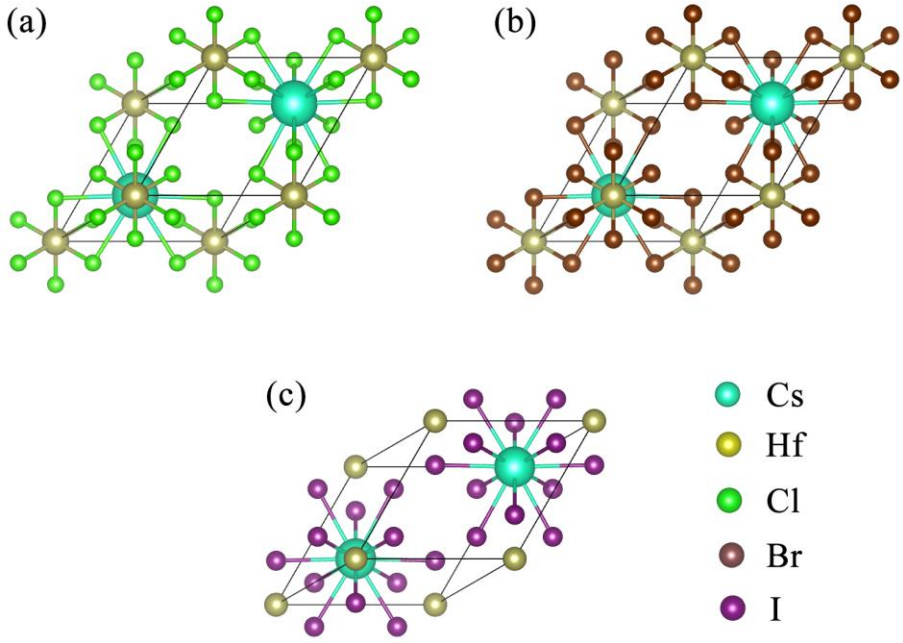

Figure. 8. Primitive cell structure of (a) Cs_2HfCl_6, (b) Cs_2HfBr_6 and (c) Cs_2HfI_6.

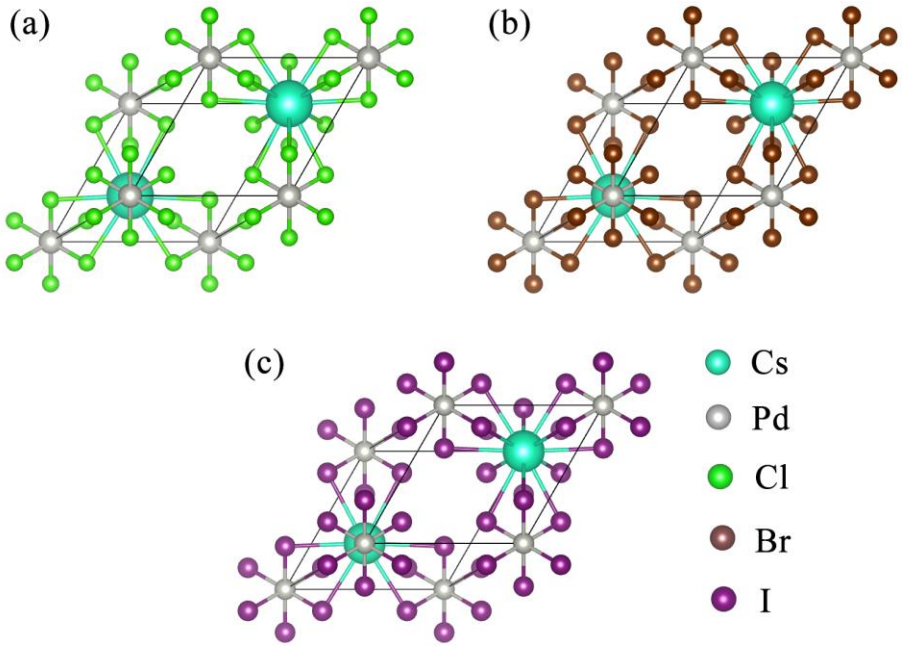

Figure. 9. Primitive cell structure of (a) Cs_2PdCl_6, (b) Cs_2PdBr_6 and (c) Cs_2PdI_6.

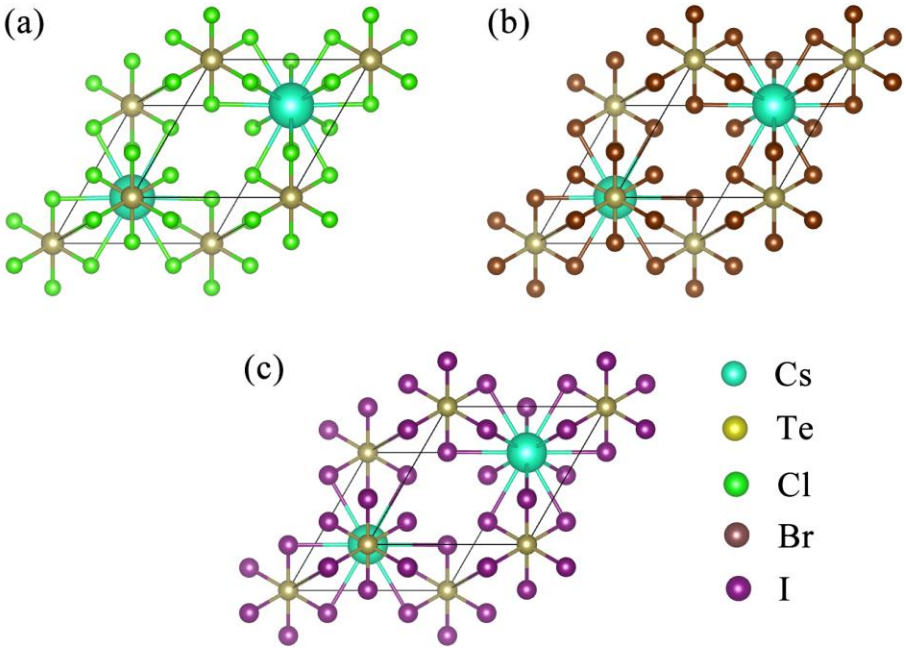

Figure. 10. Primitive cell structure of (a) Cs_2TeCl_6, (b) Cs_2TeBr_6 and (c) Cs_2TeI_6.

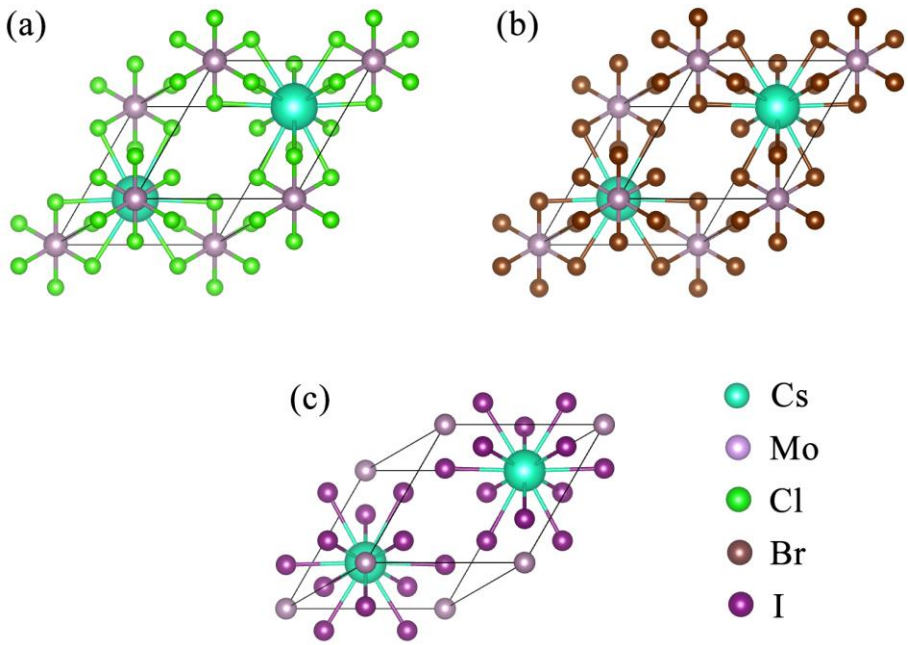

Figure. 11. Primitive cell structure of (a) Cs_2MoCl_6, (b) Cs_2MoBr_6 and (c) Cs_2MoI_6.

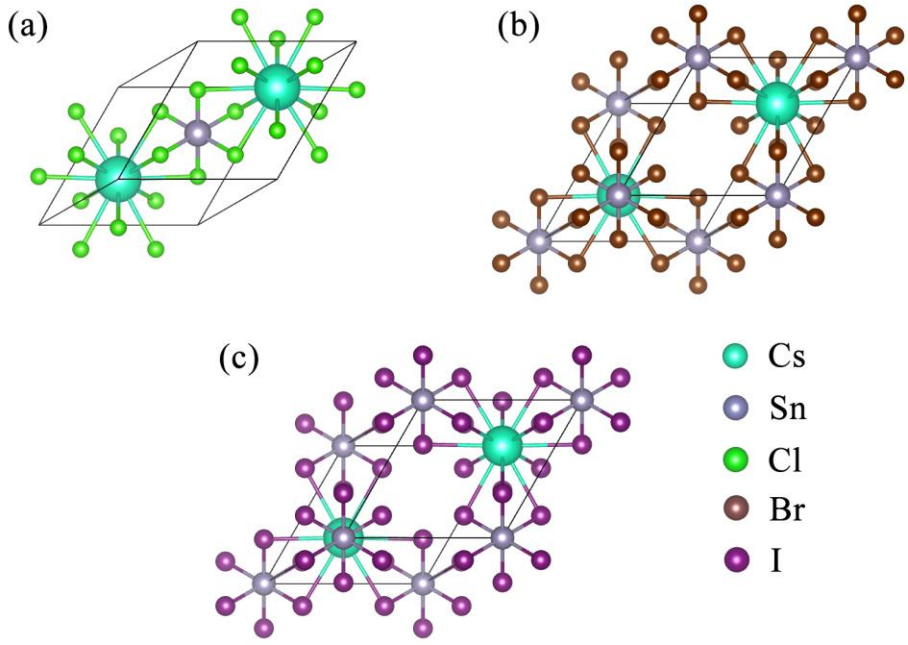

Figure. 12. Primitive cell structure of (a) Cs_2SnCl_6, (b) Cs_2SnBr_6 and (c) Cs_2SnI_6.

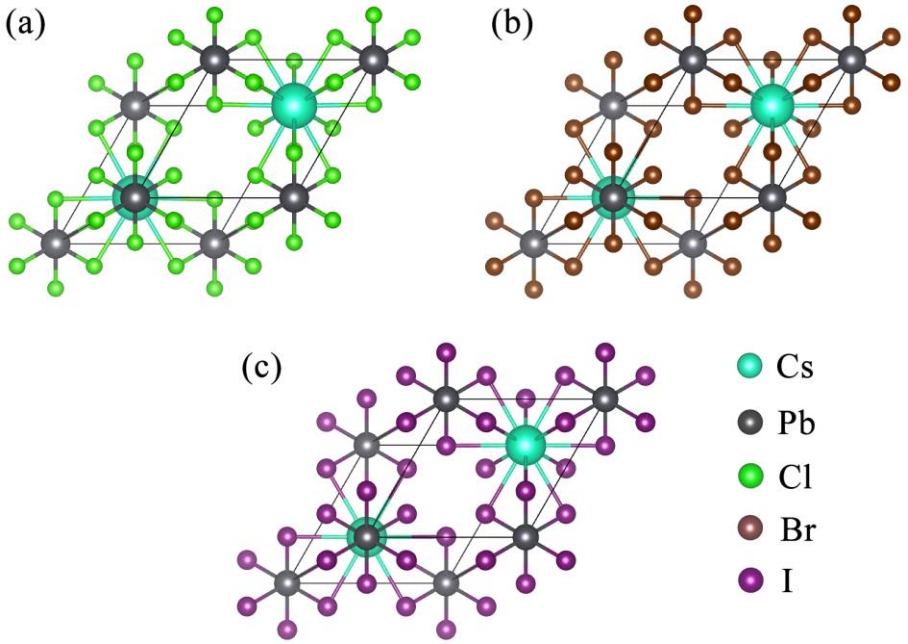

Figure. 13. Primitive cell structure of (a) Cs_2PbCl_6, (b) Cs_2PbBr_6 and (c) Cs_2PbI_6.

The ΔH can be defined as the difference between the total energy of the compound and the energies of each component in the standard state, and the formula is as follows:

$$\Delta H = E_{\text{bulk}} - n_{Cs}E_{\text{atom}}^{\text{Cs}} - n_B E_{\text{atom}}^{\text{B}} - n_X E_{\text{atom}}^{\text{X}} \quad (1)$$

where E_{bulk} represents the total energy of Cs_2BX_6; E_{atom} is the energy of the free atoms B and X, and n represents the number of free atoms in the primitive cell. The reaction free energies can be obtained by the following equation

$$\Delta G = \Delta H + \Delta E_{ZPE} - T\Delta S \quad (2)$$

where the ΔS and ΔE_{ZPE} are the difference of entropy and zero-point energy, respectively. The negative ΔH and ΔG indicate the excellent stability of all compounds, which will not decompose into respective binary components. Moreover, the reliability of the thermodynamic stability evaluation was further verified by calculating perovskite materials (Cs_2TiI_6, Cs_2GeBr_6, Cs_2PtI_6, Cs_2PdBr_6, Cs_2TeI_6, Cs_2TiBr_6, Cs_2SnBr_6, and Cs_2PtBr_6) suitable for solar cells or photocatalysts in solar water splitting after final screening by the commonly used convex hull method.[48] The enthalpies of formation of the potential binary and ternary competitive phases of Cs_2BX_6 are illustrated in Fig. 14, and all compounds correspond on the x-axis. The dashed line represents the convex hull, that is, the set of enthalpies change lines of all competing phases. If the ΔH of the perovskite studied is less than the convex hull of all phases, which means that the compound is

thermodynamically stable, otherwise, the material may be metastable or prone to decomposition.[49] From the convex hull approach of the various competing phases of Cs_2TiI_6, Cs_2GeBr_6, Cs_2PtI_6, Cs_2PdBr_6, Cs_2TeI_6, Cs_2TiBr_6, Cs_2SnBr_6, and Cs_2PtBr_6, it can be seen all the screened perovskites are thermodynamically stable.

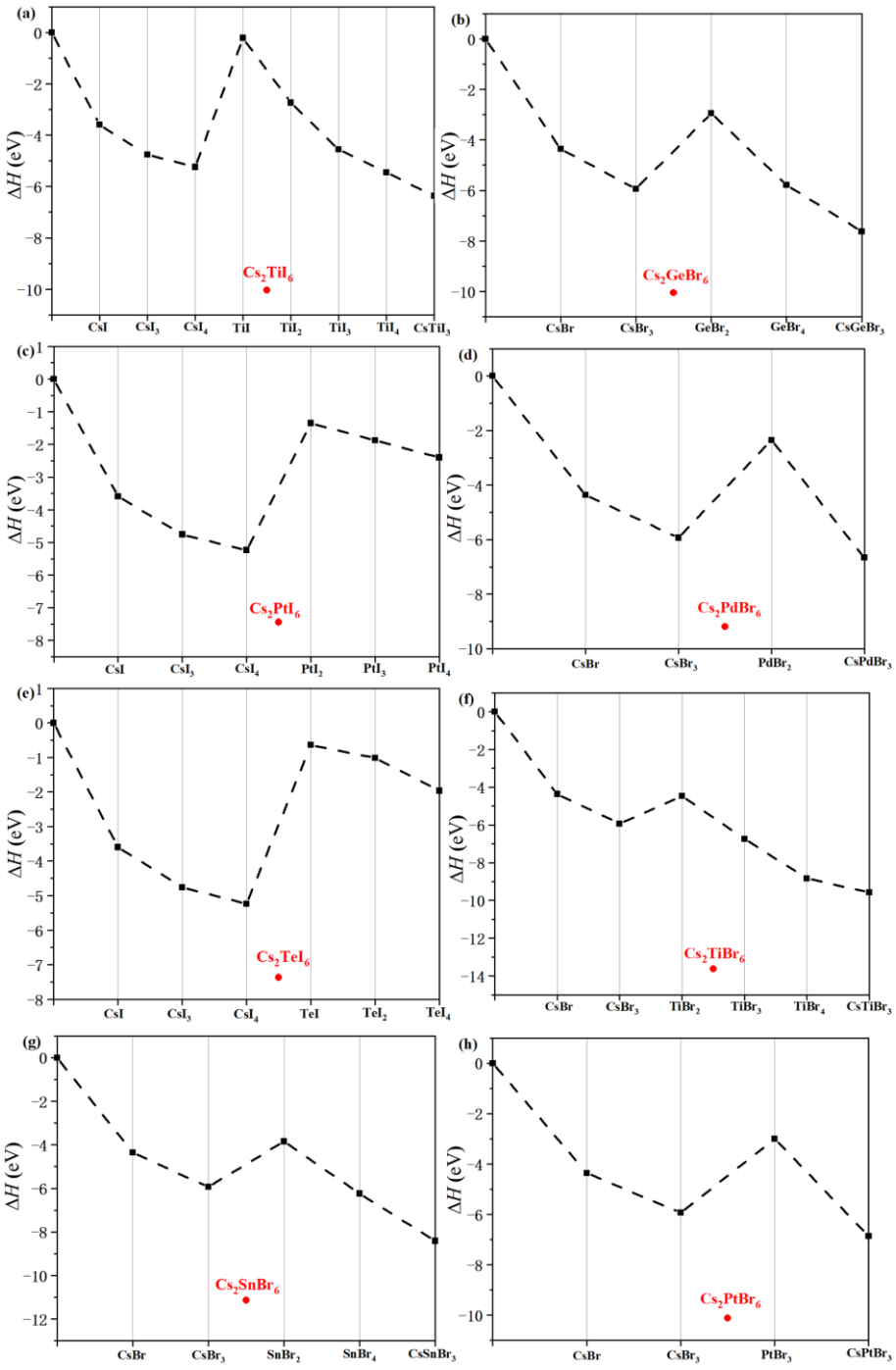

Figure. 14. The enthalpy of formation of the potential binary and ternary competitive phase of (a) Cs_2TiI_6, (b) Cs_2GeBr_6, (c) Cs_2PtI_6, (d) Cs_2PdBr_6, (e) Cs_2TeI_6, (f) Cs_2TiBr_6, (g) Cs_2SnBr_6, and (h) Cs_2PtBr_6. The dashed line represents the convex hull, that is, the set of enthalpy change lines of all competing phases.

The Goldschmidt tolerance factor ($t = (r_A+r_X)/\sqrt{2}(r_B+r_X)$) and the octahedral factor ($\mu = r_B/r_X$) are commonly used to predict the formation of perovskites by ion radius (r) to get a more distinct idea about the stability of these perovskites at room temperature.[50,51] Generally, the cubic structure of halide perovskites can maintain stability at $0.89 < t < 1$ and $0.44 < \mu < 0.90$.[52] Table 1 shows that the τ of all compounds meet the constraint conditions, representing that perovskites are relatively stable in the cubic phase at room temperature. However, the calculation results of μ are not all in a stable range, which is related to the perovskite structural characteristics. The symmetry-lowering phase transition causes the cooperative octahedral tilt and rotation of the vacancy-ordered structure with the general formula A_2BX_6 after cooling. The constituent atoms' ionic radius mismatch, affects this phase transition.[53] By comparing structural maps separated by halide, Fedorovskiy et al. also conclude that the μ factor may not be closely related to the formation of cubic double perovskite.[54] Significantly, for more than 90 years, perovskite design has been based on the Goldschmidt tolerance factor. However, as reported by recent studies, its accuracy is often not enough. In 2019, Bartel et al. initiated a new tolerance factor with a total accuracy of 92%, which was used to test the experimental group and generalized in a wide range of single and double perovskites.[55]

$$\tau = \frac{r_X}{r_B} - n_A\left(n_A - \frac{r_A/r_B}{\ln(r_A/r_B)}\right) \quad (3)$$

in which n_A represents the oxidation state of A-site cation, r_A and r_B represent the radius of ions, $r_A > r_B$ by definition, and $\tau < 4.18$ indicates perovskite. τ is only trained for ABX_3 compounds, but it is easy to adapt to $A_2BB'X_6$ double perovskite since it relies only on compositions rather than structures. It can be concluded from Table 1, that when Zr, Ge, Hf, and Mo are selected for B-site cations, no matter what the halogen ion is, the value of τ will be greater than 4.18, meaning that the probability of this component forming a stable perovskite structure is low. Cl^- contributes more to structural stability than Br^- and I^-, which is consistent with the calculation results of ΔH and ΔG. Note that since the τ was not verified on vacancy-ordered double perovskite A_2BX_6, its

accuracy could be in doubt. Cs_2PtI_6, for instance, has been successfully synthesized and investigated effectively, and it is not capable of forming stable perovskite as predicted by the τ.[11,56]

4.3.2 Electronic properties

One of the important characteristics of these perovskite materials is the bandgap. The optimum bandgap of single-junction perovskite solar cells is usually within the range of 0.9–1.6 eV.[35,57] The bandgaps of these 30 perovskites were calculated using DFT at the PBE levels, and the results were employed as a pre-screening benchmark. The PBE-based band structure and DOS of the studied 30 perovskites were displayed in Fig. 15–19. However, PBE functional underestimates the bandgaps of periodic systems in most cases. To account for numerical inaccuracies, we maintain a margin of 0.3 eV at the low ends, i.e., the perovskites with bandgap values of 0.6–1.6 eV at the PBE level were selected for further study.

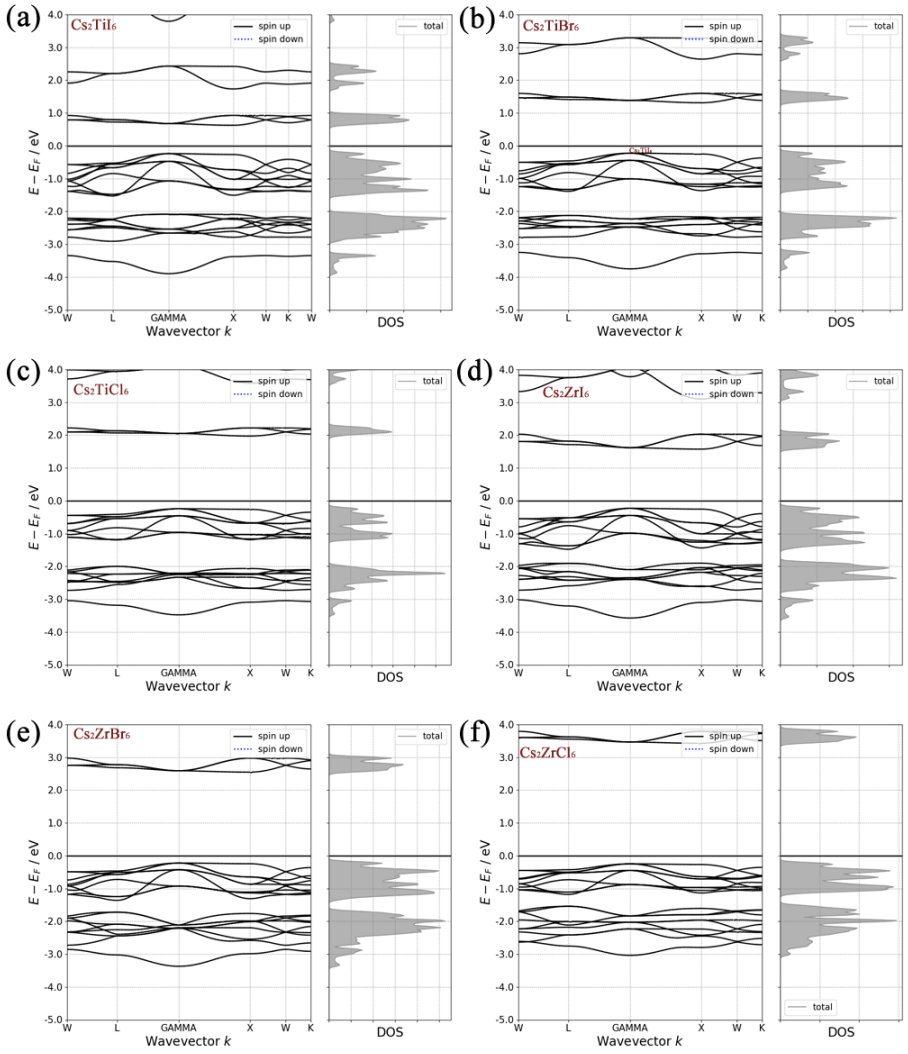

Figure. 15. Band structures and density of states of the (a) Cs_2TiI_6, (b) Cs_2TiBr_6, (c) Cs_2TiCl_6, (d) Cs_2ZrI_6, (e) Cs_2ZrBr_6, (f) Cs_2ZrCl_6 calculated by PBE functional.

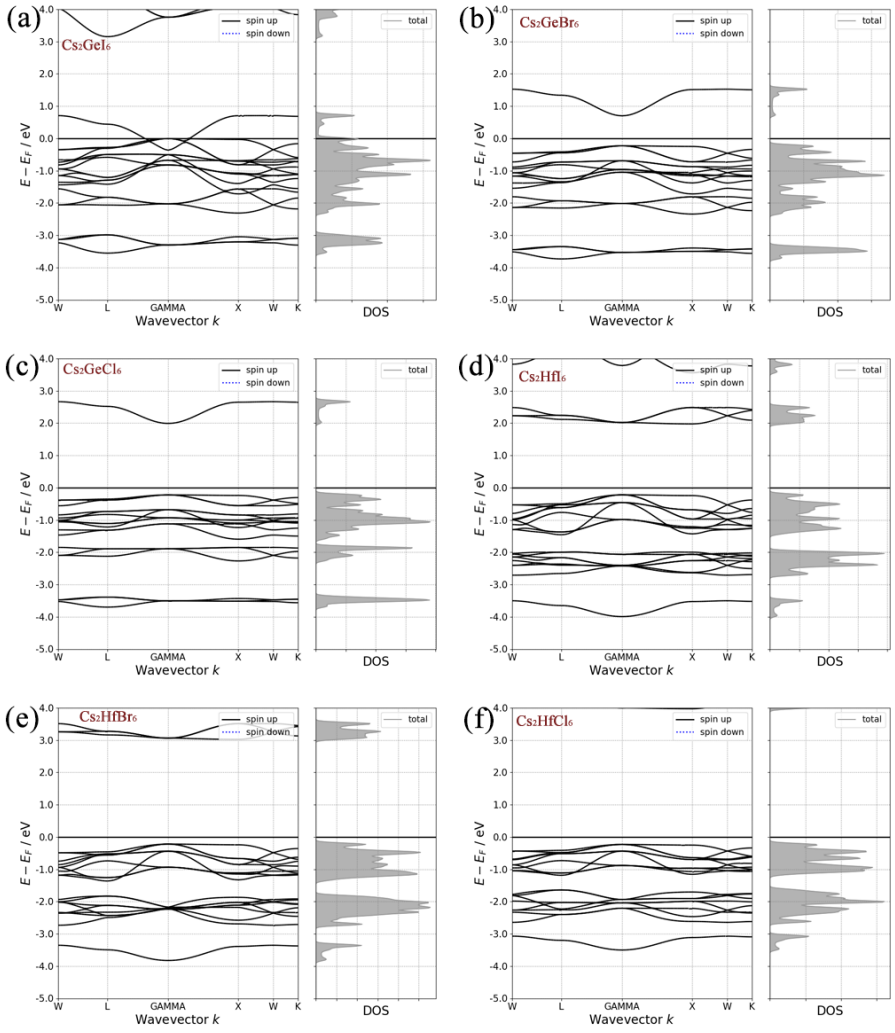

Figure. 16. Band structures and density of states of the (a) Cs_2GeI_6, (b) Cs_2GeBr_6, (c) Cs_2GeCl_6, (d) Cs_2HfI_6, (e) Cs_2HfBr_6, (f) Cs_2HfCl_6 calculated by PBE functional.

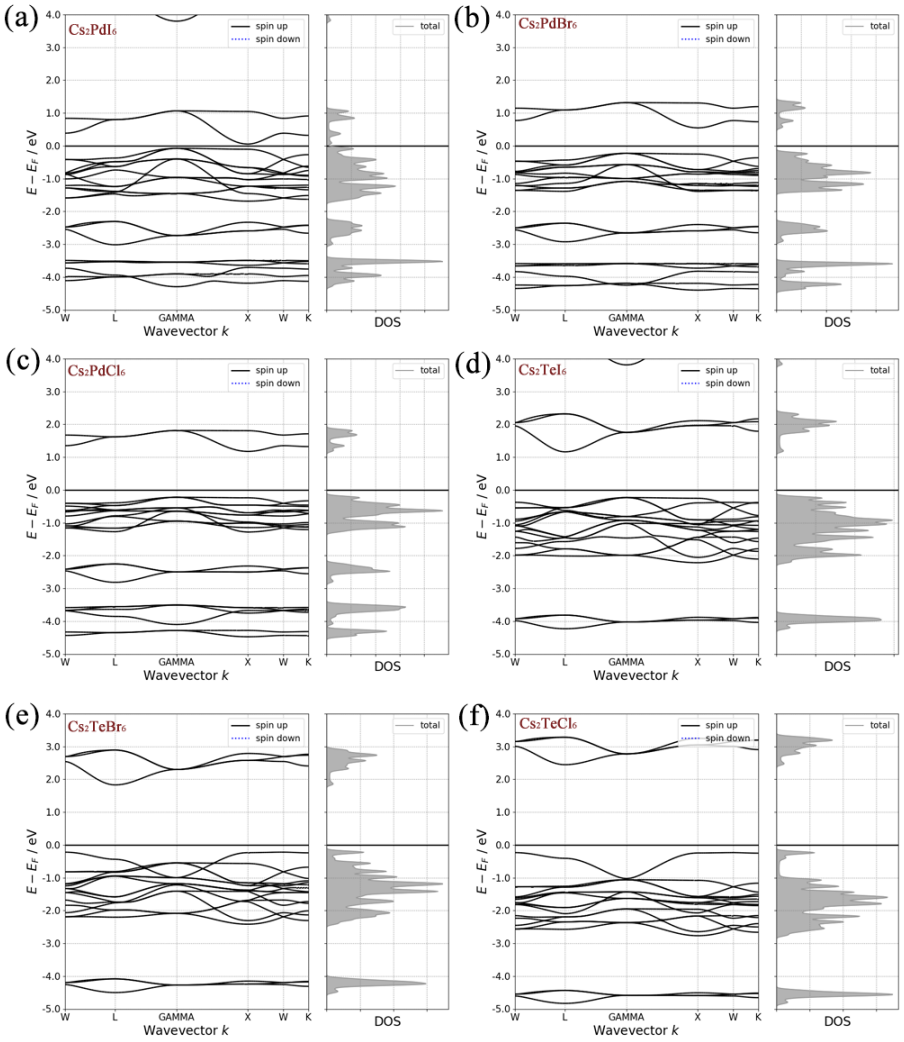

Figure. 17. Band structures and density of states of the (a) Cs_2PdI_6, (b) Cs_2PdBr_6, (c) Cs_2PdCl_6, (d) Cs_2TeI_6, (e) Cs_2TeBr_6, (f) Cs_2TeCl_6 calculated by PBE functional.

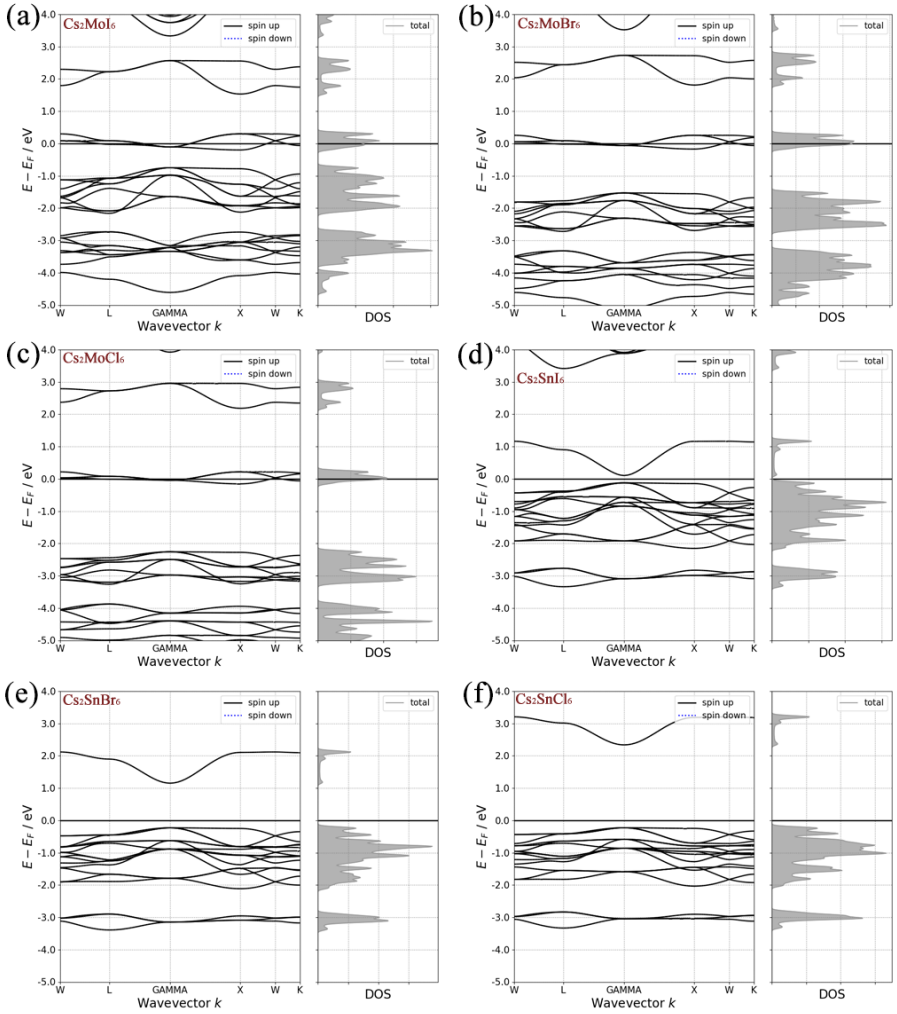

Figure. 18. Band structures and density of states of the (a) Cs_2MoI_6, (b) Cs_2MoBr_6, (c) Cs_2MoCl_6, (d) Cs_2SnI_6, (e) Cs_2SnBr_6, (f) Cs_2SnCl_6 calculated by PBE functional.

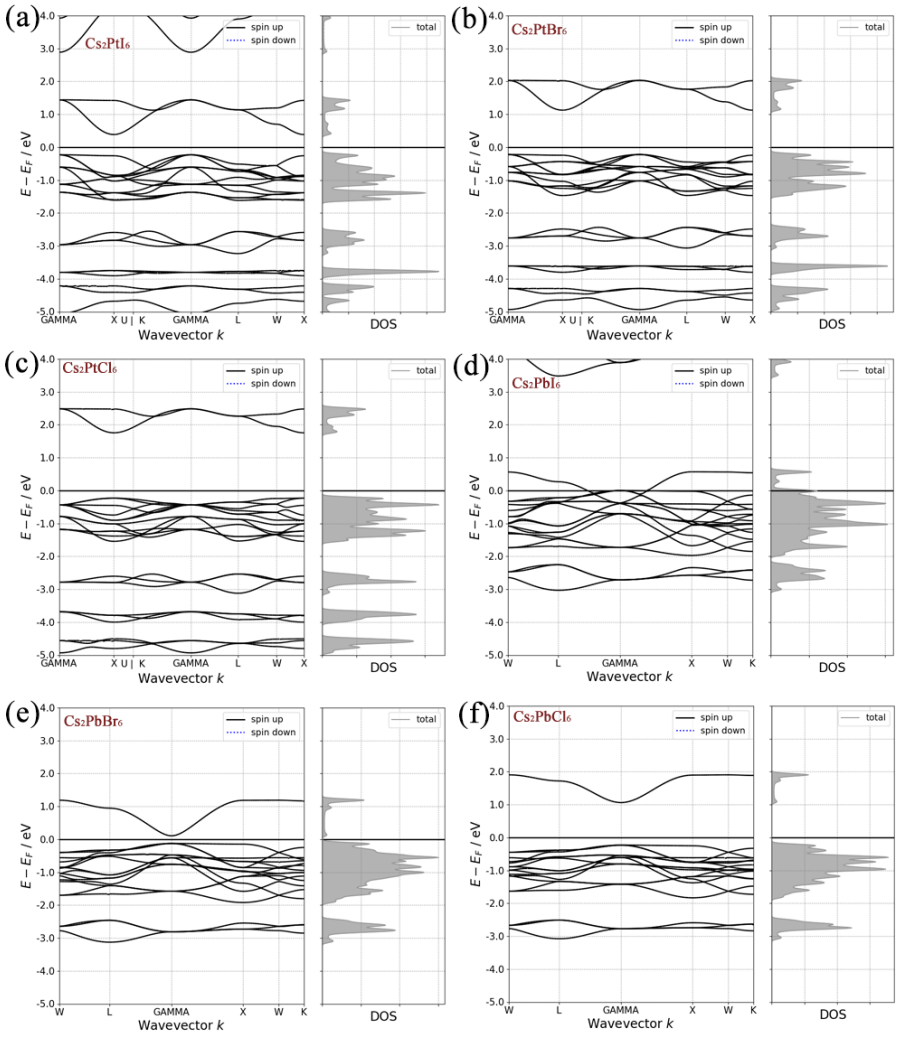

Figure. 19. Band structures and density of states of the (a) Cs_2PtI_6, (b) Cs_2PtBr_6, (c) Cs_2PtCl_6, (d) Cs_2PbI_6, (e) Cs_2PbBr_6, (f) Cs_2PbCl_6 calculated by PBE functional.

According to the theoretical calculation results, the bandgap of perovskites containing Zr and Hf is too large for single-junction perovskite solar cells, but structures combining Mo with halogens generated exceptionally narrow bandgaps and may even exhibit metallic properties as shown in Fig. 20. It can be assumed that the researched perovskites, when made up of cesium-based double perovskites, do not have the potential to produce a single solar cell worth looking forward to. Note that for the change of B-site cations in Hf, Zr, and Ti as well as Pt and Pd, the bandgap increases with the ionic radius increase. However, chemical trend was not observed in the Ge, Sn, and Pb. The transition from chloride to bromide to iodide gradually narrows the bandgap; it will have reference significance for the bandgap regulation engineering of perovskites.

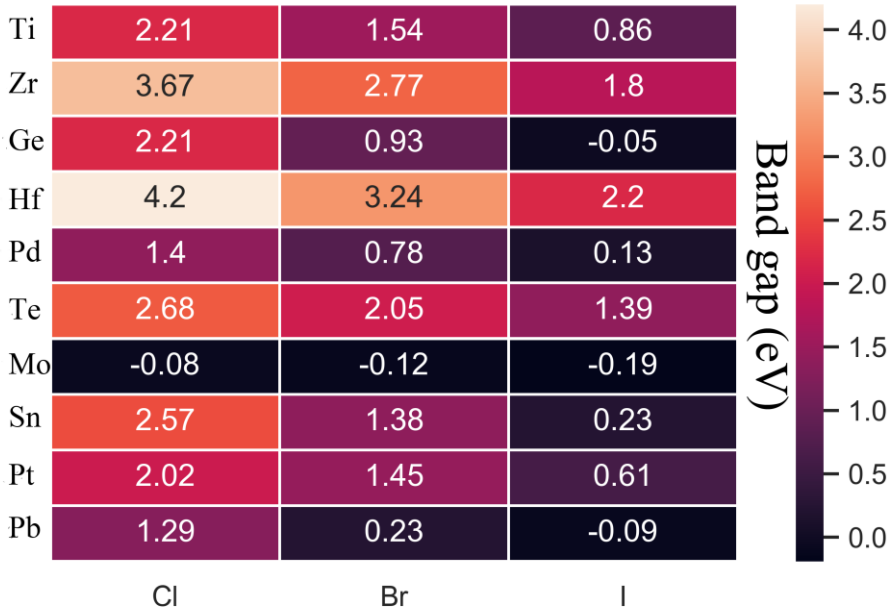

Figure. 20. Results of bandgap prescreening of the studied 30 perovskites.

Cs_2TiBr_6, Cs_2TiI_6, Cs_2GeBr_6, Cs_2PdCl_6, Cs_2PdBr_6, Cs_2TeI_6, Cs_2SnBr_6, Cs_2PtBr_6, Cs_2PtI_6, and Cs_2PbCl_6 were chosen for the calculation of the band structure using HSE+SOC functional, which is well known to give a more accurate estimate for the periodic systems bandgaps, the bandgap of Cs_2TeI_6 (1.61 eV) belongs to the boundary value of the screening range, so it was also considered. All studied materials calculated bandgaps with HSE+SOC are listed in Table 2, and some experimental bandgaps from other literature studies are included in Table 3. As expected, the theoretical results demonstrate that the bandgap of all materials increased to a certain extent. The exact increase, however, is dependent on specific metals and halogens. From this screening study, 5 perovskites, Cs_2TiI_6, Cs_2GeBr_6, Cs_2PtI_6, Cs_2PdBr_6, and Cs_2TeI_6 were chosen, exhibiting indirect bandgaps except for Cs_2GeBr_6, as shown in Fig. 21. The valence band (VB) maximum and the conduction band (CB) minimum are at the GAMMA and X points, respectively. Cs_2TiI_6, Cs_2GeBr_6, Cs_2PdBr_6, Cs_2TeI_6, and Cs_2PtI_6 were chosen as ideal target materials, and their

optical properties were further studied. Note that the bandgaps difference between PBE and HSE + SOC of the studied materials is about 0.6 eV, however this difference seems to be greatly affected by the cations at the B position. Using Cs_2TeI_6 and Cs_2PtI_6 with small and large differences of two functional (PBE and HSE+SOC) bandgaps as a reference, respectively, their experimental bandgaps (1.59 eV of Cs_2TeI_6 [19] and 1.37 eV of Cs_2PtI_6 [11]) are very close to the predicted bandgaps, indicating that the calculation method used for this study is feasible.

Table 2 Calculated bandgaps of HSE functional with SOC.

Compound	E_g (HSE-SOC) /eV
Cs_2TiBr_6	2.16
Cs_2TiI_6	1.32
Cs_2GeBr_6	1.50
Cs_2PdCl_6	2.03
Cs_2PdBr_6	1.22
Cs_2TeI_6	1.61
Cs_2SnBr_6	1.95
Cs_2PtBr_6	2.33
Cs_2PtI_6	1.39
Cs_2PbCl_6	1.99

Table 3 Calculated band gaps with PBE (GGA), HSE+SOC functional and experimental band gap of Cs_2BX_6 compounds perovskites.

Compound	E_g (GGA-PBE)/eV	E_g (HSE-SOC) /eV	Expt. /eV
Cs_2TiCl_6	2.21		
Cs_2TiBr_6	1.54	2.16	2.00[31]
Cs_2TiI_6	0.86	1.32	1.02[35]
Cs_2ZrCl_6	3.67		
Cs_2ZrBr_6	2.77		

Cs_2ZrI_6	1.80		
Cs_2GeCl_6	2.21		
Cs_2GeBr_6	0.93	1.50	
Cs_2GeI_6	-0.05		
Cs_2HfCl_6	4.20		
Cs_2HfBr_6	3.24		
Cs_2HfI_6	2.20		
Cs_2PdCl_6	1.40	2.03	
Cs_2PdBr_6	0.78	1.22	
Cs_2PdI_6	0.13		
Cs_2TeCl_6	2.68		
Cs_2TeBr_6	2.05		
Cs_2TeI_6	1.39	1.61	1.59[19]
Cs_2MoCl_6	-0.08		
Cs_2MoBr_6	-0.12		
Cs_2MoI_6	-0.19		
Cs_2SnCl_6	2.57		
Cs_2SnBr_6	1.38	1.95	
Cs_2SnI_6	0.23		
Cs_2PtCl_6	2.02		
Cs_2PtBr_6	1.45	2.33	2.85[66]
Cs_2PtI_6	0.61	1.39	1.37[11]
Cs_2PbCl_6	1.29	1.99	
Cs_2PbBr_6	0.23		
Cs_2PbI_6	-0.09		

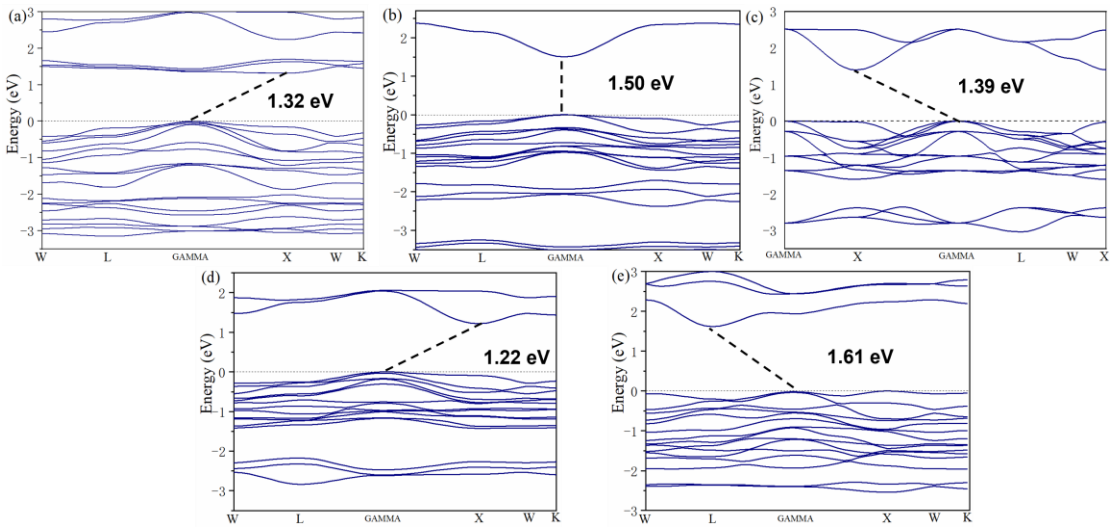

Figure. 21. Band structures of the (a) Cs_2TiI_6, (b) Cs_2GeBr_6, (c) Cs_2PtI_6, (d) Cs_2PdBr_6 and (e) Cs_2TeI_6 calculated by HSE+SOC method.

The DOS was used to further study the electronic properties of selected compounds. The total density of states (TDOS) and partial density of states (PDOS) plots are shown in Fig. 22. All the materials exhibit a semiconducting nature since the TDOS of VB doesn't go through the Fermi level. Electronic contribution of the individual atoms in the stabilized structure is clarified by the knowledge on orbital properties. It can be seen from Fig. 22a, b, that the Cs orbitals of Cs_2TiI_6 are located deep in the VB (~ -8 eV), making little contribution to the VB and CB near the Fermi level. The d states of Ti exist in the core region of VB (~ -2 eV) and at the bottom of CB. In a valence band edge (VBE), the major contribution comes from the p orbital of I, and the electrons transition from the VB to the CB after the carriers gain energy. For Cs_2GeBr_6 (Fig. 22c, d), the VBE is mainly contributed by Cs and Br-p orbitals, where Cs is also presented deep in the VB and CB (~ ±7 eV). The CB region near the Fermi level is composed of Br-p orbitals, while Ge-d orbitals mainly contribute to the core region of CB. A similar situation is observed for the Cs_2PtI_6 (Fig. 22e, f), Cs_2PdBr_6 (Fig. 22g, h), and Cs_2TeI_6 (Fig. 22i, j), concerning Cs_2TiI_6, the Cs orbitals of these four materials are located far away from the Fermi level, indicating that the Cs has little effect on the band edge states. Moreover, their conduction band edge (CBE) is formed due to the mix contribution of Pt/Pd/Te/Ti-d and Br/I-p orbitals. Through the band states of Cs_2PtI_6 and Cs_2PdBr_6, it can be observed that the d orbitals of B-site metal substituted cations and the p orbitals of halogen ions have obvious interaction, which usually affects

the thermoelectric properties of materials.[48] A minor contribution from other states also exists, but their overall influence can be ignored.

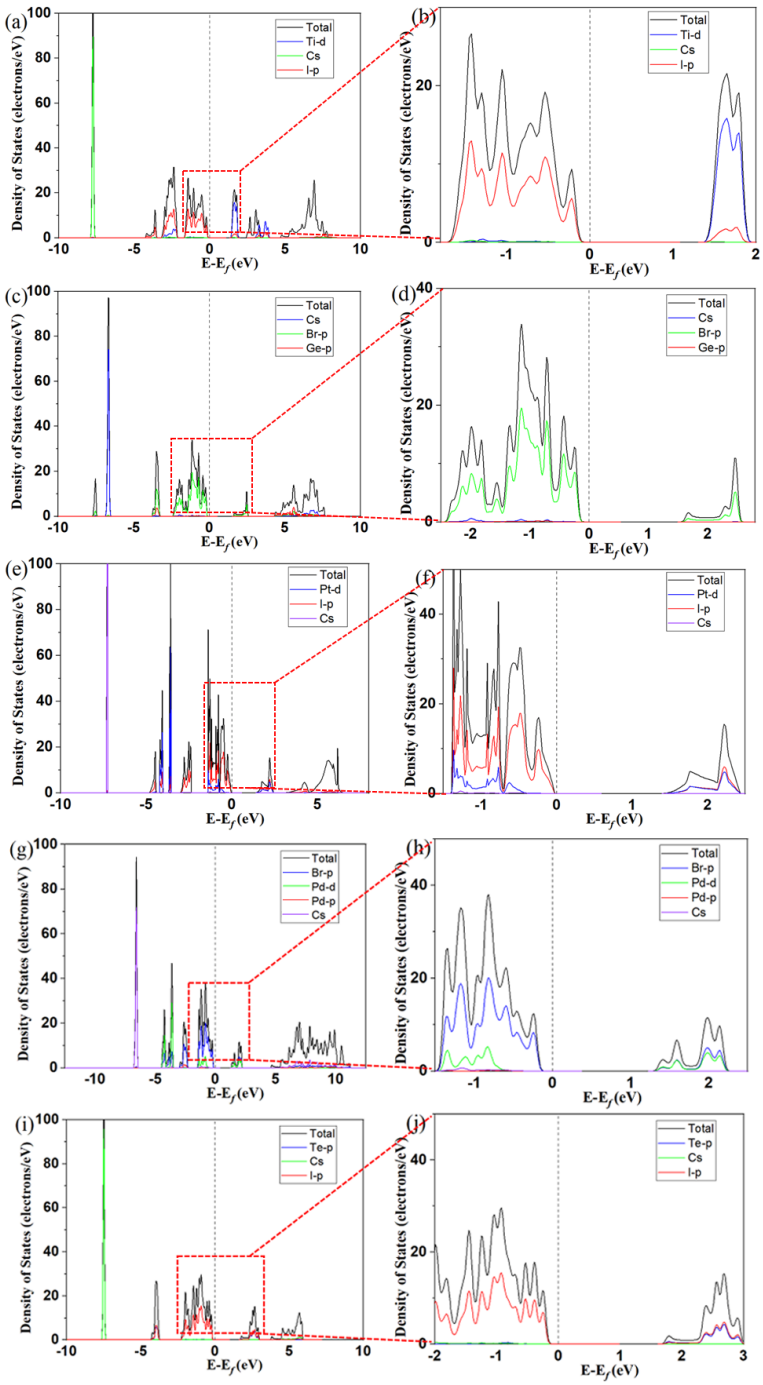

Figure. 22. The DOS of the (a, b) Cs_2TiI_6, (c, d) Cs_2GeBr_6, (e, f) Cs_2PtI_6, (g, h) Cs_2PdBr_6, (i, j) Cs_2TeI_6. Fermi energy is set to zero.

4.3.3 Optical properties

The energy-dependent dielectric constants (ε(ω)) and optical absorption of these 5 candidate structures (Cs_2TiI_6, Cs_2GeBr_6, Cs_2PtI_6, Cs_2PdBr_6, and Cs_2TeI_6), which are suitable for solar cells within the appropriate bandgap range were further studied to evaluate their optical properties, as shown in Fig. 23.

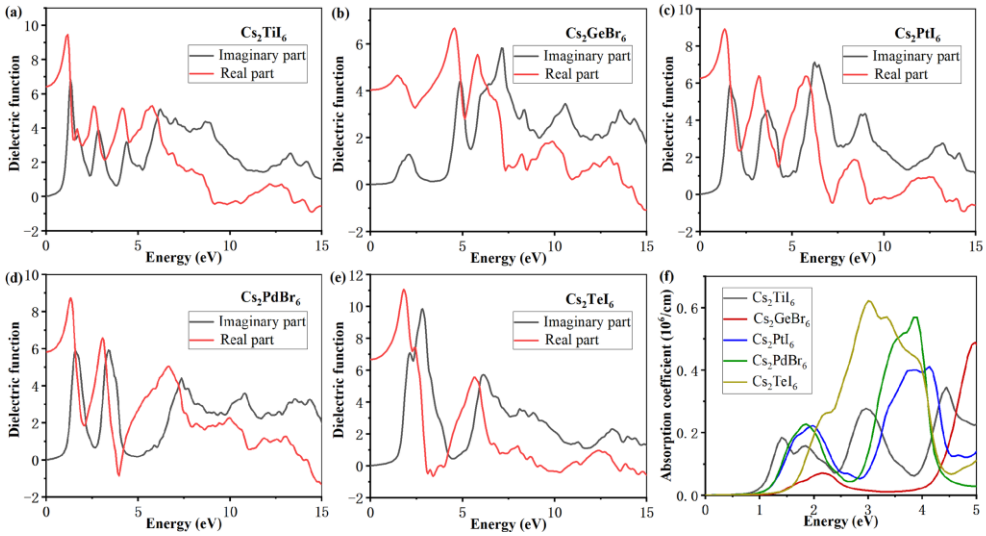

Figure. 23. Variation of imaginary and real part of dielectric constant of (a) Cs_2TiI_6, (b) Cs_2GeBr_6, (c) Cs_2PtI_6, (d) Cs_2PdBr_6 and (e) Cs_2TeI_6. (f) Optical absorption for 5 studied double perovskite.

The optical properties of solid materials are very sensitive to the nature of bandgap, electron recombination rate as well as electron-photon interaction. Because various optical parameters, e.g., refractive index, absorption, conductivity, reflectivity, and loss function, are calculated by dielectric constant, it is very important to describe the optical properties of any material. The frequency-dependent complex dielectric function can be obtained using Kramers-Kronig equations:

$$\varepsilon(\omega) = \varepsilon_1(\omega) + \varepsilon_2(\omega) \tag{4}$$

which has been calculated using PBE functional, as shown in Fig. 23 (a–e). The ω represents the angular frequency of electromagnetic radiations. The $\varepsilon_1(\omega)$ (real part of the dielectric constant) shows the dispersion and polarization of the impinging light, while the $\varepsilon_2(\omega)$ (imaginary part) illustrates light absorption by materials. The calculated $\varepsilon_1(\omega)$ and $\varepsilon_2(\omega)$ of Cs_2TiI_6 are plotted

against incident energy in Fig. 23a. The $\varepsilon_1(0)$ (static dielectric constant) can be extracted from the low energy limit of $\varepsilon_1(\omega)$, which starts at 6.43 and changes with the energy of the incident electromagnetic waves. It also appears that there are three resonance peaks of $\varepsilon_1(\omega)$ in the low energy range at 1.19 eV, 2.67 eV, and 4.15 eV. These peaks express the maximum dispersion of light and specific light energy where it is plane-polarized.[58] In addition, the $\varepsilon_1(\omega)$ curve goes through zero from the energy of 8.97 eV, while the value of $\varepsilon_1(\omega)$ is positive in the lower energy region (0-5 eV) and ensures the prevailing semiconducting behavior. [59] If the $\varepsilon_1(\omega)$ of the dielectric function is negative, which means that the region where the photon is coupled with the plasma will have total reflection and form a quasi-particle called polaron. The larger the dielectric constant, the stronger the ability of the dielectric to bind the electron, and the less likely the electron is to be polarized.[60] Not only Cs_2TiI_6, but also other compounds studied show good dielectric constants conducive to optical applications in visible spectrum. To further evaluate the application of photoelectric/solar cells, the absorption coefficients $\alpha(\omega)$ are calculated from $\varepsilon_1(\omega)$ and $\varepsilon_2(\omega)$ by using the following equation.

$$\alpha(\omega) = \sqrt{2}\omega\left\{\sqrt{\varepsilon_1^2(\omega) + \varepsilon_2^2(\omega)} - \varepsilon_1(\omega)\right\}^{\frac{1}{2}} \quad (5)$$

The calculated values of the $\alpha(\omega)$ are shown in Fig. 23f, which describes how much light energy is absorbed by the semiconductor. The $\varepsilon_2(\omega)$ also reflects the light absorption capacity of the material. Comparing the curves of the $\varepsilon_2(\omega)$ and $\alpha(\omega)$, we can find a similar trend, and the displacements of some peaks are due to the different theoretical approximation methods used in the calculation of these two. All the materials studied have several absorption peaks in the energy range of more than 1 eV, which indicates that these materials are perfect for optoelectronic devices functional in ultraviolet and visible light. The Cs_2TeI_6 has a peak absorption value of about 0.62×10^6 cm^{-1} in visible spectrum (1.6 – 3.2 eV), which is higher than that of other compounds. In contrast, Cs_2GeBr_6 only has the lowest absorption peak only at 2.1 eV, which is unfavorable to photoelectric performance in the visible range compared with the absorption curve of other compounds.

4.3.4 Solar water splitting

Considering that the bandgap of Cs_2TeI_6, Cs_2TiBr_6, Cs_2PdCl_6, Cs_2SnBr_6, Cs_2PbCl_6, and Cs_2PtBr_6 halide double perovskites is too large for the application of single-junction solar cells,

their performance as photocatalysts in solar water splitting was studied, as shown in Fig. 24. In the photocatalytic reaction, semiconductor compounds are usually in different phases from the reactants, so they are often used as heterogeneous photocatalysts. According to the reaction mechanism displayed in Fig. 24a, when the energy of incident light is greater than the material's bandgap, the excited electrons of semiconductors undergo the interband transition from the VB to the CB, separating holes and photogenerated electrons. After that, the separated holes and electrons can react directly with water molecules adsorbed on the surface-active sites of the photocatalyst to produce H_2 and O_2. The key to driving the water-splitting reaction is the bandgap and potential of VBE and CBE in semiconductor photocatalyst.

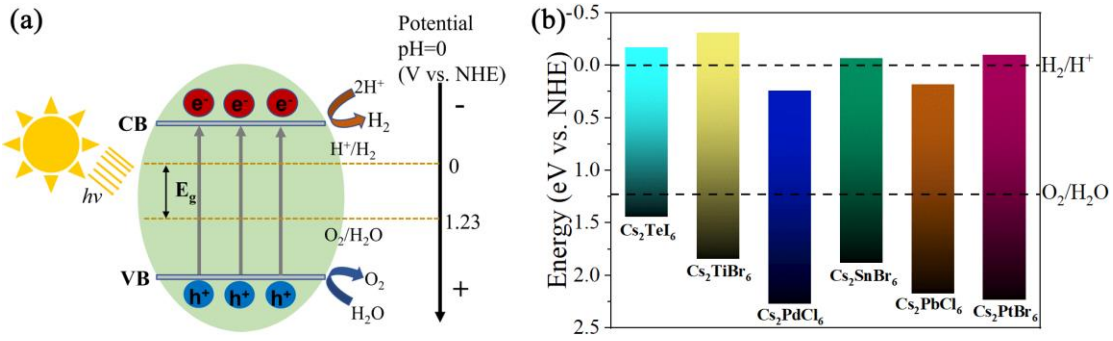

Figure. 24. (a) Schematic diagram of the basic reaction mechanism of the photocatalytic water splitting. (b) Conduction band bottom and Valence band top of the Cs_2TeI_6, Cs_2TiBr_6, Cs_2PdCl_6, Cs_2SnBr_6, Cs_2PbCl_6 and Cs_2PtBr_6. Dotted lines represent the oxidation (O_2/H_2O) and reduction (H_2/H^+) potential of water.

For the photocatalytic reaction to proceed normally, the top potential of VB of the semiconductor needs to be higher than the redox potential of O_2 / H_2O (+1.23 V relative to a normal hydrogen electrode (NHE)), while the bottom potential of CB needs to be lower than the redox potential of H^+ / H_2 (0 V relative to NHE). Therefore, the minimum bandgap required to drive the water-splitting reaction is 1.23 eV. According to the thermodynamic theory, the appropriate potential distribution and bandgap position of the photocatalyst with a minimum bandgap of 1.23 eV are the necessary and sufficient conditions for solar water splitting. However, the oxidation and reduction processes of H_2O are four-electron and two-electron multistep reactions, respectively. There is an activation barrier between water molecules and photocatalyst in the electron transfer process, which leads to the water oxidation and reduction reaction needing a high overvoltage to drive, and the incident photons' energy must be higher than the bandgap of the

photocatalyst. Therefore, the lower limit of bandgap must be much higher than 1.23 eV to drive the whole water splitting. Generally, semiconductors with a bandgap between 1.6 and 2.4 eV have practical value. [61–63] The bandgaps of Cs_2TeI_6, Cs_2TiBr_6, Cs_2PdCl_6, Cs_2SnBr_6, Cs_2PbCl_6, and Cs_2PtBr_6 halide double perovskites are all in this ideal range based on HSE+SOC calculation. According to the previous research results, the positions of the VBE and CBE can be obtained by the following empirical formula.[64]

$$E_{\mathrm{CBE}} = (\chi_{Cs}^2 \chi_B \chi_X^6)^{\frac{1}{9}} - \frac{1}{2} E_g + E_0 \quad (6)$$

$$E_{\mathrm{VBE}} = E_{CBE} + E_g \quad (7)$$

Where E_{CBE} and E_{VBE} are the CBE and VBE potential of perovskites, respectively. The χ refers to the absolute electronegativity of the atoms Cs, B, and X of Cs_2BX_6.[65] E_g is the bandgap, and E_0 is −4.5 eV for NHE, which show the scale factor from the redox level of the reference electrode to the absolute vacuum scale. Fig. 24b and Table 4 show the calculation results of the six double perovskite potentials studied. Among them, the VBE of Cs_2TeI_6, Cs_2TiBr_6, Cs_2SnBr_6, and Cs_2PtBr_6 is lower than the oxidation potential of water, while the CBE is higher than the standard potential of NHE. The band edge position and wide bandgap of these perovskites indicate that they can be active under visible light and used as photocatalysts for water splitting. These results show that perovskite's properties are strongly related to the composition of B cations and halogen ions.

Table. 4. The absolute electronegativity (χ), band gap (E_g), computed CBE, and VBE potential at a vacuum level of selected perovskites.

Compound	χ_{Cs}	χ_B	χ_X	E_g /eV	CBE/eV	VBE/eV
Cs_2TeI_6	2.18	5.49	6.76	1.61	-4.33	-5.94
Cs_2TiBr_6	2.18	3.45	7.59	2.16	-4.19	-6.35
Cs_2PbCl_6	2.18	3.90	8.30	1.99	-4.68	-6.67
Cs_2PdCl_6	2.18	4.45	8.30	2.03	-4.74	-6.77
Cs_2SnBr_6	2.18	2.77	7.59	1.95	-4.43	-6.38
Cs_2PtBr_6	2.18	5.60	7.59	2.33	-4.40	-6.73

4.4 Conclusions

In the context of the growing need for clean energy and attention to environmental protection technology, the development and application of solar cells and photocatalysis are important technologies for renewable energy. However, as a highly concerned photoelectric material and catalyst, the lead-based perovskite cannot be widely accepted due to its toxicity. The environmental friendly materials are urgently needed to overcome the main bottleneck for application. Through the theoretical prediction results of perovskite properties covering various elements, then the promising alternatives can be found to lead-containing perovskite and the development of environmental friendly materials may be accelerated. In this work, structural, electronic, and optical properties of Cs_2BX_6 compounds were calculated using first-principles calculations of PBE and HSE-SOC methods, with 30 combinations of B = Ti, Zr, Ge, Hf, Pd, Te, Mo, Sn, Pt, and Pb cations, X = Cl, Br, and I halogen ion. A pre-screen for perovskites based on their stability and predicted bandgaps at PBE level were driven. The calculated enthalpy of formation is negative, which demonstrates that the cesium-based halide perovskite possesses excellent thermal stability at 0 K. The trend of tolerance factor shows that the contribution of Cl^- to structural stability is greater than Br^- and I^-, which is consistent with the calculated formation enthalpy result. The calculated bandgap of perovskites containing Zr and Hf is too large for single-junction perovskite solar cells, while structures combining Mo also gave extremely narrow bandgaps. Furthermore, the theoretical results also revealed that all perovskites studied conforms to the typical trend of replacing halogen (Cl > Br > I) to adjust the bandgap. When the B-site cation belongs to the (Hf, Zr, Ti) group and (Pt, Pd) group, the bandgap value is directly proportional to the cation size of this group. It has guiding significance for applying Cs-based halide double perovskite bandgap engineering. After that, 10 compounds that satisfy the screening criteria were selected, and the HSE+SOC method was used to calculate their bandgap values accurately. The smallest bandgap among selected perovskites is predicted for Cs_2PdBr_6 with a bandgap of 1.22 eV, and the largest one is Cs_2PtBr_6 with a bandgap of 2.33 eV. The optical properties of perovskites with a bandgap of less than 1.6 eV were studied. They have multiple absorption peaks in the energy range above 1 eV, indicating that they are suitable for optoelectronic devices under visible and ultraviolet light. For perovskites with a bandgap higher than 1.6 eV, their performance as photocatalysts in solar water

splitting was studied. The band edge positions of Cs_2TeI_6, Cs_2TiBr6, Cs_2SnBr_6, and Cs_2PtBr_6 are matched the water redox potential. The prediction of stable materials with 1.22 ~ 2.33 eV bandgap will be helpful to promote the experimental research for novel optoelectronic devices. The DFT study can provide theoretical guidance and support the rational design of high-performance double perovskites for optoelectronic applications of solar cells and solar water splitting.

References

1 Burschka J, Pellet N, Moon S, et al. Sequential deposition as a route to high-performance perovskite-sensitized solar cells. *Nature*. **2013**;499:316-319.

2 Chen Y, Lei Y, Li Y, et al. Strain engineering and epitaxial stabilization of halide perovskites. *Nature*. **2020**;577:209-215.

3 Tong J, Gong J, Hu M, et al. High-performance methylammonium-free ideal-band-gap perovskite solar cells. *Matter*. **2021**;4:1365-1376.

4 Zhang Y, Wen J, Xu Z, et al. Effective phase-alignment for 2D halide perovskites incorporating symmetric diammonium ion for photovoltaics. *Adv. Sci.* **2021**;8:2001433.

5 Kojima A, Teshima K, Shirai Y, et al. Organometal halide perovskites as visible-light sensitizers for photovoltaic cells. *J. Am. Chem. Soc.* **2009**;131:6050-6051.

6 Best Research-Cell Efficiency Chart. Photovoltaic Research NREL. https://www.nrel.gov/pv/assets/pdfs/cell-pv-eff-emergingpv.202001042.pdf.

7 Chen P, Ong W, Shi Z, et al. Pb-Based Halide Perovskites: Recent Advances in Photo(electro)catalytic Applications and Looking Beyond. *Adv. Funct. Mater*. **2020**;30:1909667.

8 Ogawa K, Suzuki H, Zhong C, et al. Layered Perovskite Oxyiodide with Narrow Band Gap and Long Lifetime Carriers for Water Splitting Photocatalysis. *J. Am. Chem. Soc*. **2021**;143:8446-8453.

9 Shi M, Li R, Li C, et al. Halide perovskites for light emission and artificial photosynthesis: Opportunities, challenges, and perspectives. *EcoMat*. **2021**;3:e12074.

10 Fan Q, Biesold-McGee G, Ma J, et al. Lead-Free Halide Perovskite Nanocrystals: Crystal Structures, Synthesis, Stabilities, and Optical Properties. *Angew. Chem., Int. Ed.* **2020**; 59:1030-1046.

11 Yang S, Song X, Gao L, et al. A novel Lead-free material Cs2PtI6 with Narrow Bandgap and Ultra-Stable for Its Photovoltaic Application. *ACS Appl. Mater. Interfaces*. **2020**;40:44700-44709.

12 Babayigit A, Ethirajan A, Muller M, et al. toxicity of organometal halide perovskite solar cells. *Nat. Mater*. **2016**;15:247.

13 Needleman H. Lead Poisoning. *Annu. Rev. Med.* **2004**;55:209.

14 Hao F, Stoumpos C, Cao D, et al. Lead-freesolid-state organic-inorganic halide perovskite solar cells. *Nat. Photonics*. **2014**;8:489-494.

15 Noel N, Stranks S, Abate A, et al. Leadfree organic-inorganic tin halide perovskites for photovoltaic applications. *Energy Environ. Sci.* **2014**;7:3061-3068.

16 Filip M, Giustino F. Computational screening of homovalent lead substitution in organic-inorganic halide perovskites. *J. Phys. Chem. C.* **2016**;120:166-173.

17 Körbel S, Marques M, Botti S. Stability and electronic properties of new inorganic perovskites from high-throughput ab initio calculations. *J. Mater. Chem. C*. **2016**;4:3157-3167.

18 Volonakis G, Haghighirad A, Milot R, et al. $Cs_2InAgCl_6$: A New Lead-Free Halide Double Perovskite with Direct Band Gap. *J. Phys. Chem. Lett*. **2017**;8:772-778.

19 Maughan A, Ganose A, Bordelon M, et al. Defect Tolerance to Intolerance in the Vacancy-Ordered Double Perovskite Semiconductors Cs_2SnI_6 and Cs_2TeI_6. *J. Am. Chem. Soc.* **2016**;138:8453-8464.

20 Chang T, Wei Q, Zeng R, et al. Efficient Energy Transfer in Te^{4+}-Doped Cs_2ZrCl_6 Vacancy-Ordered Perovskites and Ultrahigh Moisture Stability via A-Site Rb-Alloying Strategy. *J. Phys. Chem. Lett.* **2021**;12:1829-1837.

21 Tai Q, Tang K, Yan F. Recent progress of inorganic perovskite solar cells. *Energy Environ. Sci.* **2019**;12:2375-2405.

22 Meng Y, Ahmadi M, Wu X, et al. High performance and stable all-inorganic perovskite light emitting diodes by reducing luminescence quenching at PEDOT:PSS/Perovskites interface. *Org. Electron*. **2019**;64:47-53.

23 An J, Jiang H, Tian Y, et al. Manganese doping mechanism in a $CsPbI_2Br$ photovoltaic material: a first-principles study. *Phys. Chem. Chem. Phys*. **2019**;21:23552-23558.

24 Kumar A, Swami S, Rawat S, et al. Mixed bismuth-antimony-based double perovskite nanocrystals for solar cell application. *Int. J. Energ. Res*. **2021**;45:16769-16780.

25 Liu S, Guan Y, Sheng Y, et al. A Review on Additives for Halide Perovskite Solar Cells. *Adv. Energy Mater.* **2020**;10:1902492.

26 Tong G, Ono L, Qi Y. Recent Progress of All-Bromide Inorganic Perovskite Solar Cells. *Energy Technol.* **2020**;8:1900961.

27 Liang J, Wang C, Wang Y, et al. All-inorganic perovskite solar cells. *J. Am. Chem. Soc*. **2016**;138:15829-15832.

28 Saliba M, Matsui T, Seo J, et al. Cesium-containing triple cation perovskite solar cells: improved stability, reproducibility and high efficiency. *Energy Environ. Sci*. **2016**; 9:1989-1997.

29 Abfalterer A, Shamsi J, Kubicki D, et al. Colloidal Synthesis and Optical Properties of Perovskite-Inspired Cesium Zirconium Halide Nanocrystals. *ACS Mater. Lett*., **2020**;2:1644-1652.

30 Qiu X, Wang, Cao B, Yuan S, et al. From unstable $CsSnI_3$ to air-stable Cs_2SnI_6: A lead-free perovskite solar cell light absorber with bandgap of 1.48 eV and high absorption coefficient. *Sol. Energy Mater. Sol. Cells*. **2017**;159:227-234.

31 Euvrard J, Wang X, Li T, et al. Is Cs_2TiBr_6 a promising Pb-free perovskite for solar energy applications? *J. Mater. Chem. A*. **2020**;8:4049-4054.

32 Brik M, Kityk I. Modeling of Lattice Constant and their Relations with Ionic Radii and Electronegativity of Constituting Ions of A_2XY_6 Cubic Crystals (A=K, Cs, Rb, Tl; X=Tetravalent Cation, Y=F, Cl, Br, I). *J. Phys. Chem. Solids*. **2011**;72:1256-1260.

33 Kaltzoglou A, Antoniadou M, Kontos A, et al. Optical-Vibrational Properties of the Cs_2SnX_6 (X = Cl, Br, I) Defect Perovskites and Hole-Transport Efficiency in Dye-Sensitized Solar Cells. *J. Phys. Chem. C*. **2016**;120:11777-11785.

34 Chakraborty K, Choudhury M, Paul S. Study of Physical, Optical, and Electrical Properties of Cesium Titanium (IV)-Based Single Halide Perovskite Solar Cell. *IEEE J. Photovolt*. **2021**;11:386-390.

35 Ju M, Chen M, Zhou Y, et al. Earth-Abundant Nontoxic Titanium(IV)-based Vacancy-Ordered Double Perovskite Halides with Tunable 1.0 to 1.8 eV Bandgaps for Photovoltaic Applications. *ACS Energy Lett.* **2018**;3:297-304.

36 Kresse G, Furthmuller J. Efficiency of ab-initio total energy calculations for metals and semiconductors using a plane-wave basis set. *Comput. Mater. Sci.*, **1996**;6:15-50.

37 Perdew J, Burke K, Ernzerhof M. Generalized Gradient Approximation Made Simple. *Phys. Rev. Lett.* **1996**;77:3865-3868.

38 Heyd J, Scuseria G. Ernzerhof M. Hybrid functionals based on a screened Coulomb potential. *J. Chem. Phys.* **2003**;118:8207-8215.

39 Blöchl P. Projector augmented-wave method. *Phys. Rev. B*. **1994**;50:17953-17979.

40 Liu D, Sa R. Theoretical study of Zr doping on the stability, mechanical, electronic and optical properties of Cs_2TiI_6. *Opt. Mater.* **2020**;110:110497.

41 Li W, Zhu S, Zhao Y, et al. Structure, electronic and optical properties of $Cs_2Ti(Br_{1-x}Y_x)_6$ (Y = Cl, I; x = 0, 0.25, 0.5, 0.75, 1) perovskites: the first principles investigations. *J. Solid State Chem.* **2020**;284:121213.

42 Kar M, Körzdörfer T. Computational high throughput screening of inorganic cation based halide perovskites for perovskite only tandem solar cells. *Mater. Res. Express*. **2020**;7:055502.

43 Peedikakkandy L, Bhargava P. *RSC Adv.* **2016**;6:19857-19860.

44 Opahle I, Madsen G, Drautz R. High throughput density functional investigations of the stability, electronic structure and thermoelectric properties of binary silicides. *Phys. Chem. Chem. Phys*. **2012**;14:16197-16202.

45 Thiele G, Mrozek C, Kämmerer D, et al. Über Hexaiodoplatinate(IV) M_2PtI_6 (M = K, Rb, Cs, NH_4, Tl) Darstellungsverfahren, Eigenschaften und Kristallstrukturen / on Hexaiodoplatinates(IV) M_2PtI_6 (M = K, Rb, Cs, NH_4, Tl)-preparation, properties and structural data. *Z. Naturforschung B*. **1983**;38:905-910.

46 Ferrari A, Coghi L. On the existence of hexahalogenoaurates. *Gazz Chim Ital*. **1941**;71:440-441.

47 Engel G, Kristallogr Z. Die Kristallstrukturen einiger Hexachlorokomplexsalze. *Cryst Mater.* **1935**;90:341-373.

48 Faizan M, Bhamu K, Murtaza G, et al. Electronic and optical properties of vacancy ordered double perovskites A_2BX_6 (A= Rb, Cs; B= Sn, Pd, Pt; and X= Cl, Br, I): a first principles study. *Sci. Rep.* **2021**;11:1-9.

49 Eva Z. Discovering New Materials via A Priori Crystal Structure Prediction. *Rev. Comput. Chem.* **2016**;29:274-326.

50 Goldschmidt V. Die gesetze der krystallochemie. *Naturwiss*. **1926**;14:477-485.

51 Li C, Soh K, Wu P. Formability of ABO_3 perovskites. *Alloys Compd*. **2004**;372:40-48.

52 Li C, Lu X, Ding W, et al. Formability of ABX_3 (X = F, Cl, Br, I) halide perovskites. *Acta Crystallogr. Sect. B: Struct. Sci*. **2008**;64:702-707.

53 Igbari F, Wang Z, Liao L. Progress of Lead-Free Halide Double Perovskites. *Adv. Energy Mater*. **2019**;9:1803150.

54 Fedorovskiy A, Drigo N, Nazeeruddin M. The Role of Goldschmidt's Tolerance Factor in the Formation of A_2BX_6 Double Halide Perovskites and its Optimal Range. *Small Methods*. **2020**;4:1900426.

55 Bartel C, Sutton C, Goldsmith B, et al. *Sci. Adv*. **2019**;5:eaav0693.

56 Hamdan M, Chandiran A. *Angew. Chem.* **2020**;132:16167-16172.

57 Loferski, J. Theoretical considerations governing the choice of the optimum semiconductor for photovoltaic solar energy conversion. *J. Appl. Phys*. **1956**; 27:777-784.

58 Mahmood Q, Hassan M, Yousaf N, et al. Study of lead-free double perovskites halides Cs_2TiCl_6, and Cs_2TiBr_6 for optoelectronics, and thermoelectric applications. *Mater. Sci. Semicond. Process.* **2022**;137:106180.

59 Noor N, Mahmood Q, Rashid M, et al. The pressure-induced mechanical and optoelectronic behavior of cubic perovskite $PbSnO_3$ via ab-initio investigations, *Ceram. Int.* **2018**;44:13750-13756.

60 Mahmood Q, Hassan M, Flemban T, et al. Optoelectronic and thermoelectric properties of double perovskite Rb_2PtX_6 (X = Cl, Br) for energy harvesting: First-principles investigations. *J. Phys. Chem. Solids*. **2020**;148:109665.

61 Kim J, Hansora D, Sharma P, et al. Toward practical solar hydrogen production-an artificial photosynthetic leaf-to-farm challenge. *Chem. Soc. Rev.* **2019**;4:1908.

62 Huang Y, Liu J, Deng Y, et al. The application of perovskite materials in solar water splitting. *J. Semicond*. **2020**;41:011701.

63 Luo J, Zhang W, Yang H, et al. Halide perovskite composites for photocatalysis: A mini review. *EcoMat*. **2021**;3:e12079.

64 Xu Y, Schoonen M. The absolute energy positions of conduction and valence bands of selected semiconducting minerals. *Am. Mineral*. **2000**;85:543-556.

65 Pearson R. Absolute electronegativity and hardness: application to inorganic chemistry. *Inorg. Chem.* 1988;27:734-740.

66 Bonomi S, Patrini M, Bongiovanni G, et al. Versatile vapor phase deposition approach to cesium tin bromide materials $CsSnBr_3$, $CsSn_2Br_5$ and Cs_2SnBr_6. *RSC Adv.* **2020**;10:28478.

Chapter 5. Insights into the photocatalytic mechanism of g-C_3N_4/Cs_2BBr_6 heterojunction photocatalysts by density functional theory calculations

5.1 Introduction

Nowadays the world is facing the challenge of achieving environmental sustainability. Growing pollution, limited energy resources on earth, and increasing energy consumption have driven the need for a cleaner environment and alternative energy sources that can meet human demands in a more environmentally friendly way. Therefore, the current research is greatly accelerated in this direction. Photocatalytic reaction is used to decompose water to generate hydrogen, degrade organic pollutants, reduce CO_2, and fix N_2, which can provide a feasible breakthrough for future energy utilization and environmental pollution control.[1,2] Sunlight mainly includes three different kinds of energy radiation (near-infrared (NIR), visible light (vis) and ultraviolet (UV)). According to the light absorption rate of the working photocatalyst, specific energy radiation can be used in the above photocatalytic process. Making full use of sunlight is a key technical issue that should be addressed when designing and developing highly active photocatalysts.[3] In the past decades, more than one hundred kinds of semiconductors have been explored and developed in this field.[2,4-5] Among all the developed photocatalysts, g-C_3N_4 has aroused great research interest in various fields,[6] especially in the production of hydrogen from water splitting. However, the photogenerated electron-hole pairs with high recombination rate in the isolated g-C_3N_4 will reduce the photocatalytic efficiency, and its photocatalytic activity is only moderate.[7] As a result, the performance of g-C_3N_4 based heterojunctions is still unsatisfactory, and the construction of g-C_3N_4 based heterojunctions with excellent photocatalytic performance still needs further exploration.

The co-catalysts can provide active sites for reduction or oxidation reactions to reduce the activation energy, capture charge carriers and inhibiting the recombination of photogenerated electrons and holes.[8] Therefore, the practical application of g-C_3N_4 with poor photocatalytic activity strongly usually requires surface cocatalysts with appropriate type and quantity. Many researchers have tried to combine other semiconductors to improve their photocatalytic activity.

g-C_3N_4/$BiVO_4$,[9] g-C_3N_4/$LaMnO_3$,[10] g-C_3N_4/$BiFeO_3$,[11] g-C_3N_4 modified Ag_3PO_4,[12] etc. These heterojunctions show good photocatalytic performance. In the past few years, lead halide perovskite $APbX_3$ (usually, A=MA^+, FA^+, Cs^+; X= I^-, Br^-, Cl^-), as one of the most attractive semiconductors, has shown great potential in photoelectric applications. Recently, these lead halide perovskite materials have been extended to the field of photocatalysis. Since Park and his colleagues[13] first reported the photocatalytic hydrogen evolution based on $MAPbI_3$ in saturated HI aqueous solution, people have studied various lead halide perovskite and its composites to improve their hydrogen evolution performance.[14-15] However, the inherent toxicity of lead severely limits the application of lead halide perovskite. To overcome these limitations, researchers are focusing on replacing Pb with non-toxic metals.[16-17] In these alternatives, the use of cesium based lead-free double perovskite or its composites as photocatalysts is rarely reported. Wang et al. reported that $Cs_2AgBiBr_6$ double perovskite was first used for the splitting of hydrobromic acid (HBr) under visible light irradiation.[18] Reduced graphene oxide (RGO) with good electron transfer performance and acid stability was introduced to further improve the H_2 production. Tan et al. successfully synthesized Cs_2SnCl_6/C_3N_4 heterojunction photocatalyst by solid grinding method. Through the construction of heterojunction, the charge separation between Cs_2SnCl_6 and C_3N_4 has been significantly promoted, and the photocatalytic activity can be effectively improved under visible light irradiation.[19] It is reported that the heterojunction between perovskite and other semiconductor materials can effectively promote charge separation and maintain the stability of photocatalyst.[20] These results indicate that cesium based lead-free double perovskite may be a promising candidate material for photocatalysis and various other photoelectric applications.

In this work, we used density functional theory (DFT) calculations to study the band structure and density of state (DOS) of monolayer g-C_3N_4/Cs_2BBr_6 (B=Pt, Ti, Sn) heterojunctions. In addition, the interaction between g-C_3N_4 and Cs_2BBr_6 (001) surfaces is systematically studied. After g-C_3N_4 contacts with double perovskites, due to the interaction with the interface, the edge positions of the band of the two semiconductors change, and then different kinds of band arrangements are formed. The insight gained of this work is of direct relevance to the design of new photocatalysts relating to g-C_3N_4 or Cs_2BBr_6.

5.2 Calculation methods

All calculations on the compounds were carried out by the Perdew–Burke–Ernzerhof (PBE)-GGA (generalized gradient approximation) based DFT study in the Vienna Ab initio simulation package (VASP) with a projector augmented waves (PAW) approach.[21-23] The electronic configurations of the Cs, Pt, Sn, Ti, and Br atoms are $[Xe]6s^1$, $[Xe]5d^96s^1$, $[Kr]5s^25p^2$, $[Ar]3d^24s^2$, and $[Ar]3d^{10}4s^24p^5$, respectively. The energy cutoff the plane-wave basis for all compounds was set to 500 eV. A Monkhorst–Pack mesh of 3 × 2 × 1 and 5 ×5 × 1 K-points is used to sample the Brillouin zone for geometry optimizations and electronic structure calculations, respectively. The vacuum space is set to be at least 15 Å to separate the interactions between neighboring slabs. Geometry optimizations were terminated when the energy and force on each ion were reduced below 10^{-4} eV and 0.05 eV/Å. The band alignment between g-C_3N_4 and Cs_2BBr_6 is one central issue of this study. Since PBE functional usually underestimates the band gap of semiconductors,[24] the electronic structures of g-C_3N_4 and Cs_2BBr_6 are calculated using Heyd–Scuseria–Ernzerhof (HSE06) hybrid functional and HSE functional with spin-orbit coupling (SOC), respectively.

5.3 Results and discussions

5.3.1 Geometry structure and stability

Before checking the properties of g-C_3N_4/Cs_2PtBr_6, g-C_3N_4/Cs_2SnBr_6 and g-C_3N_4/Cs_2TiBr_6 heterojunctions, we first investigated the lattice structure of Cs_2BBr_6 (B= Pt, Sn, Ti) bulk and single layer g-C_3N_4. In Fig. 1a, the optimized lattice constant of g- g-C_3N_4 is predicted to be 4.784 Å, which agrees well with previous experimental measurements and theoretical results.[25-26] In the single layer g-C_3N_4, there are three atoms in a g-C_3N_4 unit cell, corresponding to two nitrogen atoms at the edge and corner, and one carbon atom. After structural optimization, the bond lengths of carbon and nitrogen atoms are 1.46 Å and 1.33 Å, which are consistent with previously reported distances of 1.47 and 1.34Å, respectively.[27] The optimized geometry models of Cs_2PtBr_6, Cs_2SnBr_6 and Cs_2TiBr_6 drawn using the VESTA program are illustrated in Fig. 1b-d, the Cs_2BBr_6 has a face-centered cubic structure with space group $Fm\bar{3}m$ (No.225), which is alternately formed by isolated [BX_6] clusters and twisted tetragonal Cs cations (space group P4/mnc). The optimized lattice parameters of Cs_2PtBr_6, Cs_2SnBr_6 and Cs_2TiBr_6 are 11.04 Å, 10.14 Å and 10.81 Å, respectively.

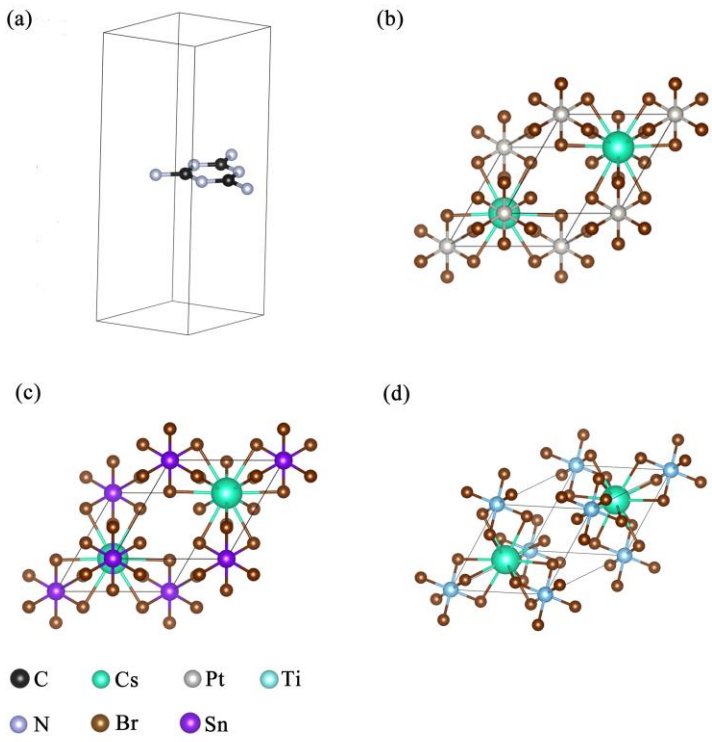

Figure. 1. Optimized geometric structures of (a) monolayer g-C_3N_4,

(b) Cs_2PtBr_6, (c) Cs_2SnBr_6, and (d) Cs_2TiBr_6 primitive cell.

The structural parameters of an optimized in this paper are consistent with those reported in earlier reference.[28-30] Schematic representations of the heterojunctions are reported in Fig. 2. Cs_2BBr_6 (001) surface was selected to construct g-C_3N_4/Cs_2BBr_6 heterojunction. A vacuum layer of 15 Å is used to isolate the slab as the boundary condition, which is good enough to make interactions between neighboring slabs negligible. To examine the vdW interaction, the mismatch ratio and mismatch energies of the relaxed g-C_3N_4/Cs_2BBr_6 heterojunction are calculated after geometry optimization and the results are listed in Table 1. The a% and b% are lattice mismatch ratios of heterojunction occur along the a and b direction, which are less than 3%, and the calculated distance between g-C_3N_4 nanosheet and Cs_2BBr_6 (001) surface is 3.5-5 Å. As shown in Fig. 2, there is a strong interaction between nitrogen and perovskite B metal cation at the interface of the two heterojunctions, which leads to the distortion of g-C_3N_4 plane and the change of bond angle. It is well known that the interlayer interaction will directly affect the thermodynamic stability of the interface structure of the prepared heterojunctions. To analyze the interaction between Cs_2BBr_6 and g-C_3N_4, the binding energy is calculated by the following formula:

$$E_b = E_{g-C_3N_4/Cs_2BBr_6} - E_{g-C_3N_4} - E_{Cs_2BBr_6} \quad (1)$$

where $E_{g-C_3N_4/Cs_2BBr_6}$, $E_{g-C_3N_4}$ and $E_{Cs_2BBr_6}$ represent the total energies of the relaxed g-C_3N_4/Cs_2BBr_6(001) heterojunction, monolayer g-C_3N_4, and Cs_2BBr_6(001) slab, respectively. Negative binding energy indicates that g-C_3N_4/Cs_2BBr_6 composites can form stable interfaces. The calculated binding energy of g-C_3N_4/Cs_2PtBr_6 is -4.2979 eV, which indicates that there is a strong interaction between the g-C_3N_4 layer and the Cs_2PtBr_6 layer. In contrast, Cs_2SnBr_6 and Cs_2TiBr_6 are not as stable as the other two heterojunctions. In addition, the lattice mismatch energy can also roughly evaluate the stability of the heterojunction. The lattice mismatch energy of the studied composites can be estimated as

$$E_{mismatch} = E_{g-C_3N_4} + E_{Cs_2BBr_6} - E'_{g-C_3N_4} - E'_{Cs_2BBr_6} \quad (2)$$

where $E_{g-C_3N_4}$ and $E_{Cs_2BBr_6}$ are the total energies of the isolated monolayer g-C_3N_4 and isolated Cs_2BBr_6(001) with the equilibrium lattice constant of the g-C_3N_4/Cs_2BBr_6 heterojunction, respectively. The$E'_{g-C_3N_4}$ and $E'_{Cs_2BBr_6}$ represent the total energies of the isolated monolayer g-C_3N_4 and Cs_2BBr_6(001) after all free geometry relaxation, respectively. The calculated lattice mismatch energies in this work are 4.15 eV for Cs_2PtBr_6, 10.26 eV for Cs_2SnBr_6, and 6.26 eV for Cs_2TiBr_6, which indicate that the lattice match of model Cs_2PtBr_6 is superior to that of Cs_2SnBr_6 and Cs_2TiBr_6.

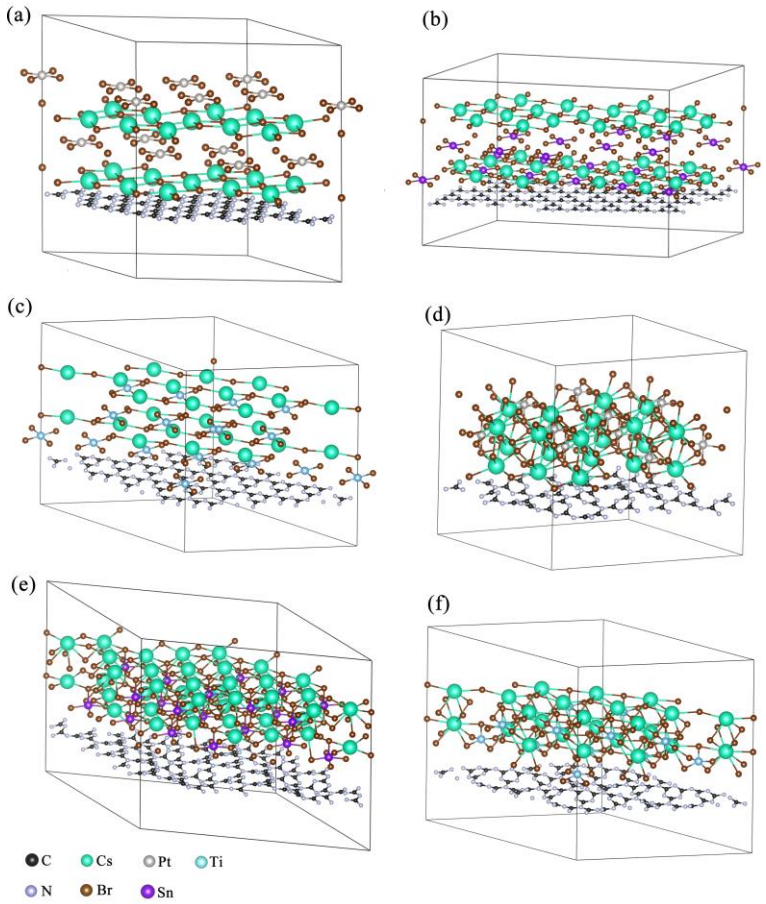

Figure. 2. Theoretical models for (a) g-C_3N_4/Cs_2PtBr_6, (b) g-C_3N_4/Cs_2SnBr_6, and (c) g-C_3N_4/Cs_2TiBr_6 heterojunctions. Optimized geometric structures of (d) g-C_3N_4/Cs_2PtBr_6, (e) g-C_3N_4/Cs_2SnBr_6, and (f) g-C_3N_4/Cs_2TiBr_6 heterojunctions.

Table. 1. The lattice mismatch ratios, mismatch energies (eV) and binding energies (eV) of g-C_3N_4/Cs_2BBr_6 using GGA-PBE functional.

Species	g-C_3N_4/ Cs_2PtBr_6	g-C_3N_4/ Cs_2SnBr_6	g-C_3N_4/ Cs_2TiBr_6
a%	0.3	2.8	0.8
b%	0.9	2.8	1.0
Binding energy (eV)	-4.2979	-1.6596	-2.8896
Mismatch energy (eV)	4.1542	10.2574	6.2574

5.3.2 Electronic properties

In order to study the photocatalytic activity of g-C_3N_4/Cs_2BX_6 heterojunction, we calculated the band structure of the heterojunction using PBE functional. At the same time, the bands of monolayer g-C_3N_4 and Cs_2BX_6 (001) surfaces were calculated by using HSE06 functional for comparison. The band structure is shown in Fig. 3. The monolayer layer g-C_3N_4 is a direct bandgap semiconductor, where the valence band maximum (VBM) and conduction band minimum (CBM) are at GAMMA-point (Fig. 3a). The calculated bandgap is 2.73 eV, which is very consistent with the experimental value (2.7 eV) and the previous calculation results.[31-32]

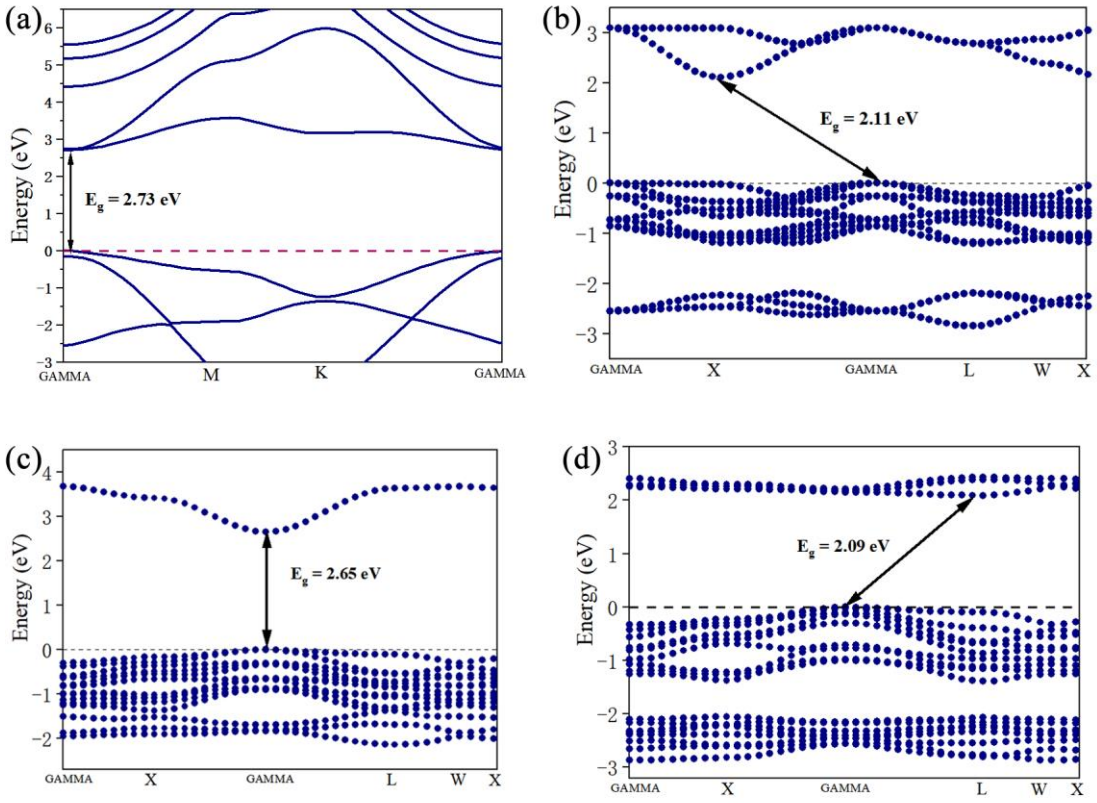

Figure. 3. Calculated band structure of (a) monolayer g-C_3N_4, (b) Cs_2PtBr_6(001) slab, (c) Cs_2SnBr_6(001) slab, (d) Cs_2TiBr_6(001) slab using HSE06 functional. The vertical line is Fermi level.

The total density of state (TDOS) and projected density of state (PDOS) are shown in Fig. 4. In DOS of g-C_3N_4 (Fig. 4a), the s-orbital electrons of N atom and the s-orbital electrons of C atom only occupy the state far away from VBM. The VBM is dominated by

N-p orbitals, while CBM is mainly contributed by N-p and C-p orbitals. Therefore, excited electron holes located on adjacent carbon and nitrogen atoms will be easily recombined according to this distribution, which leads to relatively low quantum yields. In other words, the possible high recombination probability of photogenerated carriers leads to the unsuitable band structure of g-C_3N_4 as a qualified photocatalyst for many catalytic reactions.[33] Cs_2PtBr_6 (001) slabs have indirect bandgap, its CBM is at X-point, and its VBM is at GAMMA-point (Fig. 3b). The calculated E_g is 2.11eV, which is close to the theoretical bandgap (2.23 eV) of other calculated bulk Cs_2PtBr_6.[42] The PDOS analysis of Cs_2PtBr_6 (001) surface shows that VBM is largely contributed by Br-p state, while CB is attributed to 5d of Pt and 4p state of Br (Fig. 4b). The calculated band structure and DOS of Cs_2SnBr_6 (001) slab are plotted in Fig. 3c and Fig. 4c, respectively. Obviously, this perovskite is a semiconductor with a direct bandgap of 2.65 eV, which is consistent with the experimental bandgap of 2.7 eV.[34] Both CBM and VBM are located at the GAMMA point. This direct bandgap facilitates the easier transfer of electrons from VBM to CBM. The VB of the Cs_2SnBr_6 (001) surface is mainly dominated by the Br-p state, while the CBM is mainly attributed to the Sn-d and Br-p states. The Cs orbit mainly contributes to the region far from the Fermi level. In Fig. 3d, the band structure results indicate that Cs_2TiBr_6 (001) is also an indirect bandgap (2.09 eV) semiconductor, which agrees well with experimental value (2.0 eV).[35] By analysing the PDOS of Cs_2TiBr_6 (001) (Fig. 4d), we can see that the electronic states near CBM and VBM are mainly contributed by Ti-d orbit and Br-p orbit. There is a strong hybridization between the Ti-3d orbitals and the Br-4p orbitals.

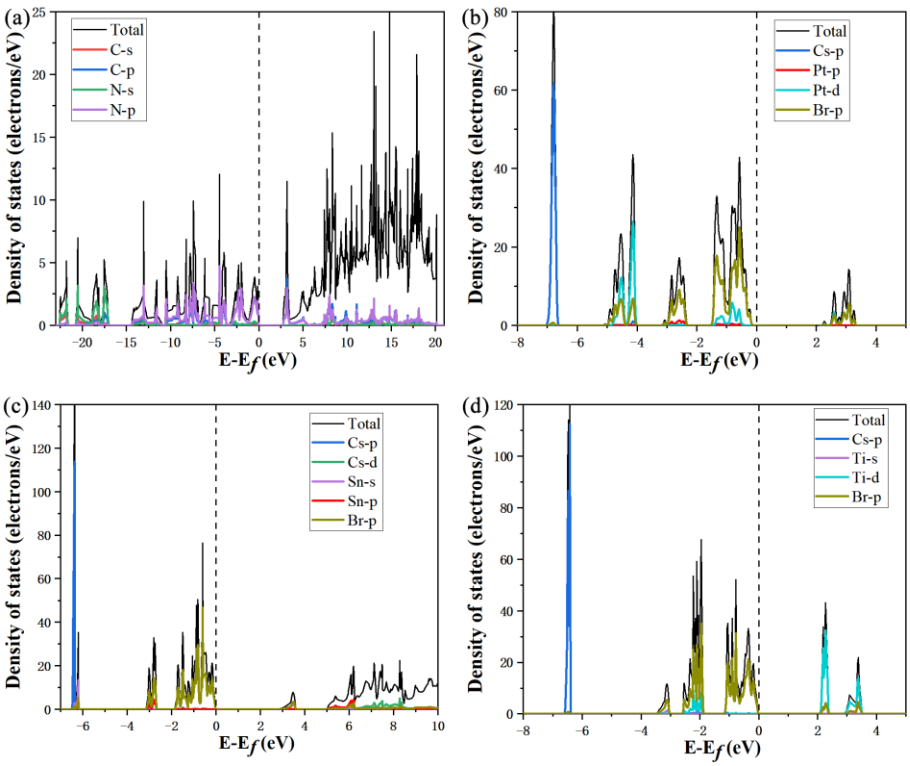

Figure. 4. Calculated TDOS and PDOS of (a) monolayer g-C_3N_4, (b) Cs_2PtBr_6(001) slab, (c) Cs_2SnBr_6(001) slab, (d) Cs_2TiBr_6(001) slab. The vertical line is Fermi level.

To describe the g-C_3N_4/Cs_2BBr_6 interaction more clearly, it is insightful to analyze their electronic structures. The band structure and total DOS of g-C_3N_4/Cs_2PtBr_6 (001), g-C_3N_4/Cs_2SnBr_6 (001) and g-C_3N_4/Cs_2TiBr_6 (001) composites and the PDOS of perovskite and g-C_3N_4 monolayer are shown in Fig 5a-c. Although PBE functional tends to underestimate the band gap value, by comparing the band structures of heterojunctions g-C_3N_4 and Cs_2BBr_6, the bandgap of composite materials is reduced to a certain extent, which is due to the interaction between g-C_3N_4 and perovskites layer. The bandgap values of g-C_3N_4/Cs_2PtBr_6 (001), g-C_3N_4/Cs_2SnBr_6 (001) and g-C_3N_4/Cs_2TiBr_6 (001) are 0.83eV, 0.49 eV and 0.56 eV respectively. It is possible that the electric field will be formed at the interface of g-C_3N_4/Cs_2BBr_6 heterojunction. In particular, the interaction between B-site cation of Cs_2BBr_6, and N atoms will lead to the redistribution of electronic state density, and change the relative state positions at C, N and B-site cation. The combination of g-C_3N_4 and perovskite leads to the redistribution of N-p state, which provides more electrons to participate in the d orbital state of the B atom at the CBM. The charge compensation effect between B-d and N-p reduces the transition energy of electrons from VB to CB. Therefore, the bandgap of heterojunction is much smaller than that of monolayer g-C_3N_4 and isolated

perovskites. This result is somewhat similar to the band gap of previously reported g-C_3N_4/WS_2[36], g-C_3N_4/CdS[37] and g-C_3N_6/TiO_2[38] heterojunctions, and due to the coupling between planes, the band distribution of the three heterojunctions near the Fermi level changes slightly. As shown in Fig. 5, the figure of the computed DOS projected on two different layers in the proposed hybrid nanocomposite is similar to the TDOS isolating Cs_2PtBr_6, Cs_2SnBr_6, Cs_2TiBr_6 and g-C_3N_4 monolayers. It is easy to understand, because the separation between the perovskite and g-C_3N_4 is relatively large, there is no covalent bond when the mixed interface is formed.[25]

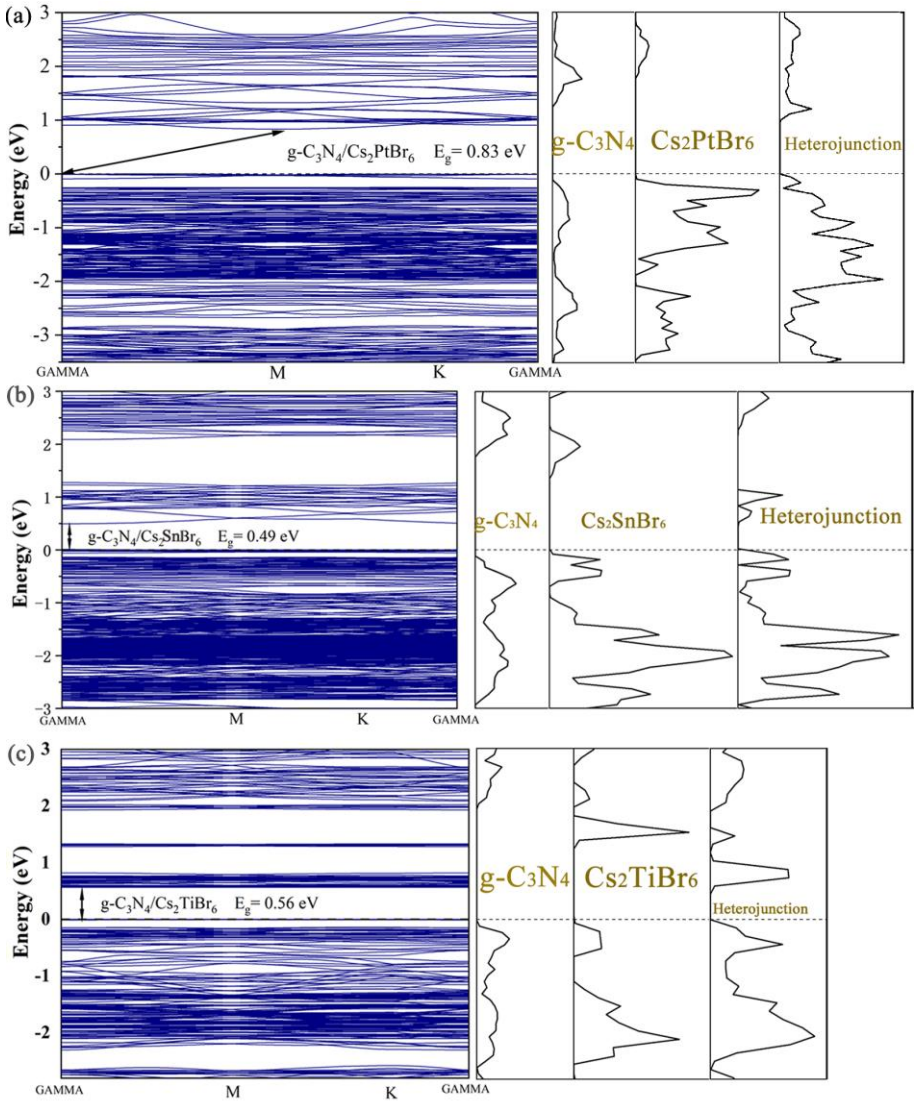

Figure. 5. Band structure and partial density of states of the (a) g-C_3N_4/Cs_2PtBr_6, (b) g-C_3N_4/Cs_2SnBr_6, (c) g-C_3N_4/Cs_2TiBr_6 heterojunctions by PBE functional.

5.3.3 Charge density difference and mechanism analysis

The work function(ϕ) analysis can help us understand the origin of interfacial charge transfer. [37] The reactivity of the photocatalyst is evaluated by its work function, which is well defined as the minimum energy required to remove electrons from the solid surface to the vacuum level. The work function is given by the following formula:

$$\phi = E_{Vacuum} - E_F \quad (3)$$

where E_{vacuum} and E_F represent the energy of a stationary electron in the vacuum near the surface and the Fermi energy, respectively. The vacuum energy is the average potential energy on the plane parallel to the heterojunction. The average plane electron potential obtained about the Z-axis is shown in Fig. 6. On the basis of eq 3, the work functions of g-C_3N_4 supercell, Cs_2PtBr_6 (001) supercell, and g-C_3N_4/Cs_2PtBr_6 (001) heterojunction were 4.35, 6.52, and 6.14 eV, respectively. The results are illustrated in Fig. 6a-c. For g-C_3N_4 supercell, Cs_2SnBr_6 (001) supercell, and g-C_3N_4/Cs_2SnBr_6 (001) heterojunction, the work functions are estimated to be 4.28, 5.50 and 5.23eV respectively, and shown in Fig. 6d-f. Fig. 6g-i show the calculated work function of g-C_3N_4 supercell, Cs_2TiBr_6 (001) supercell, and g-C_3N_4/Cs_2TiBr_6 (001) heterojunction, respectively. The calculated work functions of the g-C_3N_4 is almost consistent with that reported previously.[37] The difference of work functions between g-C_3N_4 and Cs_2BBr_6 shows that when g-C_3N_4 contacts Cs_2BBr_6, electrons flow from g-C_3N_3 to Cs_2BBr_6.

In the photocatalytic reaction, when the light ($h\nu \geq e^-$) falls on the semiconductor material and is excited from the VB to the CB, leaving holes (h^+). This is the basic step involved in all photocatalytic processes, as shown in Eq 4. In particular, the energy should be higher so that the photogenerated charge can migrate to the surface of the photocatalyst, thus participating in the redox reaction. These electrons and holes can be used in various photocatalytic reactions as long as their reduction potential meets the application requirements. Eqs 5-8 give descriptions of the general reactions and reduction potential involved in organic pollutant degradation, H_2 generation, CO_2 reduction and N_2 fixation, and the relevant reaction potentials are shown in Fig. 7.[2] All these conditions may be slightly different during the experiment, because not every reaction is carried out at pH=0 or 7.

$$\text{photocatalyst} + h\nu \rightarrow \text{photogenerated charges } (e^- \text{ and } h^+) \quad (4)$$

pollutant molecules + reactive species → degraded products (5)

$2H^+ + 2e^- \rightarrow H_2$ (6)

$CO_2 + xH^+ + xe^- \rightarrow$ useful products (7)

$N_2 + 6H^+ + 6e^- \rightarrow 2NH_3$ (8)

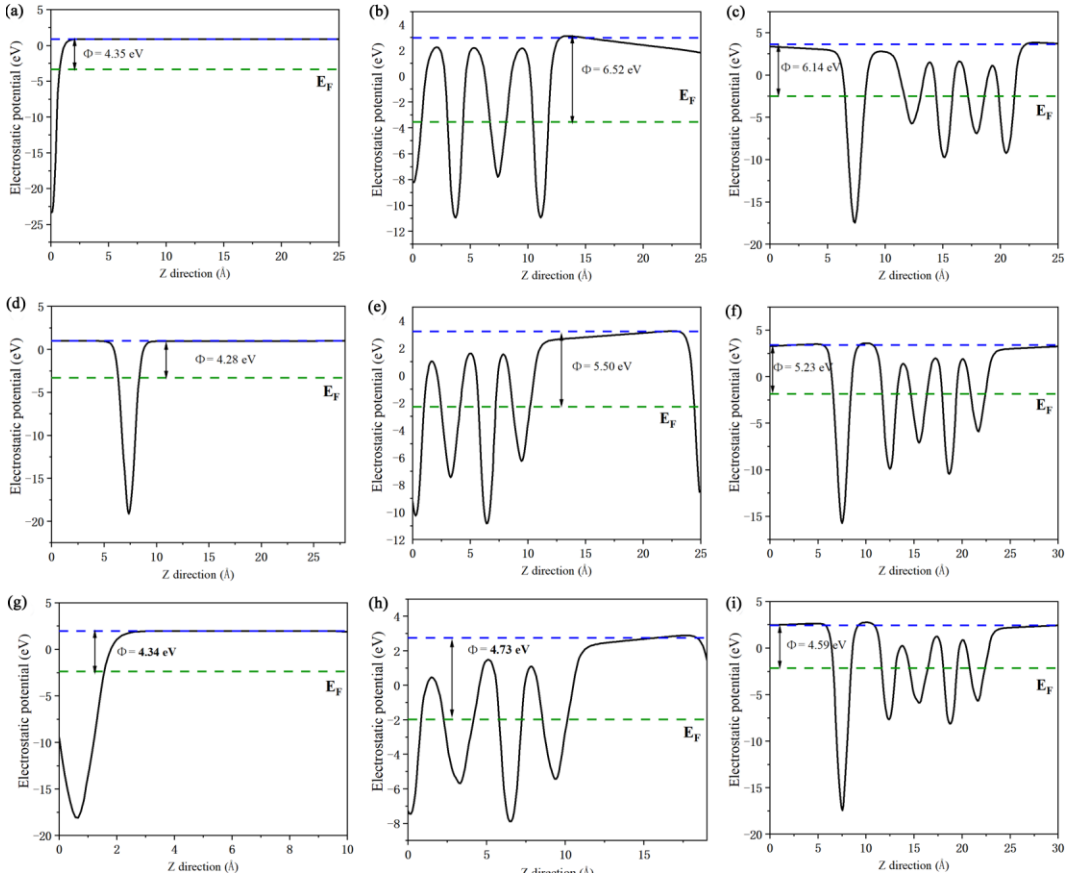

Figure. 6. Calculated electrostatic potentials for (a) monolayer g-C_3N_4 of the g-C_3N_4/Cs_2PtBr_6 heterojunction, (b) Cs_2PtBr_6(110) surface, and (c) g-C_3N_4/Cs_2PtBr_6 heterojunction slab model; Calculated electrostatic potentials for (d) monolayer g-C_3N_4 of the g-C_3N_4/Cs_2SnBr_6 heterojunction, (e) Cs_2SnBr_6(110) surface, and (f) g-C_3N_4/Cs_2SnBr_6 heterojunction slab model; Calculated electrostatic potentials for (g) monolayer g-C_3N_4 of the g-C_3N_4/Cs_2TiBr_6 heterojunction, (h) Cs_2TiBr_6(110) surface, and (i) g-C_3N_4/Cs_2TiBr_6 heterojunction slab model.

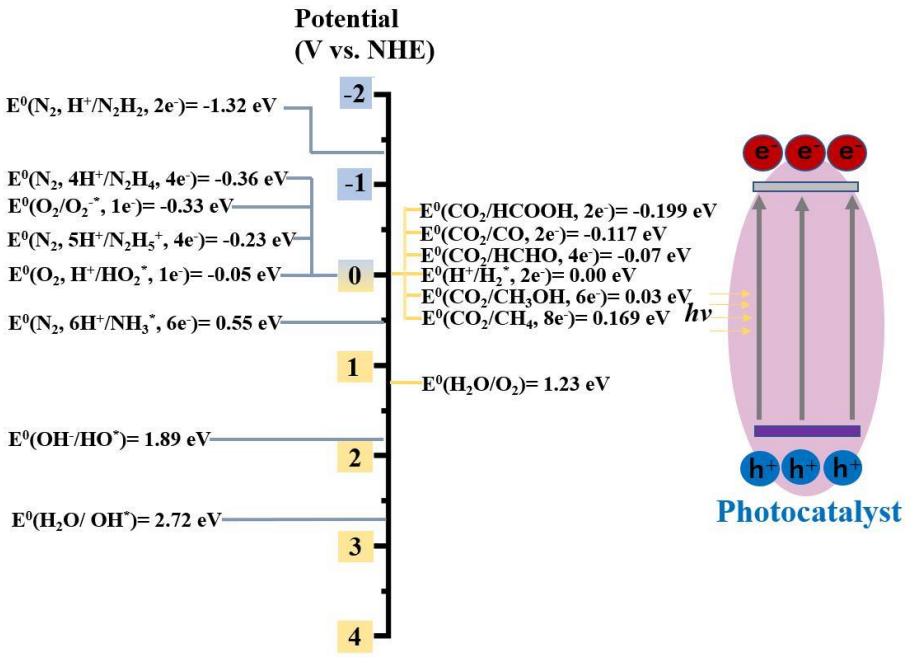

Figure. 7. Schematic illustration of photoexcitation in a photocatalyst and reduction potential values for the formation of different photocatalytic products at pH = 0 vs. NHE.

The mechanism of photocatalytic water decomposition and pollutant degradation mainly depends on the generation, separation, transfer and participation of photoinduced charge carriers.[39] In order to understand the influence of photogenerated charge carriers on the recombination behaviour and redox reaction in g-C_3N_4/Cs_2BBr_6 heterojunction, the band edge positions of g-C_3N_4, Cs_2PtBr_6, Cs_2SnBr_6, and Cs_2TiBr_6 were calculated using empirical eqs 9-10:[40]

$$E_{\mathrm{CBE}} = E_{CBE} + E_g \tag{9}$$

$$E_{\mathrm{VBE}} = (\chi_{Cs}^2 \chi_B \chi_{Br}^6)^{\frac{1}{9}} - \frac{1}{2} E_g + E_0 \tag{10}$$

Where E_{CBE} and E_{VBE} are the CBE and VBE potential of perovskites, respectively. The χ refers to the absolute electronegativity of the atoms Cs, B, and Br of Cs_2BBr_6. E_g is the bandgap, and E_0 is −4.5 eV for NHE, which show the scale factor from the redox level of the reference electrode to the absolute vacuum scale. The results are shown in left part of Fig. 8, the calculated band edge position of g-C_3N_4 and Cs_2BBr_6 are their potential before contact. When g-C_3N_4 contacts Cs_2BBr_6, the heterojunctions are formed, and the relative positions of CB and VB change with the Fermi level. Therefore, it is very important to accurately calculate the changes of CB and VB positions after contact to determine the redox ability of g-C_3N_4/Cs_2BBr_6 heterojunctions. Fig. 8a shows that

the work function (6.52 eV) of Cs_2PtBr_6 is higher than that of g-C_3N_4 (4.35eV), which causes electrons to move from g-C_3N_4 to Cs_2PtBr_6 until the Fermi energies of the two semiconductors align. The work function (6.14 eV) of g-C_3N_4/Cs_2PtBr_6 heterojunction is between that of g-C_3N_4 and Cs_2PtBr_6. Due to electron transfer, when the two components reach the same Fermi energy level, the built-in electric field from the g-C_3N_4 sheet to the Cs_2PtBr_6 surface will be established. For heterojunctions, a potential well is formed between the g-C_3N_4 and the Cs_2PtBr_6. The built-in potential can stop the charge diffusion between the g-C_3N_4 and Cs_2PtBr_6. Similarly, since the work function of g-C_3N_4 is smaller than that of Cs_2SnBr_6 (5.50 eV) and Cs_2TiBr_6 (4.73 eV), the work function of the heterojunction is also between them. Negative charges accumulate on the surface areas of Cs_2SnBr_6 and Cs_2TiBr_6. On the contrary, the g-C_3N_4 layer accumulates positive charges. The net positive and negative charges induce the internal electric field from g-C_3N_4 to Cs_2BBr_6. The internal electric field at the interface generates another force on holes and electrons, which is opposite to the diffusion force. In thermal equilibrium, electric field force and diffusion force reach equilibrium.

With the change of Fermi energy, VB and CB of g-C_3N_4 move down 1.79 eV in g-C_3N_4/Cs_2PtBr_6, while VB and CB of Cs_2PtBr_6 move up 0.38 eV. According to the analysis in Fig 8a, after the contact of the two semiconductors, the CBM in Cs_2PtBr_6 is higher than g-C_3N_4, while the VBM in g-C_3N_4 is lower than Cs_2PtBr_6. VB offset (VBO) and CB offset (CBO) are the relative positions of VBM and CBM on both sides of the interface, respectively. They are the key factors affecting the photocatalytic performance of g-C_3N_4/Cs_2PtBr_6 heterojunctions. When the g-C_3N_4/Cs_2PtBr_6 heterojunction absorbs photon energy under visible light irradiation, an electronic transition from VB to CB occurs, and photogenerated holes are generated in VB. The presence of CBO induces the photogenerated electrons in the CB of Cs_2PtBr_6 to transfer to the CB of g-C_3N_4. On the contrary, the existence of VBO leads to the transfer of photogenerated holes in VB of g-C_3N_4 to VB in Cs_2PtBr_6, which leads to the accumulation of electrons at CB of g-C_3N_4 and holes at VB of Cs_2PtBr_6. In addition, the internal electric field in the g-C_3N_4/Cs_2PtBr_6 heterojunction acts as a selector. This field promotes the movement of photogenerated electrons from CB in Cs_2PtBr_6 to CB in g-C_3N_4, and the movement of photogenerated holes from VB in g-C_3N_4 to VB in Cs_2PtBr_6. At the same time, the reverse motion of photogenerated electrons and holes is inhibited. Therefore, under the combined action of band offset and built-in electric field, photogenerated electrons and holes are effectively separated on different surfaces.[41] Similar to g-

C_3N_4/Cs_2PtBr_6, g-C_3N_4/Cs_2SnBr_6 heterojunction also forms a type II staggered band arrangement, which is conducive to the separation and transfer of photoinduced electrons and holes. After the two semiconductors g-C_3N_4 and Cs_2SnBr_6 contact, the VB edge position of g-C_3N_4 becomes 2.71 eV, which is more positive than OH^-/HO^* (1.89 eV). The CB edge position of Cs_2SnBr_6 becomes -1.04 eV, which is more negative than the CB edge position of Cs_2PtBr_6 in g-C_3N_4/Cs_2PtBr_6 heterojunction, and can cover the potential required by most nitrogen catalytic reactions. The VBM of g-C_3N_4 is lower than that of Cs_2TiBr_6, and the CBM is higher than that of Cs_2TiBr_6. However, after the contact between the two, the VB edge of Cs_2TiBr_6 changes to the negative direction and is finally lower than that of g-C_3N_4. Compared with Cs_2TiBr_6, g-C_3N_4 is a semiconductor photocatalyst with highly negative CB and highly positive VB, which forms a type I (straddling gap) heterojunction after contact. This heterojunction will accumulate photogenerated charge on Cs_2TiBr_6, so it is not conducive to photocatalysis.

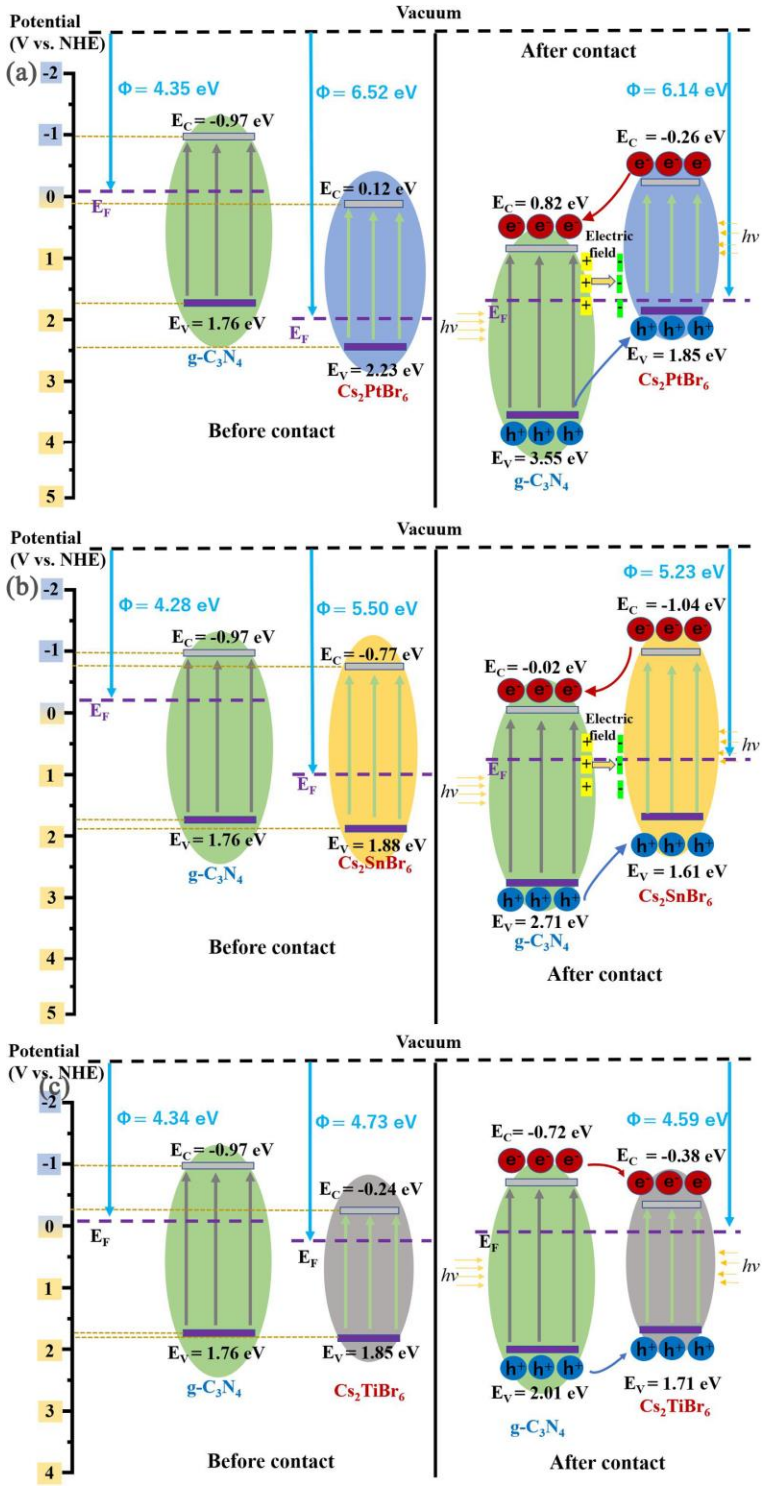

Figure. 8. Diagram of the band edge positions before and after contact of (a) g-C_3N_4/Cs_2PtBr_6, (b) g-C_3N_4/Cs_2SnBr_6, (c) g-C_3N_4/Cs_2TiBr_6 heterojunction photocatalysts.

5.4 Conclusions

In conclusion, the structural, electronic properties and photocatalytic mechanism of g-C_3N_4/Cs_2BBr_6 were systematically investigated by performing first-principles calculations. When they are close to each other, the two layers of g-C_3N_4 and Cs_2BBr_6 can produce obvious synergistic effect, which can lead to the distortion of g-C_3N_4 plane and lattice structure change. The combination of Cs_2BBr_6 and g-C_3N_4 can obtain a narrower band gap than the isolated one. Our calculation results show that both g-C_3N_4/Cs_2PtBr_6 and g-C_3N_4/Cs_2SnBr_6 heterojunctions have indirect band gaps, while g-C_3N_4/Cs_2TiBr_6 heterojunctions have direct band gaps. The band gap values of g-C_3N_4/Cs_2PtBr_6, g-C_3N_4/Cs_2SnBr_6 and g-C_3N_4/Cs_2TiBr_6 are 0.83, 0.49 and 0.56 eV, respectively. By analyzing the work function and the energy level matching between the two semiconductors, it can be inferred that negative charges accumulate on the surface areas of Cs_2BBr_6. On the contrary, the g-C_3N_4 layer accumulates positive charges. The net positive and negative charges induce the internal electric field from g-C_3N_4 to Cs_2BBr_6. The internal electric field at the interface generates another force on holes and electrons, which is opposite to the diffusion force. The calculated band arrangement between g-C_3N_4 monolayer and Cs_2BBr_6 (001) surface shows that the g-C_3N_4/Cs_2PtBr_6 and g-C_3N_4/Cs_2SnBr_6 heterojunction forms a type II staggered band arrangement. The g-C_3N_4/Cs_2TiBr_6 forms a type I (straddling gap) heterojunction after contact. The type II heterojunction is conducive to the separation and transfer of photoinduced electrons and holes. The type I heterojunction will accumulate photogenerated charge on $C_{s2}TiBr_6$ and hinder transmission, so it is not conducive to photocatalysis.

References

1 Xiong Z, Lei Z, Li Y, et al. A review on modification of facet-engineered TiO_2 for photocatalytic CO_2 reduction. *J. Photoch. Photobio. C.* **2018**;36:24-57.

2 Kumar A, Kumar A, Krishnan V. Perovskite oxide based materials for energy and environment-oriented photocatalysis. *ACS Catal.* **2020**;10:10253-10315.

3 Wang W, Tade M, Shao Z. Research progress of perovskite materials in photocatalysis- and photovoltaics-related energy conversion and environmental treatment. *Chem. Soc. Rev.* **2015**;44:5371–5408.

4 Fujishima A. Honda, K. Electrochemical Photolysis of Water at a semiconductor electrode. *Nature*. **1972**;238:37.

5 Zhu J, Li H, Zhong L, et al. Perovskite Oxides: Preparation, Characterizations, and Applications in Heterogeneous Catalysis. *ACS Catal.* **2014**;4:2917−2940.

6 Kong X, Geng W, Li W, et al. Co encapsulated N-doped carbon nanotubes as robust catalyst for valorization of levulinic acid in aqueous media. *J. Energy Chem.* **2021**;52:12–19.

7 Zhao Z, Sun Y, Dong F. Graphitic carbon nitride based nanocomposites: a review. *Nanoscale.* **2015**;7:15–37.

8 Yang J, Wang D, Han H, et al. Roles of cocatalysts in photocatalysis and photoelectrocatalysis. *Acc. Chem. Res.* **2013**;46:1900–1909.

9 Li C, Wang S, Wang T, et al. Monoclinic porous $BiVO_4$ networks decorated by discrete g-C_3N_4 nano-islands with tunable coverage for highly efficient photo catalysis. *Small*. **2014**;10:2783−2790.

10 Fang Y, Kong X, Wang D, et al. Insights into the interactions of g-C_3N_4/$LaMnO_3$ hetero-junction to their structures and electronic properties by DFT calculations. *J. Solid State Chem*. **2020**;292:121727.

11 Sepahvand H, Sharifnia S. Photocatalytic overall water splitting by Z-scheme g-C_3N_4/$BiFeO_3$ heterojunction. *Int. J. Hydrogen Energ*. **2019**;44:23658-23668.

12 Xiu Z, Bo H, Wu Y, Hao X, et al. Graphite-like C_3N_4 modified Ag_3PO_4 nanoparticles with highly enhanced photocatalytic activities under visible light irradiation. *Appl. Surf. Sci*. **2014**;289:394–399.

13 Park S, Chang W, Lee C, et al. Photocatalytic hydrogen generation from hydriodic acid using methylammonium lead iodide in dynamic equilibrium with aqueous solution. *Nat. Energy*. **2016**;2:16185.

14 Wu Y, Wang P, Zhu X, et al. Composite of $CH_3NH_3PbI_3$ with reduced graphene oxide as a highly efficient and stable visible-light photocatalyst for hydrogen evolution in aqueous HI solution. *Adv. Mater.* **2018**;30:1704342.

15 Li X, Chen M, Mei S, et al. Light-induced phase transition and photochromism in all-inorganic two-dimensional $Cs_2PbI_2Cl_2$ perovskite. *Sci. China Mater.* **2020**;63:1510–1517.

16 Hao F, Stoumpos C, Cao D, et al. Lead-free solid-state organic-inorganic halide perovskite solar cells. *Nat. Photonics.* **2014**;8:489-494.

17 Noel N, Stranks S, Abate A, et al. Leadfree organic-inorganic tin halide perovskites for photovoltaic applications. *Energy Environ. Sci*. **2014**;7:3061-3068.

18 Wang T, Yue D, Li X, et al. Lead-free double perovskite $Cs_2AgBiBr_6$/RGO composite for efficient visible light photocatalytic H_2 evolution. *Appl. Catal. B: Environ.* **2020**;268:118399.

19 Tan T, Wang X, Zhou X, et al. Highly active Cs_2SnCl_6/C_3N_4 heterojunction photocatalysts operating via interfacial charge transfer mechanism. *J. Hazard. Mater.* **2022**;439:129694.

20 Huang H, Verhaeghe D, Weng B, et al. Metal Halide Perovskite Based Heterojunction Photocatalysts. *Angewandte Chemie*. **2022**;e202203261.

21 Kresse G, Furthmuller J. Efficiency of ab-initio total energy calculations for metals and semiconductors using a plane-wave basis set. *Comput. Mater. Sci.*, **1996**;6:15-50.

22 Perdew J, Burke K, Ernzerhof M. Generalized Gradient Approximation Made Simple. *Phys. Rev. Lett.* **1996**;77:3865-3868..

23 Blöchl P. Projector augmented-wave method. *Phys. Rev. B*. **1994**;50:17953-17979.

24 Perdew J. Density functional theory and the band gap problem. *Int. J. Quantum Chem*. **1986**;30:451-451.

25 Wang J, Guan Z, Huang J, et al. Enhanced photocatalytic mechanism for the hybrid g-C_3N_4/MoS_2 nanocomposite. *J. Mater. Chem. A.* **2014**;2:7960–7966.

26 Xu M, Liang T, Shi M, et al. Graphene-like two-dimensional materials. *Chem. Rev*. **2013**;113:3766-3798.

27 Xu L, Huang W, Wang L, et al. Insights into enhanced visible-light photocatalytic hydrogen evolution of g-C_3N_4 and highly reduced graphene oxide composite: the role of oxygen. *Chem. Mater*. **2015**;27:1612–1621.

28 Ferrari A, Coghi L. On the existence of hexahalogenoaurates. *Gazz. Chim. Ital*. **1941**;71:440-441.

29 Torres D, Freire J, Katiyar R, et al. Lattice dynamics of crystals having R_2MX_6 structure. *Phys. Rev. B*. **1997**;56:7763.

30 Ju M, Chen M, Zhou Y, et al. Earth-abundant nontoxic titanium (IV)-based vacancy-ordered double perovskite halides with tunable 1.0 to 1.8 eV bandgaps for photovoltaic applications. A*CS Energy Lett*. **2018**;3:297-304.

31 Wang X, Maeda K, Thomas A, et al. A metal-free polymeric photocatalyst for hydrogen production from water under visible light. *Nat. Mater*. **2009**;8:76−80.

32 Opoku F, Govender K, van Sittert C, et al. Insights into the photocatalytic mechanism of mediator-free direct Z-scheme g-C_3N_4/Bi_2MoO_6 (010) and g-C_3N_4/Bi_2WO_6 (010) heterojunctions: a hybrid density functional theory study. *App. Surf. Sci*. **2018**;427:487-498.

33 Fang Y, Kong X, Wang D, et al. Insights into the interactions of g-C_3N_4/$LaMnO_3$ hetero-junction to their structures and electronic properties by DFT calculations. *J. Solid State Chem.* **2020**;292:121727.

34 Kaltzoglou A, Antoniadou M, Kontos A, et al. Optical-vibrational properties of the Cs_2SnX_6 (X= Cl, Br, I) defect perovskites and hole-transport efficiency in dye-sensitized solar cells. *J. Phys. Chem. C*. **2016**;120:11777-11785.

35 Euvrard J, Wang X, Li T, et al. Is Cs_2TiBr_6 a promising Pb-free perovskite for solar energy applications, *J. Mater. Chem.* **2020**;8:4049-4054.

36 Ma X, Chen C, Hu J, et al. Evidence of direct Z-scheme g-C_3N_4/WS_2 nanocomposite under interfacial coupling: First-principles study. *J. Alloys Compd*. **2019**;788:1-9.

37 Liu J. Origin of high photocatalytic efficiency in monolayer g-C_3N_4/CdS heterojunction: a hybrid DFT study. *J. Phy. Chem. C*. **2015**;119:28417-28423.

38 Liu J. Cheng B. Yu J. A new understanding of the photocatalytic mechanism of the direct Z-scheme g-C_3N_4/TiO_2 heterojunction. *Phys. Chem. Chem. Phys*. **2016**;18:31175–31183..

39 Jo W, Lee J, Natarajan T. Fabrication of hierarchically structured novel redox-mediator-free $ZnIn_2S_4$ marigold flower/Bi_2WO_6 flower-like direct Z-scheme nanocomposite photocatalysts with superior visible light photocatalytic efficiency. *Phys. Chem. Chem. Phys*. **2016**;18:1000–1016.

40 Shi L, Liang L, Wang F, et al. Facile synthesis of a g-C_3N_4 isotype composite with enhanced visible-light photocatalytic activity. *RSC Adv*. **2015**;5:101843-101849.

41 Cao S, Yu J. g-C_3N_4-based photocatalysts for hydrogen generation. *J. Phys. Chem. Lett*. **2014**;5:2101-2107.

42 Faizan M, Bhamu K, Khan S, et al. Computational study of defect variant perovskites A_2BX_6 for photovoltaic applications. *arXiv preprint* arXiv:2002.07543, **2020**.

Chapter 6. General conclusions and future prospects

In this thesis, we mainly focused on find potential materials suitable for solar cells or photocatalysts in Cs Based Vacancy Ordered Double Perovskites. Firstly, we simulated and optimized the structure of the $Cs_2PtI_{6-y}Cl_y$, $Cs_2PtI_{6-y}Br_y$, and $Cs_2PtBr_{6-y}Cl_y$ (y = 0, 1, 2, 3, 4, 5, 6) and systematically studied their electronic properties. Secondly, we investigate the structural, electronic, and optical properties of Cs_2BX_6 compounds, with the goal of finding suitable candidates for photocatalysts and perovskite solar cells. Thirdly, the structural, electronic properties and photocatalytic mechanism of g-C_3N_4/Cs_2BBr_6 were systematically investigated by performing first-principles calculations.

In chapter 1, the background and development status of photovoltaic technology and photocatalysis, including the classification of devices and photocatalysts, and the basic principles of solar cells and photocatalysis are introduced.

In chapter 2, the density functional theory and calculation methods based on which this paper is based are introduced, and the calculation tools used are listed.

In chapter 3, we performed a first-principles investigation based on density functional theory to study the structural and electronic properties of $Cs_2PtI_{6-y}Cl_y$, $Cs_2PtI_{6-y}Br_y$, $Cs_2PtBr_{6-y}Cl_y$ (y = 0, 1, 2, 3, 4, 5, 6). The calculated structural parameters revealed a good mechanical stability for all these compounds, and the trend in the formation energy indicated that the substitution of I^- with Cl^- and Br^- can significantly reduce the energy and improve the thermodynamic stability. Through a comparative analysis of the electronic properties of Cs_2PtX_6 (X = Cl, Br, I), we found that the substitutional doping of halogen ions can effectively adjust the bandgap and show an obvious trend.

In chapter 4, Screening homovalent alternatives for B and X-site ions in vacancy-ordered double perovskite Cs_2BX_6 for solar cell applications and photocatalyst was done using Perdew–Burke–Ernzerhof and Heyd–Scuseria–Ernzerhof functional with spin-orbit coupling. Three empirical factors and formation enthalpy were used to evaluate the stability of 30 materials at different temperatures. Finally, the Cs-based vacancy-ordered double perovskites with suitable bandgap for optoelectronic applications can thus be obtained.

In chapter 5, the structural, electronic properties and photocatalytic mechanism of g-C_3N_4/Cs_2BBr_6 were systematically investigated by performing first-principles calculations.

The bandgap of three heterojunction of three heterojunction are 0.83eV, 0.49 eV and 0.56 eV respectively, which will be smaller than that of the isolated semiconductor. The difference of work functions between g-C_3N_4 and perovskite shows that when two semiconductor contacts, electrons will transfer from g-C_3N_4 layer to perovskites layer. According to the work function and band edge position of the semiconductor, it can be found Cs_2PtBr_6 based and Cs_2SnBr_6 based heterojunction belong to Type II. The Cs_2TiBr_6 based heterojunction belongs to Type I.

The prospects of the research content may include the following aspects. 1. Synthesize $Cs_2PtI_yBr_{6-y}$ and characterize the performance of perovskite solar cells by experiments. 2. Calculate the properties of Rb based vacancy ordered double perovskites and predict their potential application value. 3. Calculate the differential charge density of g-C_3N_4/Cs_2TiBr_6 heterojunction to support the conclusion. We present the guiding value of theoretical research for experiments with an optimistic attitude, and believe that this field will successfully predict the perovskite solar cell materials and photocatalysts with practical value in the future.

Achievements

Publications

1. **Xinyu Ye**, Anmin Liu*, Liguo Gao, Chu Zhang, Lijing Yan, Shizheng Wen, Tingli Ma*. High-Performance Computational screening of Cs based vacancy-ordered double perovskites for solar cell and photocatalysis applications. *EcoMat*. 2022, e12295.
2. **Xinyu Ye**, Anmin Liu*, Yue Zhao, Qianji Han, Takeshi Kitamura, Tingli Ma*. DFT study of X-site ion substitution doping of Cs_2PtX_6 on its structural and electronic properties. *Int. J. Energy Res*. 2022, 46, 8471-8479.

Conferences

1. **Xinyu Ye**, Chu Zhang, Tingli Ma. “Studies on Development of New Materials and Improvement Stability of Perovskite Solar Cells”, 19th "Next-Generation Photovoltaic Power Generation System" Symposium (2nd Annual Meeting of the Japan Photovoltaic Energy Society). Online, June 28th - 29th 2022.

.

Acknowledgements

First, I would like to express my deepest thanks to my supervisor Professor Ma for giving me the opportunity to study here. It is her instruction and help that makes me finish my doctoral program smoothly.

Meanwhile, I would like to express my gratitude to every professor, who give their valuable comments on my work.

In addition, great thanks to all the members in Ma lab for their valuable help in daily life.

Finally, I appreciate my family to support my PhD study in Japan without doubt.